

**Sulfur Deposition in Nickel Laterite Calcination for Ferronickel Production
via Rotary Kiln-Electric Furnace Route**

by

Sahand Sarbishei

B.A.Sc., University of Tehran, 2010

M.A.Sc., Sharif University of Technology, 2012

A THESIS SUBMITTED IN PARTIAL FULFILLMENT OF
THE REQUIREMENTS FOR THE DEGREE OF

DOCTOR OF PHILOSOPHY

in

THE FACULTY OF GRADUATE AND POSTDOCTORAL STUDIES

(Materials Engineering)

THE UNIVERSITY OF BRITISH COLUMBIA

(Vancouver)

September 2021

© Sahand Sarbishei, 2021

The following individuals certify that they have read, and recommend to the Faculty of Graduate and Postdoctoral Studies for acceptance, the dissertation entitled:

Sulfur deoprtment in nickel laterite calcination for ferronickel production via rotary kiln-
electric furnace route

submitted by Sahand Sarbishei in partial fulfillment of the requirements for

the degree of Doctor of Philosophy

in Materials Engineering

Examining Committee:

Leili Tafaghodi, Materials Engineering, UBC
Supervisor

David B Dreisinger, Materials Engineering, UBC
Supervisory Committee Member

Wenying Liu, Materials Engineering, UBC
Supervisory Committee Member

Edouard Asselin, Materials Engineering, UBC
University Examiner

Marek Pawlik, Mining Engineering, UBC
University Examiner

Abstract

The rotary kiln-electric furnace (RK-EF) process is a common pyrometallurgical route for ferronickel production from nickel laterite ores. Sulfur is a harmful impurity that deteriorates the mechanical properties of nickel alloys. Due to the low sulfur content of the laterites, it is believed that the majority of the sulfur in crude ferronickel is originated from the process additives such as fuel and reductant in the rotary kiln. Therefore, it is crucial to investigate the effect of the sulfur content of the fuel on the calcine composition. Reducing sulfur absorption from the fuel to the calcine is beneficial to reduce the load of the refinery. This study investigates sulfur deportment in the nickel laterite calcination to obtain a fundamental understanding of the behavior of sulfur present in the rotary kiln fuel.

In this work, the main reactions that occur in the calcination stage are identified. The kinetics of the reactions are investigated by combining model-free and model-fitting methods. The sulfurization reactions in the nickel laterite calcination are identified, and the main sulfur-containing compound in the calcine is found to be pyrrhotite (Fe_7S_8). Using coal with higher sulfur content, employing a more aggressive reducing atmosphere in the furnace, and increasing the gas flow rate result in an increase in the sulfur content of the calcine. Increasing temperature from 600 to 700 °C leads to higher sulfur deportation from the gas phase to the calcine. However, raising the temperature above 700 °C decreases sulfur deportation due to sintering of the particles and recrystallization of the silicate compounds. A comprehensive kinetic analysis on the sulfurization reactions revealed that the sulfurization reaction is diffusion-controlled and has a low activation energy of 1.4-5.3 kJ/mol. Using CaCO_3 as a sulfur absorbent leads to 70.8-91% sulfur removal in the calcine. The effect of the processing temperature and time on reducing the sulfur content of the

calcine are also investigated. Increasing time from 30 to 120 min results in decreasing sulfur removal from 91 to 78.3%. Raising temperature from 700 to 800 °C promotes sulfur removal; however, sintering of additive particles at above 800 °C reduces sulfur removal.

Lay Summary

The predominant process for ferronickel (iron-nickel alloy) production from nickel laterite ore is the rotary kiln-electric furnace (RK-EF) operations. Rotary kiln and electric furnace are two main furnaces used in ferronickel production. The required thermal energy in the rotary kiln is provided by combustion of the fuels such as coal, which contains small amount of sulfur. Sulfur is a deleterious impurity that degrades the mechanical properties of ferronickel. Since laterite ores typically have a negligible sulfur content, the sulfur in ferronickel is believed to be originated from fuel and other process additives. This study investigates the effect of sulfur content of the fuel on the composition of the rotary kiln product to obtain a comprehensive understanding of sulfur deportment in the nickel laterite calcination. Calcium carbonate is used as a sulfur absorbent to reduce the sulfur content of the calcine.

Preface

This dissertation is the original and independent work by Sahand Sarbishei. This research is a collaboration project between the University of British Columbia (UBC) and Hatch Ltd. through Mitacs Accelerate Program. The original idea of this research was formed at a discussion between Dr. Leili Tafaghodi and Hatch representatives. The author, Sahand Sarbishei, designed and conducted all the experiments, prepared and analyzed the results, and wrote the thesis and papers. Dr. Tafaghodi supervised all aspects of the project.

The following journal and conference papers have been published from the research work presented in this thesis. The first paper is based on the results presented in chapter 5, and the other papers are prepared using the findings presented in chapter 6.

1. S. Sarbishei, L. Tafaghodi Khajavi, Kinetic analysis on nickel laterite ore calcination using model-free and model-fitting methods, *Minerals Engineering* 136 (2019) 129-139.
2. S. Sarbishei, L. Tafaghodi Khajavi, The effect of sulfur content of rotary kiln fuel on the composition of nickel laterite calcine, *Fuel* 280 (2020) 118648.
3. S. Sarbishei, L. Tafaghodi Khajavi, Effects of the reducing atmosphere of the calcination stage on the sulfur department in ferronickel production via RK-EF process, 59th Annual Conference of Metallurgists (COM), Canada, 2020.
4. S. Sarbishei, L. Tafaghodi Khajavi, Investigating the effect of temperature on sulfur department in nickel laterite calcination, Accepted for publication in The 16th International Ferro-Alloys Conference (INFACON), Norway, 2021.

The following manuscripts are under preparation.

1. S. Sarbishei, L. Tafaghodi Khajavi, Kinetic analysis on sulfur department in nickel laterite calcination, adapted from chapter 7.

2. S. Sarbishei, L. Tafaghodi Khajavi, Inhibition of sulfur transfer from fuel to the nickel laterite calcine using CaCO_3 , adapted from chapter 8.

Table of Contents

Abstract.....	iii
Lay Summary	v
Preface.....	vi
Table of Contents	viii
List of Tables	xiii
List of Figures.....	xv
List of Symbols	xxii
List of Abbreviations	xxiii
Acknowledgements	xxiv
Dedication	xxvi
Chapter 1: Introduction	1
Chapter 2: Literature Review	4
2.1 Nickel Resources	4
2.2 Nickel Sulfide Ores.....	4
2.3 Nickel Laterite Ores	5
2.3.1 Ferricrete and Limonite Zones.....	6
2.3.2 Saprolite Zone	6
2.3.3 Smectite Zone	7
2.4 Processing of Nickel Laterite Ores	7
2.4.1 High-Pressure Acid Leaching (HPAL).....	8
2.4.2 Caron Process.....	11

2.4.3	Ferronickel Production by Rotary Kiln-Electric Furnace Process.....	12
2.4.3.1	Pre-treatment and Drying.....	13
2.4.3.2	Calcination and Partial Reduction	14
2.4.3.3	Smelting	16
2.4.3.4	Refining.....	19
2.4.4	Matte Production by Rotary Kiln-Electric Furnace Process.....	19
2.4.5	Nickel Pig Iron (NPI) Production	23
2.5	Nickel Laterite Plant Specification (Pyrometallurgical Processes)	24
2.5.1	Cerro Matoso (Colombia).....	24
2.5.2	Hyuga (Japan).....	26
2.5.3	PT International Nickel Indonesia (PT Inco).....	27
2.6	Calcination of Nickel Laterites	32
2.7	Reduction of Nickel Laterites	34
2.7.1	The Effect of the Temperature	34
2.7.2	The Effect of the Reducing Atmosphere	36
2.7.3	The Effect of the Gas Flow Rate.....	37
2.7.4	The Effect of the Processing Time.....	38
2.8	Kinetics of Nickel Laterite Reduction	38
2.9	The Behavior of Laterite Ores in Carbo-Sulfurizing Gas Mixture	42
Chapter 3: Research Gaps and Objectives.....		49
3.1	Research Gaps.....	49
3.2	Research Objectives.....	50
Chapter 4: Materials and Methods		52

4.1	Materials	52
4.2	Characterization of the Raw Materials	52
4.3	Preliminary Processing of the Raw Materials.....	54
4.4	Calcination and Partial Reduction Experiments	56
4.4.1	TGA-DSC Experiments	56
4.4.2	Tube Furnace Experiments	56
4.5	Analytical Techniques and Sample Preparation	68
4.5.1	Inductively Coupled Plasma Optical Emission Spectroscopy	68
4.5.2	X-ray Diffraction, Scanning Electron Microscopy and Energy Dispersive X-ray Spectroscopy	70
Chapter 5: Kinetic Analysis on Nickel Laterite Calcination		71
5.1	Introduction.....	71
5.2	Phase Transformation and Reactions during the Calcination Process.....	71
5.3	SEM-EDS Analysis of the Calcined Samples	73
5.4	Kinetic Analysis.....	76
5.5	Conclusion	87
Chapter 6: Sulfur Department and the Effect of Operational Parameters on the Composition of the Calcine		88
6.1	Introduction.....	88
6.2	Thermodynamic Analysis	88
6.2.1	Sulfur Department	89
6.2.2	The Effect of Sulfur Content of the Burning Coal.....	91
6.2.3	The Effect of the Reducing Atmosphere (CO/CO ₂)	93

6.2.4	The Effect of the Total Gas Flow Rate	93
6.2.5	The Effect of the Temperature	94
6.3	High-Temperature Experiments.....	94
6.3.1	Characterization of the Sulfur-Containing Compound.....	94
6.3.2	The Effect of Sulfur Content of the Burning Coal.....	99
6.3.3	The Effect of the Reducing Atmosphere (CO/CO ₂)	101
6.3.4	The Effect of the Total Gas Flow Rate	103
6.3.5	The Effect of Temperature.....	105
6.4	Conclusion	108
Chapter 7: Kinetic Analysis on the Sulfur Deportation during the Calcination Process ...		109
7.1	Introduction.....	109
7.2	Kinetic Parameters and the Kinetic Model of the Sulfur Deportation during Calcination Stage	109
7.2.1	Model-Free Method	113
7.2.2	Model Fitting Method.....	116
7.2.3	Master Plot Method.....	121
7.3	The Effect of P _{SO₂} on the Kinetics of Sulfur Deportation	123
7.4	Conclusion	129
Chapter 8: Inhibition of Sulfur Transfer from the Fuel to the Calcine.....		130
8.1	Introduction.....	130
8.2	The Behavior of CaCO ₃ as a Sulfur Absorbent in the Calcination Stage.....	130
8.2.1	Thermodynamic Analysis	131
8.2.2	The XRD and SEM Analyses	135

8.3	The Effect of the Processing Time on the Sulfur Absorption Behavior of CaCO ₃	137
8.4	The Effect of the Temperature on Sulfur Absorption Behavior of CaCO ₃	141
8.5	Conclusion	144
Chapter 9: Conclusions and Recommendations for Future Work		146
9.1	Conclusions.....	146
9.2	Recommendations.....	148
Bibliography		150
Appendices.....		163
	Appendix A List of the species used for thermodynamic analysis.....	163
	Appendix B Gas flow rate calculation	164

List of Tables

Table 2.1 Nickel and iron content and SiO ₂ / MgO of the raw ore in industrial plants [45].	24
Table 2.2 Typical chemical composition of ferronickel at different plants (wt%) [45].	26
Table 2.3 Chemical composition of the feed, calcine and matte at PT Inco [13, 45].	28
Table 2.4 Summary of the specifications of the nickel laterite plants at Cerro Matoso, Hyuga, and PT Inco operations [45].	30
Table 4.1 Proximate analysis of bituminous coal (wt%).	52
Table 4.2 Chemical composition of the laterite ore analyzed by XRF.	53
Table 4.3 Experimental conditions for calcination experiments on the effects of the operational parameters.	61
Table 4.4 Experimental conditions for the samples calcined at various temperatures to investigate the kinetics of sulfur deportation.	63
Table 4.5 Experimental conditions for the samples calcined at various Pso ₂ to investigate the kinetics of sulfur deportation.	65
Table 4.6 Experimental conditions for the samples calcined at various processing times and temperatures to investigate the effect of CaCO ₃ additive on sulfur content of the calcine.	67
Table 5.1 The EDS analysis of the selected points on the raw laterite and calcined samples.	75
Table 5.2 List of the reaction models applied to investigate kinetics of nickel laterite ore calcination.	78
Table 5.3 List of model-free equations used to study the kinetics of nickel laterite ore reduction [114, 115].	79

Table 5.4 The range of the activation energy for the main reactions calculated by two model-free methods.	84
Table 5.5 Selected possible kinetic models for reactions that occur at 300, 600, and 800 °C.	86
Table 6.1 List of the probable reactions associated with sulfur deportment in the system including laterite ore and N ₂ -CO-CO ₂ -SO ₂ gas mixture at 900 °C.	91
Table 6.2 EDS analysis of the selected points in sample F5.	98
Table 7.1 Equations for sulfur content in the calcine (%) vs. time (min) at 700, 800, and 900 °C.	111
Table 7.2 Selected kinetic models for steps 1 and 2 of the sulfurization process.	118
Table 7.3 Regression equations for sulfur content of the calcine (%) vs. time (min) at different values of P _{SO₂}	125
Table 7.4 The values of P _{SO₂} and P _{SO₂,eq} used for kinetic calculations.	127
Table 7.5 Order of reaction values with respect to P _{SO₂} for the two steps of the process.	128
Table 8.1 List of the probable sulfur deportment reactions in the system, including CaCO ₃ and N ₂ -CO-CO ₂ -SO ₂ gas mixture at 800 °C.	135
Table 8.2 EDS analysis of the selected sulfur-rich points in sample B-T2.	137

List of Figures

Figure 2.1 Schematic of nickel laterite profile in a tropical climate, including approximate Ni, Fe, Co, and MgO contents of the main layers (wt%) [13].	6
Figure 2.2 Generalized flow sheets of nickel laterite processing [6, 10, 37].	8
Figure 2.3 Process flowsheet for high-pressure acid leaching (HPAL) [13].	9
Figure 2.4 Rotary kiln-electric furnace process flowsheet for ferronickel production [13].	13
Figure 2.5 Two configurations of electric furnace: (a) shielded-arc, and (b) immersed arc electric furnace [56].	18
Figure 2.6 RK-EF process flowsheet for nickel matte production [13].	21
Figure 2.7 Schematic of the process steps in Peirce-Smith converter [13].	22
Figure 2.8 The weight loss percentage versus time at various temperatures for Sivrihisar limonite ore [66].	33
Figure 2.9 The effect of temperature on the reduction of three saprolite ores in CO/CO ₂ =2.57 gas mixture [73].	35
Figure 2.10 The effect of the CO/CO ₂ on the reduction of saprolite ore at 740 °C [75].	37
Figure 2.11 The effect of the gas flow rate on the reduction of a saprolite ore at 1000 °C and CO/CO ₂ =3 [75].	38
Figure 2.12 (a) Non-isothermal TGA analysis of a nickel laterite ore, (b) Variation of the activation energy versus the extent of reaction at 450-1000 °C [95].	41
Figure 2.13 Equilibrium partial pressure of the gaseous components in CO-SO ₂ system at 700 °C [103].	44
Figure 2.14 The effect of the temperature on TGA curves at X _{co} =0.66 [103].	45

Figure 2.15 TGA plots of carbo-sulfurization of the laterite sample at 700 °C in various compositions of CO-SO ₂ gas mixture [104].	46
Figure 2.16 Predominance diagrams of (a) Fe-O-S and (b) Ni-O-S at 800 °C obtained by HSC Chemistry 5.11 [105].	48
Figure 4.1 XRD pattern of the raw laterite ore.	54
Figure 4.2 (a) Oven, (b) mortar grinder mill.	55
Figure 4.3 Particle size distribution of the ground ore.	55
Figure 4.4 Horizontal tube furnace including (1) gas inlet, (2) quartz tube, (3) gas outlet, and (4) temperature controller.	58
Figure 4.5 Schematic of the experimental setup used for the calcination experiments.	58
Figure 4.6 Calibration of the furnace temperature by comparing the temperature obtained by the external thermocouple and the one displayed by the furnace controller.	59
Figure 4.7 Experimental setup for investigating the effect of CaCO ₃ additive on the sulfur content of the calcine.	66
Figure 4.8 The ball mill grinder.	69
Figure 4.9 Muffle furnace.	69
Figure 5.1 TGA-DSC analysis of the raw laterite ore.	72
Figure 5.2 XRD patterns for the raw laterite ore and the samples collected after non-isothermal reduction at 350, 500, 630, 750, and 990 °C.	72
Figure 5.3 SEM images of (a) the raw laterite ore and (b, c) the calcined ore. Analysis points for EDS of (d) the raw laterite ore and (e, f) the calcined ore. H: hematite, SM: silica-magnesia area, M: magnetite, F: forsterite, N: nickel-rich region.	74
Figure 5.4 Mass change vs. temperature for the calcination process at various heating rates.	80

Figure 5.5 Extent of reaction vs. temp. for the calcination process at various heating rates.....	81
Figure 5.6 Regression lines for different extents of reactions based on (a) Flynn-Wall-Ozawa, and (b) Kissinger-Akahira-Suonose model-free methods.	82
Figure 5.7 Activation Energy (E) as a function of the extent of reaction (α) obtained by two model-free methods.....	84
Figure 6.1 Equilibrium composition of the main sulfur-containing compounds in the (a) calcine, (b) gases reacted with solids, and (c) input gas mixture without reaction with solids.	89
Figure 6.2 The sequence of the sulfur department reactions resulting in the formation of iron sulfide.....	90
Figure 6.3 (a) Predicted %S in the calcine versus P_{SO_2} , (b) equilibrium content of sulfur compounds versus P_{SO_2} , (c) %S in the calcine versus CO/CO ₂ , (d) %S in the calcine versus gas flow rate, (e) equilibrium content of sulfur compounds versus gas flow rate and (f) %S in the calcine versus temperature (data obtained by HSC Chemistry 5.11 [105]).	92
Figure 6.4 X-ray diffraction patterns of samples (a) S1, (b) H1, and (c) separated sulfide particles from sample H1.....	96
Figure 6.5 SEM image of sample (a) F5 and (b) sulfur-rich zone. EDS map analysis of (c) sulfur, (d) iron, (e) oxygen, (f) silicon, and (g) nickel.	97
Figure 6.6 Additional SEM image of sample (a) F5 and (b) sulfur-rich zone. EDS map analysis of (c) sulfur, (d) iron, (e) oxygen, (f) silicon, and (g) nickel.....	97
Figure 6.7 SEM images and EDS point analysis of various sulfur-rich zones in sample F5.	98
Figure 6.8 The effect of the P_{SO_2} on the % S in the calcine and sulfur deportation percentage at 900 °C, CO/CO ₂ of 4, 60 min processing time, and the gas flow rate of 57.3 ml/min.....	100
Figure 6.9 XRD patterns for samples (a) S1, (b) S3, and (c) S5.	101

Figure 6.10 The effect of CO/CO₂ on the % S in the calcine and sulfur deportation percentage at 900 °C, 5% S in burning coal (P_{SO₂} = 0.016 atm), 60 min processing time, and gas flow rate of 57.3 ml/min. 102

Figure 6.11 X-ray diffraction patterns of samples C1, C3, and C4 prepared in various reducing atmospheres..... 103

Figure 6.12 The effect of the gas flow rate on the % S in the calcine and sulfur deportation percentage at 900 °C, 5% S in burning coal (P_{SO₂} = 0.016 atm), 60 min processing time, and CO/CO₂ of 4..... 104

Figure 6.13 X-ray diffraction patterns of samples (a) F1, (b) F2, (c) F3, and (d) F5. 105

Figure 6.14 The effect of temperature on the %S in the calcine and sulfur deportation percentage at 5% S in burning coal (P_{SO₂} = 0.016 atm), CO/CO₂ of 4, 60 min processing time, and the gas flow rate of 229.2 ml/min. 106

Figure 6.15 X-ray diffraction patterns of samples prepared at various temperatures, i.e., T1-T4. 107

Figure 7.1 %S in the calcine vs. processing time for calcines processed at 700, 800, and 900 °C with constant parameters of 5% S in burning coal (P_{SO₂} = 0.016 atm) and the gas flow rate of 229.2 ml/min..... 110

Figure 7.2 Extent of reaction vs. time for samples processed at 700, 800, and 900 °C with constant parameters of 5% S in burning coal (P_{SO₂} = 0.016 atm) and the gas flow rate of 229.2 ml/min. 112

Figure 7.3 The regression lines for various extents of reaction based on the integral insoconversional method. 114

Figure 7.4 (a) The plots of dα/dt vs. time and (b) ln(dα/dt) vs. time. 115

Figure 7.5 The regression lines for various extents of reaction based on the differential isoconversional method.	115
Figure 7.6 Activation energy as a function of the extent of reaction obtained from integral and differential isoconversional methods.	116
Figure 7.7 The kinetic function $g(\alpha)$ vs. time for the selected kinetic models at 700-900 °C. (a) Contracting sphere (C3) for the first step and (b) Avrami-Erofeev (A3) for the second step. ...	118
Figure 7.8 Dependence of $\ln k$ vs. $1/T$ for two steps of the process.	119
Figure 7.9 (a) Master plot for the theoretical kinetic models and the experimental data; (b) master plot of the selected kinetic models (C3 and A3) and experimental data.	123
Figure 7.10 %S in the calcine vs. processing time for the calcines processed at 6.4×10^{-3} , 1.6×10^{-2} , and 2.6×10^{-2} atm SO_2	125
Figure 7.11 Extent of reaction vs. time for (a) step 1 (15-60 min) and (b) step 2 (75-120 min) of the sulfurization reaction.	126
Figure 7.12 The value of $g(\alpha)$ of the best kinetic model vs. time for (a) step 1 (15-60 min) and (b) step 2 (75-120 min) of the sulfurization reaction.	126
Figure 7.13 $\ln[k(P_{\text{SO}_2} - P_{\text{SO}_2, \text{eq}})^n]$ vs. $\ln(P_{\text{SO}_2} - P_{\text{SO}_2, \text{eq}})$ for the two steps of the process.	128
Figure 8.1 Predominance area diagrams for Ca-S-C-O system at (a) 700, (b) 800, and (c) 900 °C.	132
Figure 8.2 Equilibrium composition of the solids in Ca-S-C-O system at 5% S in burning coal ($P_{\text{SO}_2} = 0.016$ atm), and CO/CO ₂ of 4.	133
Figure 8.3 The equilibrium composition of the main sulfur-containing compounds in the gas mixture prior to reacting with the additives at 5% S in burning coal ($P_{\text{SO}_2} = 0.016$ atm), and CO/CO ₂ of 4.	134

Figure 8.4 The sequence of the sulfurization reactions between input gas stream and CaCO ₃ additive.....	134
Figure 8.5 X-ray diffraction patterns of (a) raw CaCO ₃ and processed CaCO ₃ for (b) 60, and (c) 120 min at 800 °C.	136
Figure 8.6 SEM image of sample (a) B-T2 and (b) sulfur-rich area. EDS elemental map of (c) sulfur, (d) calcium, and (e) oxygen.	137
Figure 8.7 The effect of the processing time on the sulfur content of the calcine in the presence and absence of CaCO ₃ additive at 800 °C, 5% S in burning coal (P _{SO₂} = 0.016 atm), and CO/CO ₂ of 4.	138
Figure 8.8 The effect of processing time on the sulfur reduction percentage in the calcine at 800 °C, 5% S in burning coal (P _{SO₂} = 0.016 atm), and CO/CO ₂ of 4.....	139
Figure 8.9 SEM images of CaCO ₃ particles processed for (a) 30, (b) 60, and (c) 120 min at 800 °C, 5% S in burning coal (P _{SO₂} = 0.016 atm), and CO/CO ₂ of 4.....	140
Figure 8.10 The particle size distribution of CaCO ₃ additive processed for 30, 60, and 120 min at 800 °C, 5% S in burning coal (P _{SO₂} = 0.016 atm), and CO/CO ₂ of 4.....	140
Figure 8.11 The effect of temperature on the sulfur content of the calcine in the presence/absence of CaCO ₃ additive at 60 min processing time, 5% S in burning coal (P _{SO₂} = 0.016 atm), and CO/CO ₂ of 4.	142
Figure 8.12 The effect of temperature on the sulfur reduction percentage in the calcine at 60 min processing time, 5% S in burning coal (P _{SO₂} = 0.016 atm), and CO/CO ₂ of 4.....	142
Figure 8.13 SEM images of CaCO ₃ particles processed for 60 min at (a) 700, (b) 800, and (c) 900 °C.	143

Figure 8.14 The particle size distribution of CaCO₃ additive processed at 700, 800, and 900 °C.

..... 144

List of Symbols

α	Extent of reaction
β	Heating rate
ΔG°	Standard Gibbs free energy
A	Pre-exponential factor
E	Activation energy
$f(\alpha)$	Function of the extent of reaction
$g(\alpha)$	Integral form of the reaction model
$h(P)$	Pressure function
$K(T)$	Temperature function
P_{SO_2}	Partial pressure of SO ₂ in the system
$P_{SO_2,eq}$	Partial pressure of SO ₂ in the equilibrium condition
R	Gas constant
S _R	Sulfur reduction percentage
t	Time
T	Temperature

List of Abbreviations

AOD	Argon oxygen decarburization
BVM	Bureau Veritas Minerals
CCD	Counter-current decantation
HPAL	High-pressure acid leaching
ICP-OES	Inductively coupled plasma optical emission spectrometry
LOI	Loss on ignition
PLS	Pregnant leach solution
RK-EF	Rotary kiln-electric furnace
SEM-EDS	Scanning electron microscope and energy dispersive spectroscopy
TGA-DSC	Thermal gravimetric analysis-differential scanning calorimetry
XRD	X-ray diffraction
XRF	X-ray fluorescence

Acknowledgements

First of all, I would like to express my sincerest gratitude to my supervisor, Prof. Leili Tafaghodi, for her support, guidance, and encouragement throughout my Ph.D. program. This work would not have been possible without her dedication and inspiration. Thanks for everything.

I would like to thank my examining committee members, Profs. D. Dreisinger, W. Liu, E. Asselin, and M. Pawlik, for their valuable suggestions that improved this work. I am thankful to Prof. Dreisinger for broadening my perspective on the mining sector and Prof. Liu for providing me with valuable insights.

Thanks to the financial support from Hatch Ltd., Mitacs Accelerate Program (IT08851), and UBC Four Year Doctoral Fellowship. I would also like to acknowledge Canadian Institute of Mining, Metallurgy, and Petroleum (CIM) for supporting students by providing various scholarships. Receiving CIM Vancouver Branch Graduate Student Award (2016) and MetSoc Pyrometallurgy Graduate Scholarship Award (2021) from CIM motivated me to go forward and pursue my goals.

My best thanks go to all my friends, particularly my officemates at FF 201 C and my colleagues at QMI 379 Lab (both of pyrometallurgy and hydrometallurgy sections), for their frequent help and support. I also wish to acknowledge ICP technician, Ms. Maureen Soon, and SEM technicians, Mr. Jacob Kabel and Ms. Heli Eunike, for their precious technical recommendations. My sincere thanks also go to Dr. Addie Bahi for his support and understanding when I served as a teaching assistant for “Nanofibre Technology” course.

I wish to express my deepest appreciation to my family, without whom none of my achievements would have been possible. I owe a great debt of gratitude to my father, whose memory propels me

forward every single day of my life. Words cannot express how grateful I am to my mother for her endless love and unconditional support. A sincere word of appreciation is extended to my brothers and sister-in-law for their encouragement and moral support. Finally, special thanks to my dear Shanli, for her love and understanding during this arduous endeavour.

To my father

whose memory is always with me

To my mother

for her love, sacrifice, and support

Chapter 1: Introduction

Nickel is a strategic metal mostly used in stainless steel, superalloys, high-temperature alloys, non-ferrous alloys, and batteries [1–4]. Almost two-thirds of the nickel produced globally is consumed for stainless steel production. The increasing production of stainless steel results in higher demand for nickel production [5]. Consequently, the global nickel consumption was increased from 1.1 to 1.6 Mt in the first decade of the 21st century, with an annual increase rate of 2.9% [6]. While at present times, nickel is mostly used in the stainless steel industry, it is predicted that the rapid growth of the battery industry impacts the nickel market in the future [7].

Nickel resources are divided into two types: sulfides and laterites. Overall nickel reserves are estimated at 299.6 million tonnes [5], with laterites representing about 60% of the deposits. Before 2000, nickel was primarily produced from sulfides (60%) due to accessible upgrading methods, low energy consumption of the extraction process, and availability of high-grade ore. Considering the continuous depletion of sulfides over the last few years and the high demand for nickel, laterite ores are expected to constitute the bulk of future nickel production [8, 9]. Currently, it is estimated that 70% of the global nickel is produced by processing laterites [10]. The rapid growth of the stainless steel industry has led to an increase in global nickel demand. In response, China has developed about 30 nickel smelters for nickel pig iron (NPI) production, accounting for about 30% of global nickel production [8–10].

With respect to the nickel-bearing minerals in the ore, laterites are divided into two main types: limonite and saprolite. Limonites represent about 60% of the total laterite resources, while saprolites account for 32%. The remaining 8% is in the mixed limonite and saprolite layer, known as smectite [8, 11, 12]. The main extraction route for limonite ores is the hydrometallurgical

process, while saprolites are typically processed via the pyrometallurgical route. The low iron and high magnesium contents of the saprolite ore are the main reasons for using pyrometallurgical methods for saprolite ores [13, 14].

The rotary kiln-electric furnace (RK-EF) operation is the predominant process for extracting nickel from saprolitic ores. This process involves drying, calcination and partial reduction, smelting, and refining to produce ferronickel or nickel sulfide matte. Calcination and partial reduction of the ore are performed in a rotary kiln at 800-1000 °C. Calcination is an energy-intensive step in pyrometallurgical extraction of nickel where the required energy is provided by fuel combustion [13]. Various types of fuel, such as coal, oil, and natural gas, are used in the rotary kiln [13, 15]. The composition of the calcine affects the final impurity content of ferronickel [16, 17].

Sulfur is one of the deleterious impurities in ferronickel that interacts with alloy components and decrements the mechanical properties of nickel alloys [18]. Since laterites typically contain low amount of sulfur (~0.01%), it is believed that the majority of sulfur in crude ferronickel originates from the fuel and reductant added in the rotary kiln [19, 20]. Bituminous coal is mostly used as a fuel in rotary kilns. This type of coal typically contains sulfur in the range of 0.2-10% [21–24]. Therefore, it is crucial to monitor the behavior of sulfur in the rotary kiln to control the sulfur content of the calcine. Decreasing the sulfur content of the calcine will reduce the load of the refinery, and hence the overall cost of the process.

The main objective of this study is to investigate the behavior of sulfur during laterites calcination process in the rotary kiln. As an initial step, the kinetics of the main reactions that occur during calcination stage is examined by a novel approach of combining model-free and model-fitting methods (chapter 5). In the next step, the sulfurization reactions are identified and the effects of

sulfur content of the fuel, e.g., coal, reducing atmosphere, gas flow rate, and temperature on the sulfur content of the calcine are investigated (chapter 6). The kinetics of sulfur deportment is studied by variation of temperature and partial pressure of SO_2 (P_{SO_2}) at various processing times (chapter 7). Finally, an efficient method to decrease sulfur transfer from fuel to the calcine is proposed (chapter 8).

Chapter 2: Literature Review

2.1 Nickel Resources

Nickel is the 24th most abundant element in the earth's crust, accounting for its 0.008% [25]. Nickel resources are available across the world, mostly in Indonesia, Australia, Brazil, Philippines, New Caledonia, Russia, and Canada [10, 26]. Nickel deposits are divided into two major groups, laterites and sulfides.

Sulfide ores typically contain 1.5-3 % Ni and mostly include Cu, Co, and Fe sulfides. Laterite ores are composed of oxide minerals and mostly contain 1.3-2.5% Ni [13]. Laterites constitute a considerable amount of free water and hydroxides.

Since the current thesis is directed at processing of nickel laterites, the literature survey is focused on the composition and processing of nickel laterites, while processing sulfide ores is briefly discussed in the following section.

2.2 Nickel Sulfide Ores

Sulfide ores are mostly formed through volcanic processes and the intrusion of molten magma on the earth's crust [13]. The most common nickel-bearing mineral is pentlandite ((Fe,Ni)₉S₈), in which the atomic ratio of iron to nickel is in the range 0.34 to 2.45. Other common minerals associated with pentlandite are pyrrhotite (Fe₈S₉) and chalcopyrite (CuFeS₂). Extraction of nickel from sulfide ore involves several steps, including grinding, upgrading, roasting, and smelting. First, sulfide ore is upgraded via flotation. The concentrate is then roasted above 700 °C in the air atmosphere. The roasted product is smelted in an electric or flash smelting furnace at 1250-1300 °C to produce molten matte. Then, iron is oxidized and removed as the slag in the converter. Subsequently, high-grade matte is refined to produce pure nickel (99.95%) [13, 27, 28].

2.3 Nickel Laterite Ores

The nickel contents in the oxide ores are variable and relatively low compared to the sulfide minerals. The oxide ores are usually called lateritic ores due to their formation process. Prolonged tropical weathering of “ultramafic” rocks containing ferro-magnesian minerals resulted in the formation of laterite deposits. Chemical weathering, also known as serpentinization, involves the dissolution of the original minerals, followed by the movement of the dissolved elements in solution and their precipitation in another location. Laterites are generally formed near the surface. Therefore open-pit mining techniques are used for removing them from the crust of the earth [8, 29, 30].

The weathering process is initiated by the dissolution of olivine, $(\text{Mg,Fe})_2\text{SiO}_4$, by groundwater. Olivine is an iron magnesium silicate that contains minor amounts of nickel. Weathering of olivine results in the dissolution of iron, magnesium, and nickel. Iron oxidizes and precipitates out first in the form of goethite, $\text{FeO}(\text{OH})$, and hematite, Fe_2O_3 . Hence, the concentration of iron is higher near the earth's surface. The dissolved nickel and magnesium are transferred downward. [25, 31]. Nickel substitutes into magnesia silicate compound in place of either iron or magnesium due to similar ion radii [32].

As described above, the net effect of the prolonged weathering phenomena is the formation of a profile of the minerals from the surface to the bottom of the bedrock [33, 34]. The schematic of a laterite profile, including its chemical composition, is shown in Figure 2.1.

Laterite Profile	Common Name	Minerals	Approximate Analysis (%)			
			Fe	MgO	Ni	Co
Ferricrete	Ferricrete	Goethite	> 50	< 0.5	< 0.8	< 0.1
Limonite	Limonite	Hydrated FeO(OH)	40 - 50	0.5 - 5	0.8 - 1.5	0.1 - 0.2
Smectite	Smectite	Nontronite, Saponite	10 - 30	5 - 15	0.6 - 2	0.02 - 0.1
Saprolite	Saprolite	Serpentine, Chlorite, Sepiolite, Talc	10 - 25	15 - 35	1.5 - 4	0.02 - 0.1
Serpentinized Peridotite	Bedrock	Peridotite	5	35 - 40	0.3	0.01

Figure 2.1 Schematic of nickel laterite profile in a tropical climate, including approximate Ni, Fe, Co, and MgO contents of the main layers (wt%) [13].

2.3.1 Ferricrete and Limonite Zones

As shown in Figure 2.1, the main layers in a typical laterite profile are ferricrete, limonite, smectite, saprolite, and bedrock. The crust, also known as ferricrete, is the layer from which most of the MgO and SiO₂ have been leached by rain and vegetative acids [13, 33]. Limonite layer is commonly referred to as oxide deposit. The limonite zone mainly contains goethite and amorphous ferric hydroxide. Nickel substitutes into goethite structure in place of iron. This zone includes a low amount of 0.5-5% magnesia, and the nickel grade is in the range of 0.6-2 wt% [8, 13].

2.3.2 Saprolite Zone

The lower region of the laterite profile attributes to the hydrous magnesium silicate deposit, generally known as saprolite layer. The main minerals are lizardite, Mg₃(Si₂O₅)(OH)₄, from serpentine group, chlorite, (Ni₅Al)(Si₃Al)O₁₀(OH)₈, and talc, Mg₃Si₄O₁₀(OH)₂ [8, 13, 35].

The iron content of this layer is considerably lower than the upper layer. Saprolite layer has relatively high nickel and magnesia contents. Nickel grade in the saprolite layer is in the range of 1.5-4 wt% [8, 13]. While limonite layer is mainly composed of hydroxides, saprolite zone mostly contains hydrous magnesium silicates.

2.3.3 Smectite Zone

The transition layer between limonite and saprolite layers is composed of clay silicate deposit known as smectite. The major minerals in the smectite layer are nontronite, $\text{Na}_{0.3}\text{Fe}_2(\text{Si},\text{Al})_4\text{O}_{10}(\text{OH})_2 \cdot n(\text{H}_2\text{O})$, and saponite, $(\text{Ca}_{0.5}\text{Na})_{0.3}\text{Mg}_3(\text{Si},\text{Al})_4\text{O}_{10}(\text{OH})_2 \cdot 4\text{H}_2\text{O}$. Smectite is mostly formed in less severe weathering conditions like dry or cool climates, where silica is leached to a lesser extent compared to humid tropical regions [33]. The smectite layer is found in “dry laterite” mostly formed in Australia where low water is available for laterite formation. [36]. The typical grade of nickel in the smectite layer is in the range of 0.6-2 wt% [8, 13].

2.4 Processing of Nickel Laterite Ores

The chemical composition of the ore is the main factor determining the choice of the extraction route. Limonite ore, due to its low MgO content, is typically processed with a hydrometallurgical route. In addition, goethite, as the main nickel-bearing mineral in limonite ore, is dissolved efficiently by hydrometallurgical routes. On the other hand, low iron content of saprolite ores makes it suitable for nickel-rich ferronickel production via pyrometallurgical method [13].

The main nickel extraction processes from laterites are shown in Figure 2.2. The hydrometallurgical routes, including high-pressure acid leaching (HPAL) and Caron process, are used for the extraction of nickel and cobalt from limonite ore. The pyrometallurgical route commonly used to produce ferronickel or nickel matte from saprolite ore is rotary kiln-electric

furnace (RK-EF) [13, 37]. Another pyrometallurgical route for nickel extraction is nickel pig iron production. The process which has been recently developed in China is based on the ore reduction in blast furnace and electric arc furnace [38].

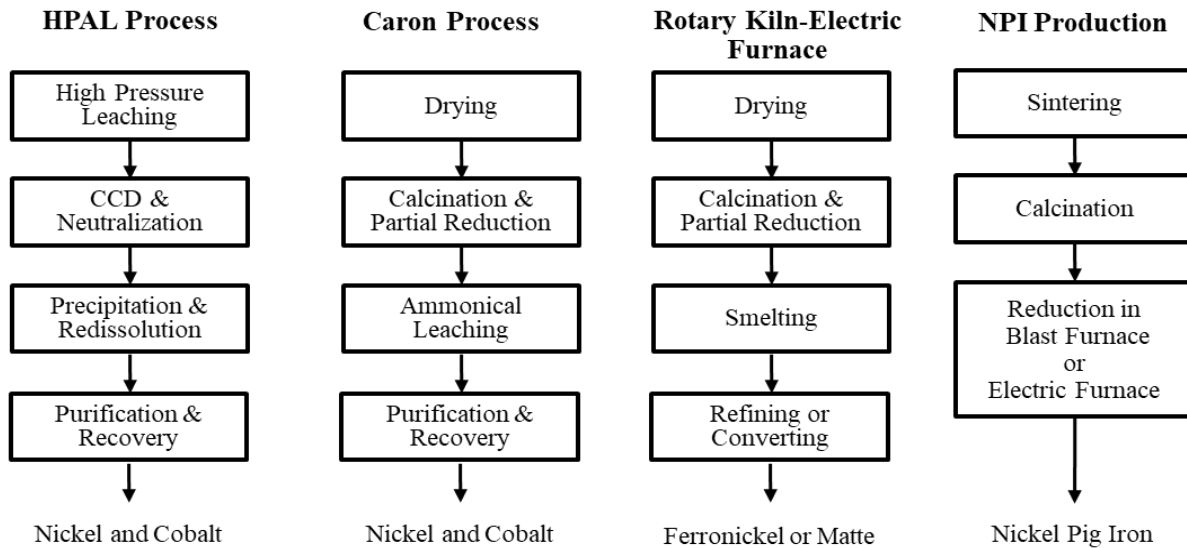


Figure 2.2 Generalized flow sheets of nickel laterite processing [6, 10, 37].

2.4.1 High-Pressure Acid Leaching (HPAL)

High-pressure acid leaching starts with sulfuric acid leaching in an autoclave at 240-270 °C under 33-55 atm [39]. The heated slurry of nickel laterite is fed to the autoclave, and after 1 to 2 hours, a pregnant leach solution (PLS) is obtained. The recovery of nickel in PLS is typically higher than 95%, while only 3% of the iron in the feed is dissolved in the solution [13]. It is worth mentioning that the dissolved iron can be hydrolyzed and precipitate as hematite and jarosite in the autoclave. In the next step, solids are separated from liquids by the counter-current decantation (CCD) process. Nickel and cobalt can be recovered from the PLS with various processing methods. Precipitation as sulfide or hydroxide compounds, and direct solvent extraction are the main recovery methods [37]. HPAL is not economical for saprolite ores because of their high MgO

content, and subsequently, high acid consumption. The flowsheet of HPAL process is shown in Figure 2.3.

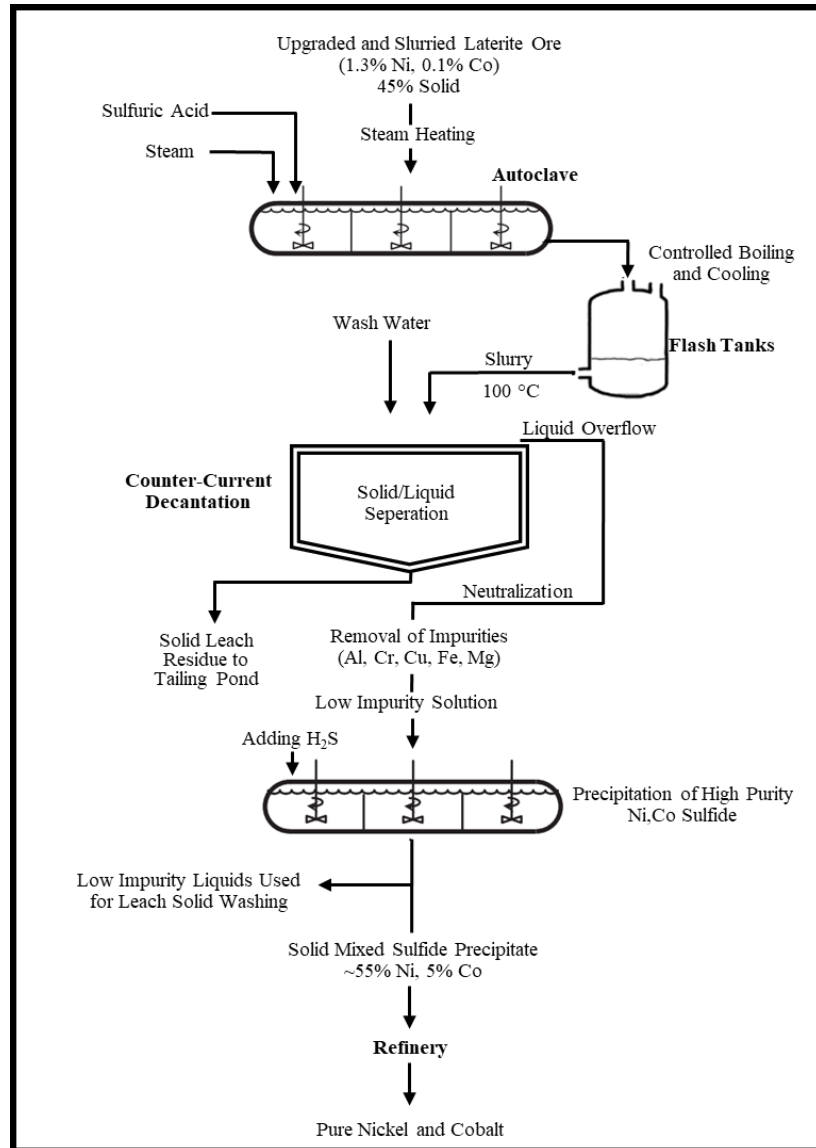


Figure 2.3 Process flowsheet for high-pressure acid leaching (HPAL) [13].

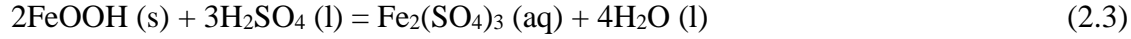
The main chemical reactions that occur in the autoclave are presented in equations 2.1-2.5 [13]:

a) Nickel and cobalt leaching:





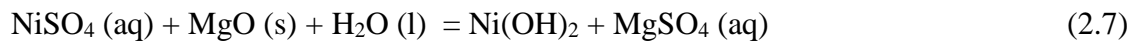
b) Dissolution of goethite and precipitation of iron as hematite and jarosite



As mentioned above, mixed-sulfide precipitation process is utilized to precipitate nickel and cobalt sulfides using hydrogen sulfide gas. Finally, the mixed-sulfide product is transferred to the refining step to recover nickel and cobalt. The precipitation reaction in mixed-sulfide process is presented in equation 2.6 [13]:



Another method for nickel and cobalt recovery is precipitating them as hydroxides. In this process, known as mixed-hydroxide precipitation, the leached solution from autoclave is reacted with magnesia slurry to precipitate nickel and cobalt as mixed hydroxides. The solution is thickened and filtered to separate nickel and cobalt hydroxides. In the next step, nickel and cobalt, in their metallic form, are recovered from hydroxides by refining [13]. The refining includes leaching by ammonia ammonium-carbonate followed by electrowinning [40]. The reaction for the formation of nickel hydroxide using MgO is shown in equation 2.7 [41]:



The main advantage of HPAL is the high recovery of nickel and cobalt, generally above 95%. In addition, it does not need high-temperature processes such as calcination and smelting. However, the process involves some drawbacks like hot corrosion of the autoclaves, expensive construction

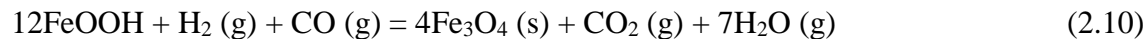
materials for autoclaves, and high maintenance costs. Environmental impacts are another concern associated with HPAL. Generating a large quantity of liquid waste, the necessity for neutralization of sulfuric acid after the leaching process, and disposal of magnesium sulfate are the main environmental concerns of the process.

2.4.2 Caron Process

Caron process developed in the 1920s is the oldest hydrometallurgical route developed for processing limonite ore [42]. However, a mixture of limonite and saprolite ores can also be treated with Caron method. The main steps of Caron process are [42]:

- a) Drying and grinding the raw ore
- b) Reduction in the multiple hearth furnaces
- c) Leaching with ammoniacal-ammonium carbonate
- d) Recovery of metal from the solution

Initially, the ore is dried to decrease moisture content from ~35% to ~8% [26]. The dried ore is ground and fed to the hearth furnace for the reduction step. Nickel and cobalt oxides are reduced to metallic form, while the majority of iron is present as magnetite in the calcine [43]. The main reduction reactions in the hearth furnace are presented in equations 2.8 to 2.10 [13]:



The next step is leaching of the calcine by ammonia-ammonium carbonate solution to dissolve metallic nickel and cobalt according to reactions 2.11 and 2.12 [13].



The next step is boiling the solution to remove ammonia and precipitate nickel carbonate followed by calcination of the carbonate to produce a mixture of nickel (60%) and nickel oxide (40%). Finally, the calcine is reduced in the belt furnace at 900-1000 °C to produce nickel [13, 26].

2.4.3 Ferronickel Production by Rotary Kiln-Electric Furnace Process

Pyrometallurgical processing of laterites is another established route for extracting nickel. This process can be divided into two subsets based on the final product: 1. Smelting process to produce nickel matte and 2. Rotary kiln-electric furnace (RK-EF) process to produce ferronickel.

Rotary kiln-electric furnace process is generally used for saprolite ores. The lower iron content of saprolite compared to limonite ensures that the final product (ferronickel) is not extremely diluted with iron [13].

The flowsheet of the RK-EF process is shown in Figure 2.4. The major steps are [13]:

- 1- **Drying:** removal of entrained water from the ore.
- 2- **Calcination and partial reduction:** breaking the chemical bonds between water and various constituents of the ore by heating the ore, and partial reduction of nickel and iron oxides to metallic form.
- 3- **Smelting:** reduction of remaining nickel and iron oxides by smelting the calcine in an electric furnace.
- 4- **Refining:** removal of impurities such as sulfur and phosphorus from the crude ferronickel.

All steps of the RK-EF process are discussed in further detail in the following sections.

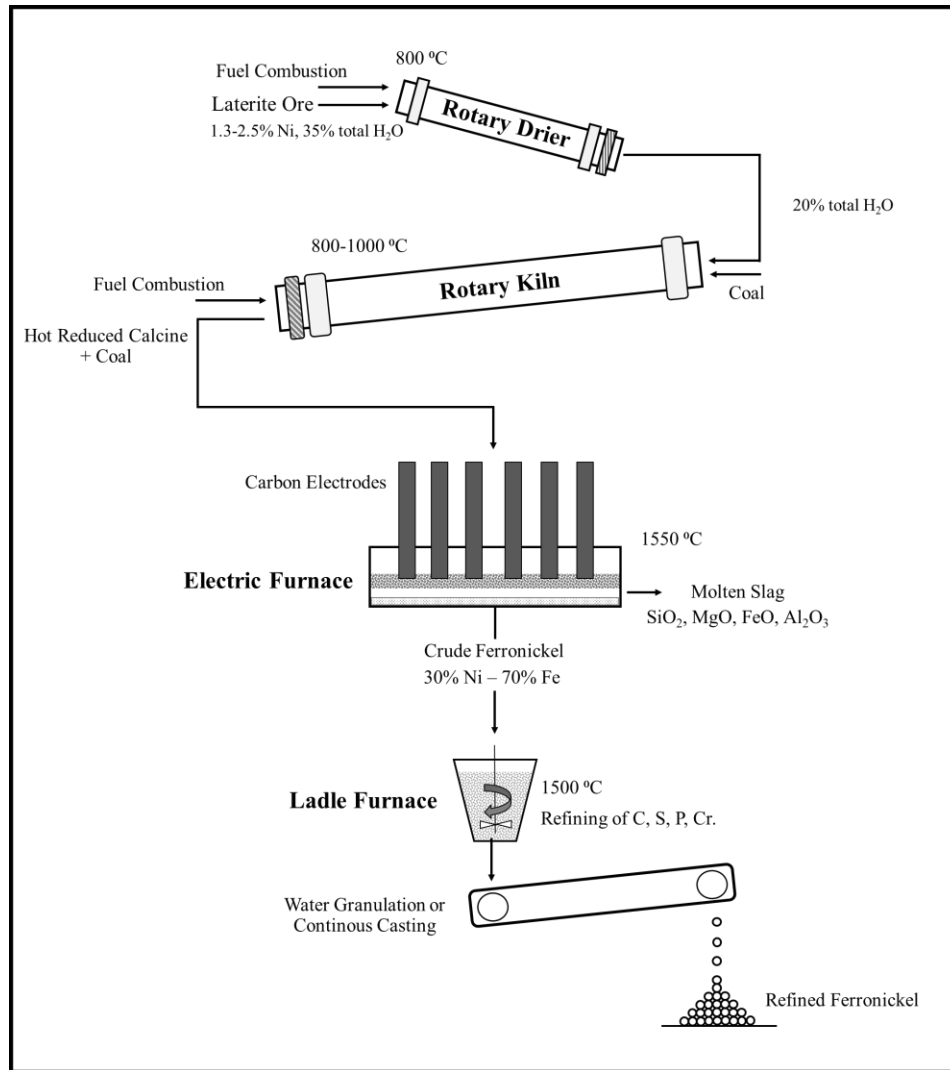


Figure 2.4 Rotary kiln-electric furnace process flowsheet for ferronickel production [13].

2.4.3.1 Pre-treatment and Drying

Upgrading the ore is the first step in ferronickel production. As mentioned in section 2.3, laterite ore has a heterogeneous composition, including different silicates such as serpentine, talc, and chlorites. Moreover, weathered minerals with high nickel content are generally softer than precursor rocks. By means of screens and filters, larger particles that are mainly hard and lean in nickel can be separated from small and nickel-rich particles. This upgrading step decreases the

amount of the raw material that will go through the high-temperature steps. Upgrading the ore minimizes energy consumption, the amount of reagent materials, and shipping cost. It is worth mentioning that the nickel content of the upgraded ore is typically only 1.2 to 2 times greater than the original ore [13].

Laterite ores are mostly sticky and include a considerable amount of moisture up to 40% [13, 44]. It is necessary to remove the water in the upgraded ore before feeding it to the electric furnace in order to avoid any explosions. The water is removed in two steps: drying and calcination. Wet ore is continuously fed to the dewatering kilns to remove moisture. The ore should not be sticky as it will adhere to the conveyor belts. Conversely, it should not be excessively dusty because it creates problems for ore handling. Hot air and gas resulted from fuel combustion are blown to the dewatering kilns to evaporate moisture. The flow of the hot gas and the ore are in the same direction to avoid mud ring formation in the kiln. The dust in the off-gas is recovered via electrostatic precipitators and recycled to the dryer kiln or calcination kiln. The product of the drying step is partially dewatered ore, which is transferred to the calcination kiln [13].

2.4.3.2 Calcination and Partial Reduction

The ore obtained from the drying step has 15-20% residual free water and 10-12% crystalline water [28]. This high amount of water needs to be removed from the ore prior to smelting. Rotary kilns are commonly used for calcination and pre-reduction processes. The main objectives of processing the ore in the calcination kiln are in the following [13, 28, 45]:

- 1- Evaporation of the remaining water in the ore to prohibit explosion during the following smelting step.
- 2- Reduction of about 25% of nickel oxide to the metallic nickel.

- 3- Converting most of the hematite to wustite and obtaining about 5% metallic iron.
- 4- Adding sufficient coal (3.5-11 wt% of the ore) to the rotary kiln considering that some coal should remain in the calcine for the final reduction in the subsequent smelting process.
- 5- Preparing high-temperature calcine (800-900 °C) as the feed for the smelting furnace to decrease energy consumption.

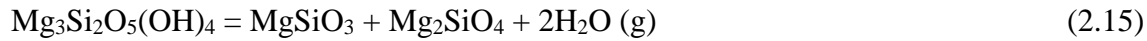
Industrial rotary kilns are typically 3-6 m in diameter and 70-185 m long with 40-165 ton/hr capacity. The energy is obtained by burning fuels such as coal, oil, and natural gas. The kiln is designed for continuous operation with a slope of about 4° from horizontal to facilitate the downward motion of the solids. Rotation of the kiln (~1 rpm) and counter-current flow of the hot gas and solid material enhance heat transfer and reactivity between solids and gases. The air can be purged along the length of the kiln at different locations to control the atmosphere of the kiln [46, 47]. Additional coal might be charged in the middle of the kiln to control the reducing atmosphere and heat transfer in the kiln [48]. The calcination stage mainly includes dehydroxylation and dissociation reactions. At 350-400 °C, dihydroxylation and transformation of goethite [FeO(OH)] to hematite occurs [49, 50]. Additionally, at 600-700 °C, hydrated magnesium silicate is dissociated, and the hydroxyl group is removed [49, 51, 52]. Partial reduction reactions also occur in the rotary kiln. About 25% of nickel oxide is reduced to metallic nickel, and most of the hematite is reduced to wustite [13]. The outputs of the rotary kiln are calcine and off-gas at 800-1000 °C and 250-400 °C, respectively [13]. The dust in the off-gas, which accounts for 15-20% of the kiln feed, can be pelletized and recycled back to the rotary kiln. The calcine should contain enough coal for the complete reduction of the remaining iron and nickel oxides in the next step, i.e., the electric furnace.

The main reactions that occur in the rotary kiln are summarized as follows (reactions 2.13-2.23) [13, 46]:

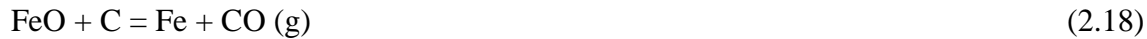
a) Complete evaporation of the remaining water in the ore:



b) Thermal dissociation of the laterite minerals, i.e., goethite and serpentine complex compounds in limonite and saprolite ore, respectively:



c) Direct reduction of nickel and iron oxides by carbon:



d) Indirect reduction of nickel and iron oxides by reducing gases, i.e., carbon monoxide:



2.4.3.3 Smelting

The product of the calcination step is fed to the electric furnace for complete reduction of nickel oxide to metallic nickel. During the smelting process, stable oxides form the slag phase and separate from ferronickel. Molten slag contains SiO_2 , MgO , FeO , Al_2O_3 , and negligible amount of nickel (0.07-0.2%). The slag is tapped from the higher taphole at 1550-1600 °C. The crude

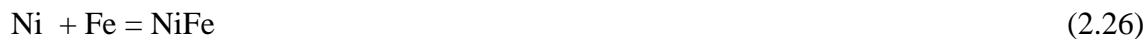
ferronickel containing 60-80% Fe and 20-40% Ni, is tapped from the lower taphole at 1450-1500 °C. Low thermal conductivity of the slag (3-7 W/m.K) causes a difference in the slag and ferronickel temperatures and a decrease in the temperature from top to the bottom of the electric furnace [53, 54]. The main reason for effective separation of slag and ferronickel is the immiscibility of these two phases. Ferronickel with density of $\sim 7 \text{ g/cm}^3$ settles at the bottom of the furnace, while the slag with the density of $\sim 3 \text{ g/cm}^3$ floats on the top. The crude ferronickel is transferred to the refining step using a ladle. The slag is either sent to a waste dump or granulated to be used as building material. The off-gas is completely burned, dedusted and released to the atmosphere or used in the drying kilns [13, 14].

The main reactions that occur in the electric furnace are summarized as follows [13]:

a) Reduction of iron and nickel oxides to metallic iron and nickel



b) Formation of ferronickel by melting and alloying of nickel and iron at 1450 °C



c) Formation of molten ionic slag from the unreduced oxides in the calcine



The ferronickel slag contains cations and anions such as Mg^{2+} , Fe^{2+} , and SiO_4^{4-} . Depending on the composition of the feed, the slag is mainly composed of 40-55% SiO_2 , 20-35% MgO , 5-20% FeO , 1-7% CaO , and 1-2% Al_2O_3 [13, 55]. Generally, the slag is tapped at 50 °C higher than its melting point, i.e., 1500 °C, to obtain appropriate fluidity and easy separation from the ferronickel. The nickel recovery of the smelting process is in the range of 90-98%.

The main drawback of the smelting process is producing a large volume of slag, 14-15 times higher than ferronickel, which results in high energy consumption of the process [13].

The industrial electric furnaces are either circular with three electrodes or rectangular with six electrodes. Carbon electrodes are made in a cylindrical shape with 1-2 m diameter and 20-25 m height. The energy required for the smelting process is obtained by heating joule, which is provided by high current density of 10-15 KA/m² between the suspended electrodes.

Nowadays, the shielded arc approach is commonly used for ferronickel production. In the shielded arc method, most of the power is transferred directly from the arc to the feed, while in the immersed electrode method, the overlaying calcine is melted by resistance heating of the slag (Figure 2.5). The shielded arc method has some advantages over the immersed electrode method. Lower consumption of electrodes, higher rate of melting, slower degradation of refractories, and smaller size of the electrodes are the main benefits of the shielded configuration [56].

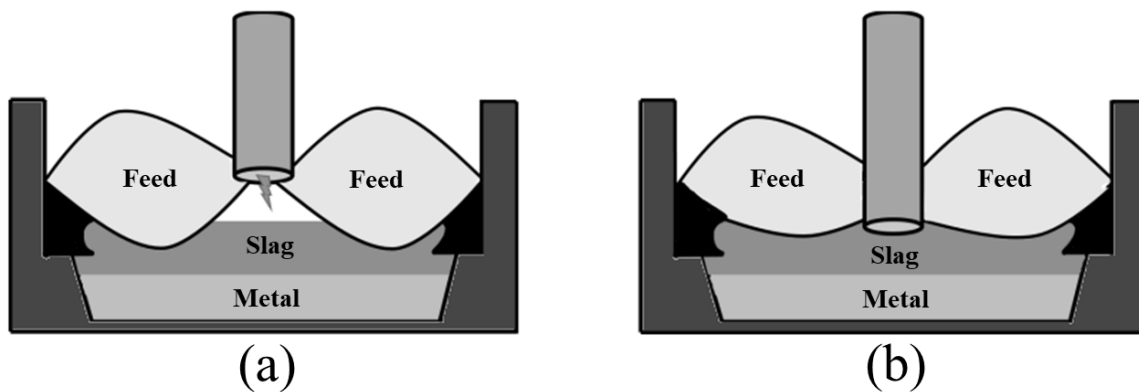
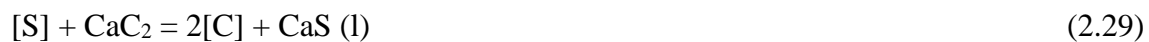


Figure 2.5 Two configurations of electric furnace: (a) shielded-arc, and (b) immersed arc electric furnace [56].

2.4.3.4 Refining

The crude ferronickel obtained from the electric furnace contains impurities, which should be removed in the refining step. Generally, crude ferronickel contains up to 0.06% phosphorus and 1% sulfur, while the maximum acceptable phosphorus and sulfur contents of the commercial ferronickel are 0.02% and 0.05%, respectively [13]. Phosphorus and sulfur removal are carried out in the ladle furnace at 1550-1600 °C by tapping the slag formed through different refining stations, i.e., dephosphorization and desulfurization.

Phosphorus removal is done by adding lime (CaO) and oxygen to the molten ferronickel. Lime is added before and during the process to obtain efficient mixing of lime with the ferronickel. Oxygen is also blown into the molten ferronickel by refractory-coated stainless steel lances to remove impurities such as carbon and silicon from the crude ferronickel. Sulfur removal is carried out by adding calcium carbide (CaC₂) into the molten ferronickel. Calcium sulfide is formed in the slag, which is removed by tipping the ladle. Other reagents such as CaO, CaCO₃, CaSi, Na₂O, and Na₂CO₃ are also used to remove sulfur. The representative reactions of phosphorous, sulfur, and carbon removal are given as follows [13]:



2.4.4 Matte Production by Rotary Kiln-Electric Furnace Process

About 10% of the laterite smelting plants produce Ni-Fe-S matte. Most steps of this process are similar to the ferronickel production except reagents addition in the rotary kiln and the requirement for extra steps like converting and roasting. PT Inco in Indonesia and Le Nickel in New Caledonia

are the two primary nickel matte producers in the world. The extraction process at PT Inco plant is discussed in section 2.5.3.

Figure 2.6 shows the process flowsheet for matte production at PT Inco operations. Initially, the raw ore is dried in the dryer kiln. The partially dewatered ore is fed to the rotary kiln for calcination and partial reduction. Molten sulfur is sprayed into the discharge end of the rotary kiln to sulfurize the calcine. The sulfurized calcine containing ~1% sulfur is fed to the electric furnace to separate oxides and obtain molten matte with the approximate composition of 63% iron, 26% nickel, 10% sulfur, and 1% cobalt. The next step involves removal of iron from the matte by the Peirce-Smith converter. As shown in Figure 2.7, there are three main steps in the Peirce-Smith converter. First, a matte with high iron content is charged to the converter. Subsequently, the air is blown into the converter to oxidize the iron present in the molten matte. Finally, the slag phase containing the oxidized iron is poured out to obtain matte with low iron content. Since the main reactions that occur in the converter are highly exothermic, external heat is not required for this process. The approximate composition of the converted matte is 78% nickel, 20% sulfur, 1% iron, and 1% cobalt. The matte is solidified and granulated by spraying water and sent for the roasting to produce pure nickel [13, 32].

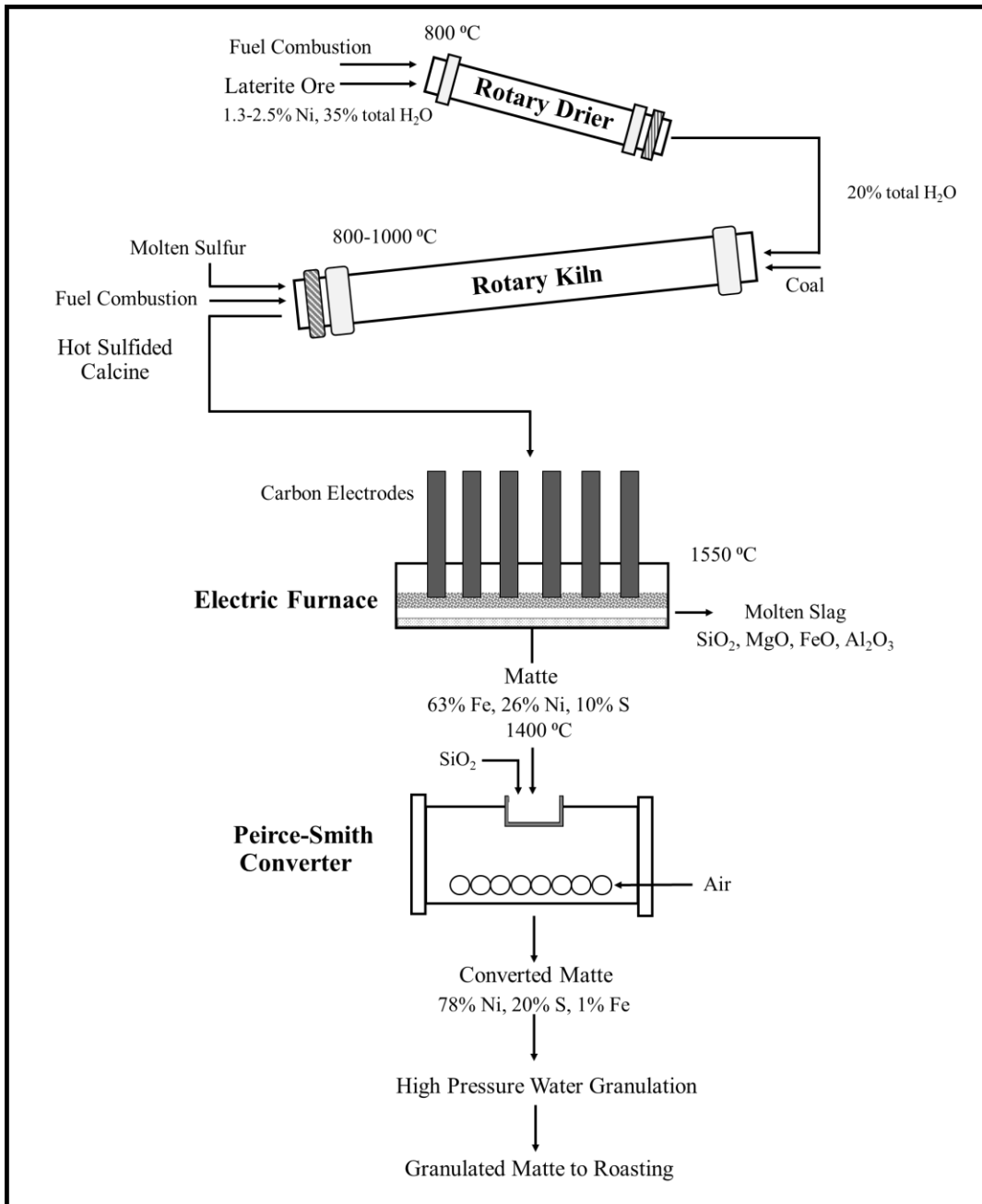


Figure 2.6 RK-EF process flowsheet for nickel matte production [13].

Nickel and iron sulfurization reactions in the rotary kiln are presented by equations 2.31 and 2.32 [13]:





The main oxidizing reactions in the Peirce-Smith converter are given in equations 2.33 and 2.34

[13]:

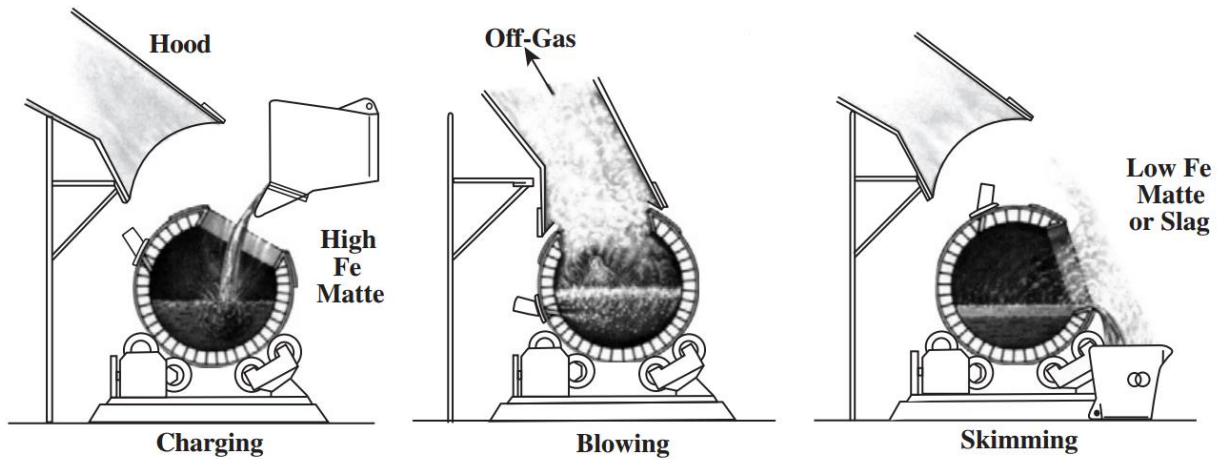


Figure 2.7 Schematic of the process steps in Peirce-Smith converter [13].

Converted matte is roasted to remove sulfur and obtain metallic nickel or nickel oxide as the final product. The roasting process is performed in the fluidized-bed roaster, where oxygen-enriched air is purged to the system to oxidize the matte at 1050 °C. Since the chemical reactions in the roasting process are strongly exothermic, the roaster needs to be water-cooled to avoid over-heating. The oxidation roasting reaction of the matte is shown in equation 2.35:



The final product of the roasting step generally consists of 76% nickel, 23% oxygen, 0.5% iron, and 0.003% sulfur [13]. Occasionally, nickel oxide is directly sent for stainless steel production.

However, the roasting product is generally reduced to obtain metallic nickel. The reduction is carried out at 1000 °C, where the reducing atmosphere is provided by air-deficient combustion of hydrocarbons. Nickel oxide is reduced to metallic nickel by reacting with carbon monoxide and hydrogen. By recycling the dust to the roaster, nickel recovery in the roasting plant reaches almost 100%.

2.4.5 Nickel Pig Iron (NPI) Production

Nickel pig iron (NPI) production has been expanded in China since the early 2000s due to the increased demand for nickel and the domestic growth of the stainless steel industry in China. NPI is a low-cost alternative for nickel in the stainless steel industry. NPI is considered a low-grade ferronickel that contains about 8-15% nickel [10, 38].

The NPI production route is quite similar to the conventional pig iron process. Raw materials including ore, coke breeze, and fluxes are mixed together and sintered to form agglomerates. Then, the sintered materials are smelted in the blast furnace or electric arc furnace to separate NPI from slag. The main technical challenges associated with the sintering and smelting route are corrosion of the furnace refractories due to the addition of fluxes, high viscosity of the slag, and high coke breeze consumption [6]. Several small pig iron blast furnaces in China are modified for NPI production without significant capital cost. Raw laterite ores are generally imported from Indonesia and Philippines. However, enactment of the law to prohibit the exportation of raw ores from Indonesia in 2014, diminished NPI production in China. Therefore, Chinese NPI producers have relocated NPI plants outside of China, mainly in Indonesia. Tsingshan plant located in Fujian province of China is an example of NPI production using RK-EF process. Very fast construction, standardized equipment, low custom design, high iron recovery, and high production using parallel

lines are the main differences with conventional RK-EF plants. Recently, due to the rapid growth of battery and electric vehicle industries, the demand for high purity nickel has increased. Thus, it is predicted that NPI producers modify RK-EF process for matte production to obtain high purity nickel as a final product [6, 10, 38, 57].

2.5 Nickel Laterite Plant Specification (Pyrometallurgical Processes)

Since the current study deals with processing nickel laterites via RK-EF route, the industrial specifications of RK-EF extraction process are examined for three well-known plants, namely Cerro Matoso in Colombia, Hyuga in Japan, and PT Inco in Indonesia. It should be noted that the publicly available data for industrial plants are very limited. The following evaluation is based on the scattered data from the available articles and one comprehensive plant survey published in 2006 [19, 45, 48, 58–62]. In the absence of a more recent plant survey, the process specifications mentioned below might vary from the current industrial values.

2.5.1 Cerro Matoso (Colombia)

The Cerro Matoso deposit was first reported by Richmond Petroleum Co. in 1958. The mine started operating in 1982 [58]. This deposit which is located in the northwest of Colombia, contains about 25 million tonnes of nickel laterite ore [59, 60]. The typical nickel and iron content and SiO₂ to MgO ratio of the ore at Cerro Matoso are presented in Table 2.1.

Table 2.1 Nickel and iron content and SiO₂/ MgO of the raw ore in industrial plants [45].

Mining plant\Feed composition	Ni (wt%)	Fe (wt%)	SiO ₂ /MgO
Cerro Matoso (Colombia)	2.2	15.2-15.4	2.8
Hyuga (Japan)	2.1-2.5	11-23	1.5-1.6
PT Inco (Indonesia)	1.8-1.9	20	2

The RK-EF process is used for producing ferronickel at Cerro Matoso operations. The ore is selectively mined using a conventional open cut method and stored in different piles. In order to provide homogeneous feed materials with accurate chemical composition, different piles are used in rotation. The wet ore, containing 15-25% moisture (depending on the season), is dried to 11-16% moisture in the two dryers working in parallel. The dried ore is passed through the screen to reject coarse rocks larger than 50 mm [60]. The sieved ore is mixed with 4-5% coal and fed to the two gas-fired rotary kilns. The counter-current direction of hot gas and solid feed is designed for higher thermal efficiency, and leads to evaporation of crystalline water, decomposition of complex compounds, and partial reduction of iron and nickel oxides [13, 63]. About 90 to 95% percent of trivalent iron is reduced to divalent state, and the rest is converted to metallic iron. About 20% of nickel oxide is reduced to metallic nickel in the rotary kiln. The calcined ore is fed to the electric arc furnace for reduction to ferronickel at temperatures around 1600 °C [45]. The product, which contains approximately 35% nickel, is tapped at 1450-1470 °C [45]. The crude ferronickel contains 0.45-0.65% sulfur which is lowered to 0.06% at the ladle refining stage. The refining is operated in a combustion oxygen blowing system (COBS) and ladle furnace by adding CaO and Al. Sulfur removal from ferronickel occurs via reaction 2.36:



The slag produced from the refining step is cooled down and crushed, followed by the recovery of the entrapped ferronickel by magnetic separation [60, 64]. The slag is produced at the rate of 16:1 of ferronickel; the ratio is expected to increase with the continuous decline of the nickel grade in the feed. The nickel content of the laterite ore decreased from 3.2 to 1.66% during 1982 -2019

[10]. Declining the ore grade decreased production capacity from 55 to 41 kt/y during 2001-2019

[10]. The typical final chemical composition of ferronickel is presented in Table 2.2.

Table 2.2 Typical chemical composition of ferronickel at different plants (wt%) [45].

Ferronickel/Composition	Ni	Fe	Co	C	S	Si	P	Cr
Cerro Matoso	34-36	64	<1	<0.04	<0.06	<0.7	<0.04	<0.03
Hyuga (Low C)	17-28	70-81	0.85-1.4	<0.02	<0.03	<0.3	<0.02	<0.3
Hyuga (High C)	16	77	<0.8	3	<0.03	<0.5	<0.05	<2.5
PT Inco	76-80	>0.7	1	-	18-22	-	-	-

2.5.2 Hyuga (Japan)

Hyuga ferronickel smelting operation is located on the coast of Hyuga city, Miyazaki prefecture, Japan. The main steps of the process are similar to Cerro Matoso, with differences in operational parameters, capacity, reagents, and fuel type.

The typical ore composition is presented in Table 2.1. While the Ni content of the ore at Hyuga is comparable with that of Cerro Matoso, SiO₂/MgO ratio is lower at Hyuga. The preheated ore from the rotary dryer is fed to the reduction rotary kiln to evaporate the remaining free moisture (23%) and chemically bonded moisture (11%) [48]. Coal is also added as the reducing agent to the rotary kiln with a feed rate of ~7 % of the ore. About 60% of the Fe³⁺ is reduced to Fe²⁺ in the rotary kiln [48]. The calcine is then fed to the electric furnace. The ferronickel and slag are tapped at around 1425 and 1575 °C, respectively [45]. Ferronickel is refined in two steps. First, sulfur is removed by adding CaC₂ to the induction furnace. According to reaction 2.37, sulfur is removed to the slag as CaS, and carbon is transferred to the molten ferronickel.



The last step is granulation by pouring the ferronickel into the water pond, in which water is jetted from the nozzles [65]. The chemical composition of the final ferronickel product is presented in Table 2.2. Hyuga produces two grades of ferronickel with high and low carbon contents. The high carbon ferronickel is fed to the argon oxygen decarburization (AOD) furnace for stainless steel production. In the case of low carbon ferronickel, the product of the desulfurization step is further processed with a converter to decrease the carbon content [19, 48].

2.5.3 PT International Nickel Indonesia (PT Inco)

PT Inco operation is located in Sorowako on the island of Sulawesi in Indonesia. The main raw ore is mined from the saprolitic layer and the lower portion of the limonitic layer [61]. West block (WB) and east block (EB) are the two deposits in Sorowako area. WB contains high concentration of olivine, generally 60-90%. This deposit has a high SiO_2/MgO (>2.2), which leads to severe damage to the sidewall integrity of the electric furnace due to the acidity of the slag and the favorable reaction between slag and basic component of the sidewall (MgCO_3). In order to control the corrosion of the sidewall caused by the high silica content of the slag and maintaining SiO_2/MgO ratio of the feed around 2 (Table 2.1), WB ore is blended with EB ore [36, 62].

The extraction process at PT Inco is similar to the matte production process explained in section 2.4.4. The process includes drying, calcination and partial reduction, smelting, converting, and refining. The typical chemical composition of the feed to the dryer is presented in Table 2.3. Compared with Cerro Matoso and Hyuga, the PT Inco feed contains lower Ni and higher Fe content.

Table 2.3 Chemical composition of the feed, calcine and matte at PT Inco [13, 45].

Sample \ Composition (wt%)	Ni	Fe	S	SiO ₂	MgO	Co
Feed	1.8	20	low	36	17	0.06
Calcine	2	23	1	40	20	0.08
Final product (converter matte)	76-80	>0.7	18-22	0	0	1

At PT Inco operations, EB and WB ores are dried separately in the dryers to reduce moisture from about 30 to 20%. EB and WB ores are mixed and fed to the rotary kiln. The coal is also added as the reductant and additional fuel. The process in the PT Inco rotary kiln is similar to those of Cerro Matoso and Hyuga, with the exception of spraying molten sulfur at the discharge end of the rotary kiln. Sulfur is added at the rate of 14 kg per tonne of the rotary kiln product (calcine). Liquid sulfur vaporizes in the rotary kiln and reacts with nickel and iron to produce iron and nickel sulfides based on reactions 2.32 and 2.33 mentioned in section 2.4.4. Nickel sulfide and iron sulfide form at the surface of the calcine particles. The calcine contains 1% sulfur after the sulfurizing process. The next step involves smelting of the calcine in the electric furnace. The unreacted carbon in the calcine (~1.3%) acts as the reductant in the electric furnace and reduces almost all of the remaining NiO to metallic nickel. The molten matte and slag are immiscible, and it is possible to tap them separately due to their density difference. Molten matte with higher density (4.5 gr/cm³) is tapped from the low taphole, while slag with lower density (3.2 gr/cm³) is tapped through the high taphole. Since electric furnace slag is separated and discarded, the nickel content of slag should be minimized to reach high recovery values in the process. The following practices are necessary to reduce the nickel content of the slag below 0.15% [13]:

- 1- Maintaining enough carbon in the calcine for reducing all NiO to Ni.
- 2- Controlling Ni content of the electric furnace matte in the low range about 26%.

3- Adjusting slag viscosity for easy separation of matte and slag and quick settling of the matte droplets

4- Preventing accidental tapping of matte with slag

The electric furnace wall is cooled by circulating cold water in the cooling system. Water cooling leads to the solidification of olivine needles on the sidewall of the refractories. The deposited olivine is also known as freeze lining that can act as a barrier layer and hinder the erosion of the refractory lining and increase its lifetime.

The last step of the Ni extraction process is converting. The matte from the smelting stage is transferred to the Peirce-Smith converters to oxidize iron by blowing air. Silica is also added as a flux to make iron silicate slag and decrease the melting point of the slag. Sulfur is partially oxidized when the iron content of the matte is decreased due to oxidation. The process is generally operated without an external heat source due to the exothermic nature of the oxidizing reactions. The slag and the matte are tapped at around 1400 °C and 1350 °C, respectively. The chemical composition of the final converter matte is presented in Table 2.3.

The summary of the specifications for various steps of the nickel extraction process at Cerro Matoso, Hyuga, and PT Inco operations is presented in Table 2.4.

Table 2.4 Summary of the specifications of the nickel laterite plants at Cerro Matoso, Hyuga, and PT Inco operations [45].

Step/Plant	Cerro Matoso (Colombia)	Hyuga (Japan)	PT Inco (Indonesia)
Drying in rotary dryer			
Size of dryer (Diameter, Length- m)	2 Rotary dryers 5.1×45	1 Rotary dryer 5×40	3 Rotary dryers #1:5×50, #2:5.5×50, #3:6×65
Nominal Capacity (Dry ore- tonnes/h)	Up to 200 each rotary dryer	160	#1-240, #2-305, #3-410
Evaporation rate (Kg H ₂ O/m ³ dryer)	64	30	47
Fuel type	Natural gas	Pulverized coal + bunker C oil for ignition + electric furnace off-gas	High sulfur fuel oil
Average fuel consumption (per tonne of dry ore)	12-18 Nm ³	12-13 L (includes oil equivalent of coal)	26 L
Calcination and partial reduction in rotary kiln			
Size of Rotary Kiln (Diameter, Length- m)	2 RKs #1:6.1×185, #2:6×135	2 RKs 4.8×105	5 RKs #1,2,3:5.5×100, #4:6×115, #5:6×135
Feed rate (Dry ore- tonnes/h)	165 each RK	60-65 each RK	#1,2,3-160, #4- 220, #5-6×235
Calcine discharge temperature (°C)	800-850	800-900	700
Fuel type	Natural gas	50-65% pulverized coal & bunker C oil	High sulfur fuel oil

Average fuel consumption (per tonne of dry ore)	50-55 Nm ³ (~40-44 kg)	60-62 L (~78-81 kg)	66 kg
Reductant type	Anthracite coal	Coal	Bituminous coal
Average reductant consumption (kg per tonne of dry ore)	50-60	70-80	35-40
Smelting in the electric furnace			
Electric furnace dimensions (D×h - m)	2 Round furnaces 22.15×7.6	2 Round furnaces #1:18.5×5.5, #2:17.5×5.4	4 Round furnaces 18×6
Average power per furnace (MW)	65-70	60 day, 80 night	55-60
Average electrical energy consumption (kWH/t of calcine)	520	470-480	465
Matte/Metal temperature (°C)	1450-1470	1400-1450	1350-1400
Slag temperature (°C)	1560	1550-1600	1500-1550
Refining (ferronickel) or converting (matte)			
Process	Refining (3 steps)	Refining (3 steps)	Converting
Procedure explanation	<p>Step 1: De-P & De-C in COBS and ASEA ladles using CaO, SiO₂ and O₂ reagents at 1440 °C</p> <p>Step 2: Deoxidation in COBS and ASEA</p>	<p>Step 1: Desulfurization in low frequency induction furnace by adding CaC₂, working in 1400- 1450 °C</p> <p>Step 2: De-C & De-Si in LD convertor by flowing</p>	<p>3 Peirce Smith Converters at 1400 °C with average air rate of 18000 Nm³/h.</p>

	ladles using FeSi and Al reagents at 1550 °C Step 3: Desulfurization in COBS and ASEA ladles using CaO and Al reagents at 1620 °C	oxygen at 1600-1650 °C	
Final product	Ferronickel (3-5mm shots)	Ferronickel (99% shots and 1% ingots)	Granulated Bessemer matte
Annual tonnage production in the period of 2002-4 (tonne/year)	49100	22000	72000

2.6 Calcination of Nickel Laterites

As described in section 2.4.3.2, calcination is an essential step for ferronickel production via RK-EF process. In this section, the reactions and phase transformations that occur during the calcination process are discussed in detail.

Keskinkilic et al. investigated the calcination characteristics of Sivrihisar laterite ore from the Central Anatolia region of Turkey [66]. The authors classified the ore as limonite due to high iron content (32.6 %) and low magnesium content (1.03 %). The percentage of weight loss versus time at various temperatures is shown in Figure 2.8. By increasing the temperature, the weight loss is increased, and the samples reach the steady state in a shorter period of time. For instance, by

comparing the samples calcined at 250 and 800 °C, the one carried out at 250 °C showed 5.9% weight loss and reached the steady state at 65 min, while by increasing the calcination temperature to 800 °C, weight loss and steady state time are 10% and 27 min, respectively. The authors attributed the weight loss to the removal of chemically bound water and volatiles. Moreover, the effective temperature for removing volatiles and crystalline water was found to be 700-800 °C.

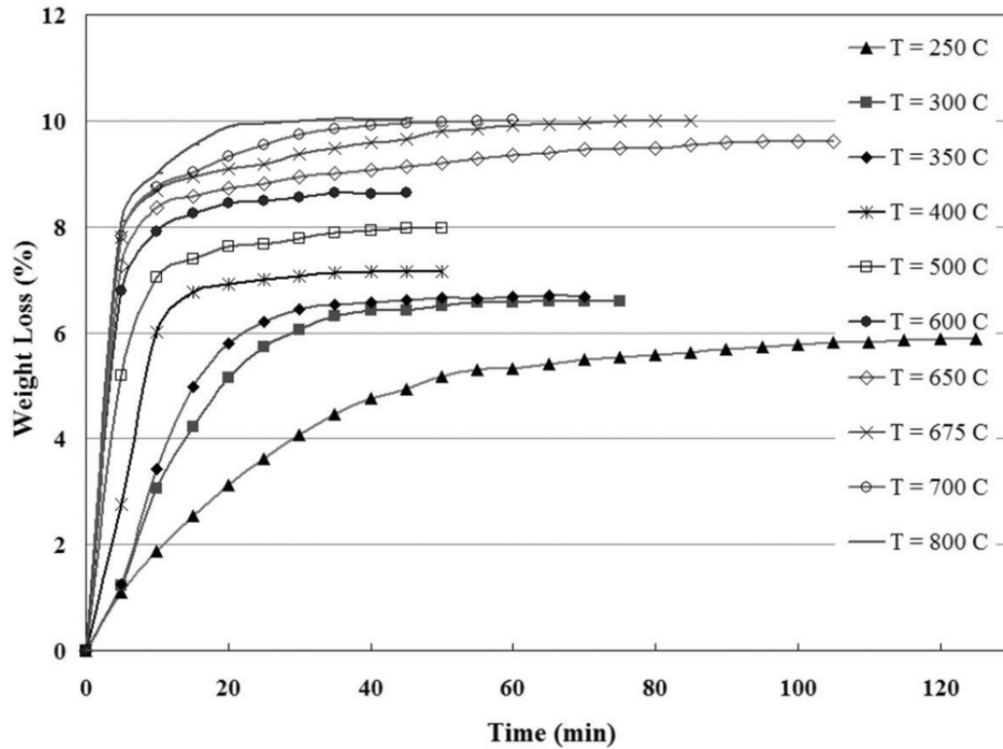


Figure 2.8 The weight loss percentage versus time at various temperatures for Sivrihisar limonite ore [66].

Zevgolis et al. studied phase transformation of three types of Greek laterites, categorized as limonite and smectite, by heating them from room temperature to 900 °C [67]. Heating of limonite and smectite to 400 °C results in dehydroxylation of goethite ($\text{FeO}(\text{OH})$) and transformation of goethite to hematite. Heating at 850 °C leads to decomposition of chlorite ($(\text{Mg}, \text{Ni}, \text{Fe}, \text{Al})_6 (\text{Al}, \text{Si})_4 \text{O}_{10} (\text{OH})_8$) and serpentite ($(\text{Mg}, \text{Fe}, \text{Ni})_6 \text{Si}_4 \text{O}_{12} (\text{OH})_6$) in limonite and smectite ores, respectively.

Huang and Lv investigated the phase transformations that take place in saprolite ore using TGA [49]. They found a total mass loss of 17.3%, which corresponds to evaporation of free water with 8.9% mass loss at 100-140 °C, goethite decomposition with 4.3% mass loss at 200-480 °C, and hydroxyl group removal with 4.1% mass loss at 500-800 °C. Other similar investigations have been conducted to understand the phase changes during the calcination process [16, 17, 68–71]. These studies also confirmed goethite decomposition and dehydroxylation as the main phenomena in the calcination stage.

2.7 Reduction of Nickel Laterites

Reduction of nickel laterite ores is categorized into direct and indirect reduction reactions. Carbon and carbon monoxide are the main reducing agents for direct and indirect reduction reactions, respectively. The first step of the direct reduction is the reaction of carbon with nickel and iron oxides. The reduction process is continued by gaseous reductants, i.e. CO, emitted through the solid-state reduction reactions. Carbon monoxide produced by Boudouard reaction plays a significant role in maintaining the reducing atmosphere [72]. Indirect reduction by CO gas is more significant than direct reduction via carbon due to faster kinetics of gas-solid reactions versus solid-state reactions. The effects of temperature, the reducing atmosphere, gas flow rate, and time on the reduction behavior of nickel laterite are discussed in the following sections.

2.7.1 The Effect of the Temperature

Temperature is a crucial factor that influences the reduction behavior of nickel laterite ores. The effect of temperature on the reduction behavior of laterite ores has been investigated in several studies. Bunjaku et al. studied the reduction behavior of three saprolite ores in 72 vol% CO-28 vol% CO₂ gas mixture at 750 and 900 °C [73]. The degree of reduction was defined by the ratio

of the mass loss after reduction to the oxygen content in iron and nickel oxides of the original ore. As shown in Figure 2.9, the reduction reaction was rapid in the early stages of the process and slowed down considerably after the first 5 minutes. The authors mentioned recrystallization of magnesia silicate compounds at 800-820 °C affects the degree of reduction [74, 75]. The nickel oxide incorporated in forsterite structure will be locked up in temperatures above 800 °C [76]. Thus, samples processed at 900 °C showed a lower degree of reduction than the ones at 750 °C. The authors proposed that the diffusion through the product layer controlled the reaction rate [73].

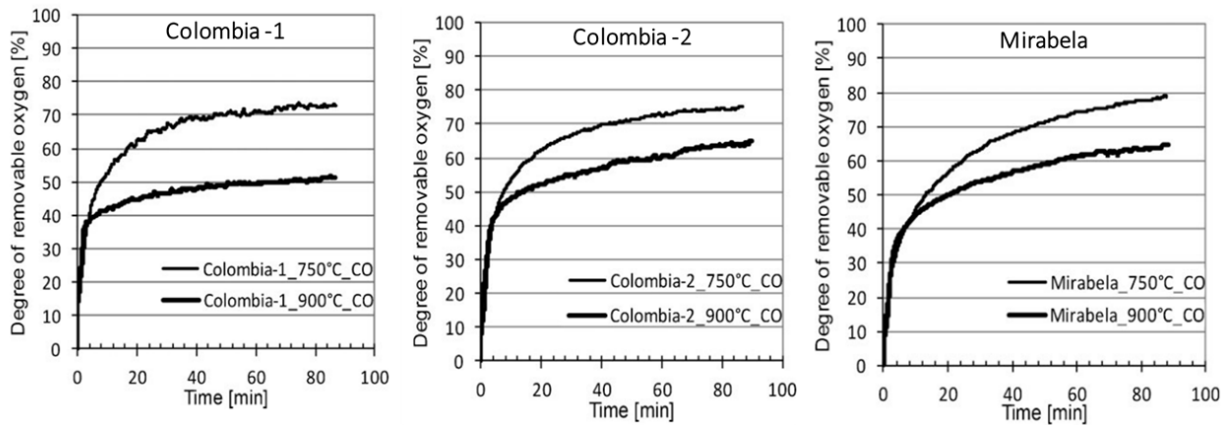


Figure 2.9 The effect of temperature on the reduction of three saprolite ores in CO/CO₂=2.57 gas mixture [73].

The reduction behavior of saprolite ore by 50 vol% CO-50 vol% CO₂ gas mixture at 700-930 °C was examined by Li [75]. The maximum extent of reduction was obtained below the temperature of olivine recrystallization. It is worth mentioning that forsterite (Mg₂SiO₄), and enstatite (MgSiO₃) can be formed by lizardite (Mg₃Si₂O₅(OH)₄) dissociation during nickel laterite calcination process. Formation of crystalline magnesia silicate phases at high temperature depends on MO to SiO₂ ratio in the raw ore, where MO is the divalent metal oxides in the ore. MO/SiO₂ of higher than 1.5 implies the formation of forsterite [77]. The reducibility of nickel oxide in enstatite

structure is easier than forsterite because of the porous structure of enstatite that facilitates the gas-solid reaction [73, 76, 78, 79]. Therefore, it is concluded that the composition of the raw ore significantly affects the reducibility of nickel oxide. In other words, formation of forsterite at high temperatures can hinder the reduction of nickel oxide, while enstatite formation would not affect the reduction of nickel oxide significantly.

2.7.2 The Effect of the Reducing Atmosphere

Purwanto et al. investigated the reduction of low-grade limonite ore in CO-CO₂ atmospheres containing 30% and 90% CO at 1000 °C [80]. According to their results, 2% and 21% mass loss were observed for the samples reduced in the atmosphere containing 30% and 90% CO, respectively. Higher mass loss observed at higher CO content implies an increased reduction percentage in the CO rich atmosphere. The effect of the CO/CO₂ on the reduction of a saprolitic ore was also examined by Li [75]. As can be seen in Figure 2.10, by increasing the CO/CO₂, weight loss and the degree of reduction were increased.

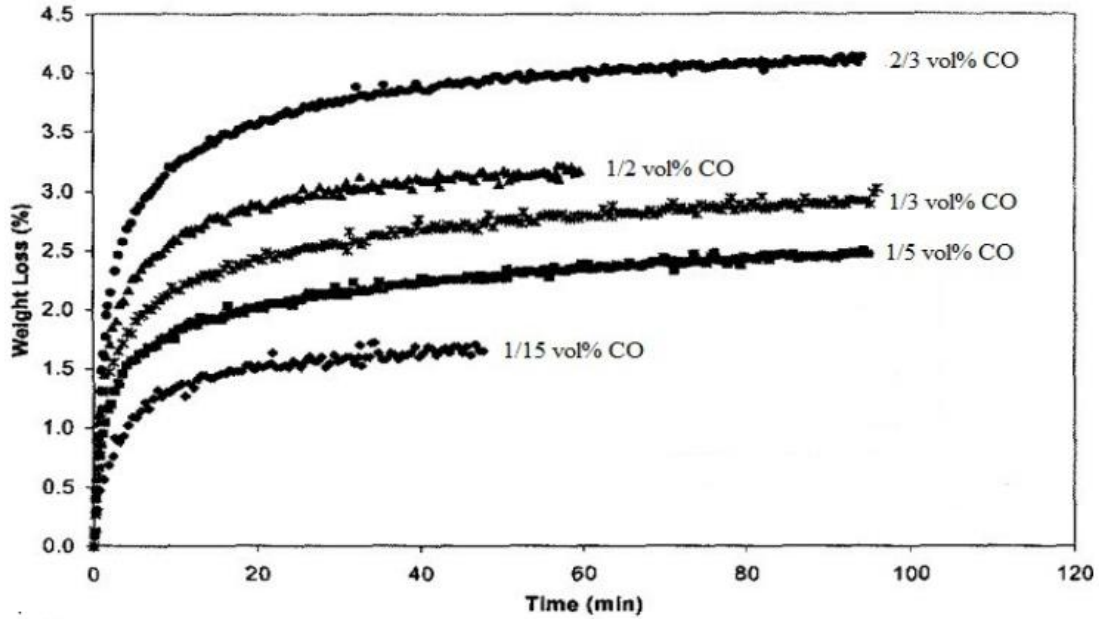


Figure 2.10 The effect of the CO/CO₂ on the reduction of saprolite ore at 740 °C [75].

2.7.3 The Effect of the Gas Flow Rate

Limited studies have been done on the effect of the gas flow rate on the reduction of laterite ores. Li examined the reduction of a saprolite ore at 1000 °C and CO to CO₂ ratio of 3 using different gas flow rates [75]. According to Figure 2.11, increasing the gas flow rate from 200 to 2200 ml/min leads to a higher degree of reduction. However, the author pointed out that the effect of gas flow rate in the range of 1500-3000 ml/min was negligible since, at high flow rates, the external mass transfer of the gas phase was not the controlling mechanism for the reduction reactions. The gas flow rate of 2200 ml/min was selected for experiments since it is sufficiently large to eliminate the mass transfer control effect.

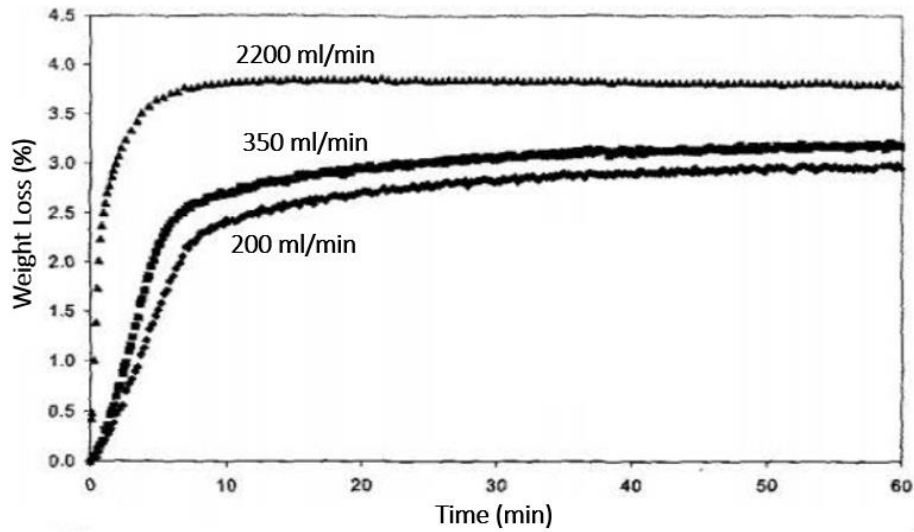


Figure 2.11 The effect of the gas flow rate on the reduction of a saprolite ore at 1000 °C and $\text{CO}/\text{CO}_2=3$ [75].

2.7.4 The Effect of the Processing Time

Gas-solid reactions are the main reactions that occur during the reduction of nickel laterites in the rotary kiln. The reduction time is expected to influence the three main steps of these reactions, namely mass transfer of gases, diffusion through the solid, and interfacial chemical reaction [79, 81, 82]. According to the findings of the study by Li (Figure 2.11) reduction rate is rapid at the first 10 minutes and then declined. The author proposed that the decrease in the overall reduction rate is related to particle agglomeration, which results in a decrease in the surface area as well as the phase changes that hinder gas-solid reactions.

2.8 Kinetics of Nickel Laterite Reduction

Thermal gravimetric analysis-differential scanning calorimetry (TGA-DSC) is one of the common methods for studying the kinetics of the reduction reactions. Generally, the kinetic data is obtained by measuring the weight change of the sample during the thermal process. The general expression for the rate of reaction is [83, 84]:

$$\frac{d\alpha}{dt} = f(\alpha)k(T)h(P) \quad (2.38)$$

Where $f(\alpha)$, $k(T)$, and $h(P)$ are the functions of the extent of reaction, temperature, and pressure.

The extent of the reaction is defined as below:

$$\alpha = \frac{W_i - W}{W_i - W_f} \quad (2.39)$$

Where W is the weight of the sample at time t , and W_i and W_f are the initial and final weight of the sample, respectively. The temperature function is modeled using the Arrhenius equation:

$$k(T) = A \exp\left(\frac{-E}{RT}\right) \quad (2.40)$$

E is the activation energy (J/mol), A is the pre-exponential factor (1/s), and R is the gas constant (J/(mol.k)). The kinetic parameters (E and A) and the reaction model for the main reactions that took place during the process can be obtained by two different approaches, i.e., model-fitting and model-free methods.

Several works have been performed on the kinetics of nickel laterite reduction using carbon, carbon monoxide, hydrogen, and methane [85–91]. Since carbon and carbon monoxide are the reducing agents of interest in this thesis, the works related to the carbothermic reduction of nickel laterite are summarized here.

Two main approaches for kinetic analysis are model-fitting and model-free. The derivation of kinetic parameters associated with a specific kinetic model is known as model-fitting approach [83, 92, 93]. In this methodology, several kinetic models are fitted to data, and the best model is selected based on the highest coefficient of determination. However, just a single kinetic model is selected for the overall process. In order to identify the possible steps of the reaction by calculating

E values versus extent of reaction, model-free approach is utilized [83 ,84, 92, 94]. The E values in the whole process are obtained by model-free approach without imposing a hypothetical function as the kinetic model. The detailed description of these kinetic approaches are discussed in chapter 5.

Li et al. investigated the kinetics of low-grade nickel laterite reduction in carbon monoxide using both isothermal and non-isothermal tests [95]. The authors divided the process into three stages based on the results of the differential thermal gravimetric (DTG) graph of the non-isothermal TGA test (Figure 2.12 (a)). According to XRD results of the samples collected at different temperatures, the first stage is attributed to the reduction of NiO and Fe₂O₃ to Ni and Fe₃O₄ at 460-570 °C. The next step consists of the reduction of Fe₃O₄ to FeO and partial reduction of FeO to Fe at 570-820 °C. In the last stage, reduction reaction of FeO to Fe is continued at 820-1000 °C. The authors utilized both model-free and model-fitting approaches for kinetic analysis. The variation of the activation energy versus the extent of reaction at 450-1000 °C is shown in Figure 2.12 (b). They found that the combination of chemical reaction and gas diffusion is the rate-controlling mechanism below 600 °C. In contrast, by increasing temperature, the reduction reactions occur easier, and the process is controlled by diffusion of CO within the gas phase and through the pores of the laterite ore.

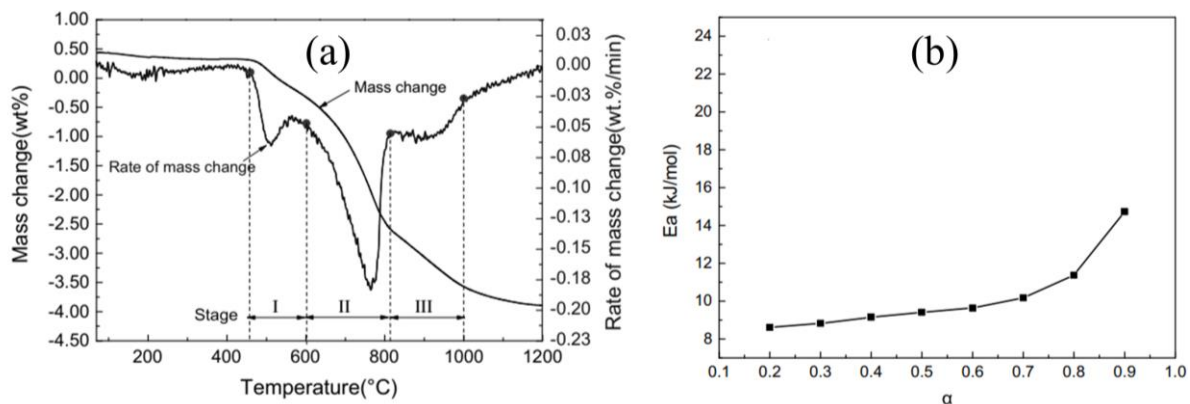


Figure 2.12 (a) Non-isothermal TGA analysis of a nickel laterite ore, (b) Variation of the activation energy versus the extent of reaction at 450-1000 °C [95].

Kinetic analysis of nickel laterite reduction in carbon monoxide was also examined by Li et al. [96]. Non-isothermal TGA tests were carried out at various heating rates in the range of 5-20 °C/min. It was found that the reduction of the laterite ore is a complex process, including several steps. They concluded that the first stage relates to the reduction of trevorite (NiFe_2O_4) to Ni and Fe_3O_4 at 200-600 °C, and the second stage corresponds to the reduction of Fe_3O_4 to FeO or Fe at 600-800 °C. The reduction rate is gradually decreased at the last stage at 800-950 °C [96]. The authors calculated kinetic parameters and selected kinetic models for three stages of the process based on the maximum correlation coefficient using model-fitting method.

Lv et al. studied non-isothermal reduction kinetics of a nickel laterite ore with graphite in an inert atmosphere [97]. The results indicated that the reduction process could be divided into three stages. In the first stage, Fe_2O_3 is reduced to Fe_3O_4 . The high value of activation energy (~480 kJ/mol) was obtained in the first stage, due to the slow kinetics of solid-solid reactions and the difficulty of graphite diffusion in the laterite ore. In the second stage, the reduction of Fe_2O_3 and FeO occurred, and the concentration of CO is increased, which makes the reduction process easier and leads to the lower activation energy of ~280 kJ/mol. In the last step, fayalite (Fe_2SiO_4) is reduced.

Since reduction of Fe_2SiO_4 is more difficult than FeO , the activation energy of the third stage was higher than the second stage, i.e., ~ 310 kJ/mol compared with ~ 280 kJ/mol. Similar results were observed by Liu et al., who examined the kinetics of carbothermic reduction of nickel laterite [98]. The authors mentioned that the first and second stages of the reduction process are controlled by three-dimensional diffusion function, while the last stage is controlled by the chemical reaction mechanism.

2.9 The Behavior of Laterite Ores in Carbo-Sulfurizing Gas Mixture

Sulfurization reactions of nickel laterite ores are gas-solid reactions as a result of the interaction of solid laterite particles with the moving gas stream. The following phenomena may occur during gas-solid reactions [81, 99]:

- 1- External mass transfer of the gas phase from the bulk of the gas stream to the surface of solid particles
- 2- Diffusion of the gases through the solid
- 3- The chemical reaction of the gas with the solid at the surface of the particles

The rate-controlling step of the overall reaction can be the chemical reaction, the diffusion, or the combined effects of the above two mechanisms [99]. The slowest step of the reaction is expressed as the rate-controlling step. If the gas-solid system includes fast reactions, the overall rate is controlled by diffusion of the gas through the solid surface. If the resistance to mass transfer is negligible, the overall reaction rate is controlled by the chemical reaction. When mass transfer and chemical reaction reveal comparable resistance to the progress of the reaction, both mechanisms should be considered simultaneously [99].

Limited studies have been conducted on nickel laterite calcination in the reducing atmosphere containing SO_2 gas. The most relevant works were performed on the sulfurization of bauxite ore in a CO-SO_2 gas mixtures. These studies were carried out to increase the aluminium content of bauxite ore by removing iron via sulfurization and subsequent chlorination process. These studies are the most relevant works to this thesis. Although bauxites and laterites have different chemical compositions, they both contain significant amount of iron oxides that are prone to sulfurization. Hence, it is reasonable to expect similarities between the behavior of bauxites and laterites in reducing atmospheres containing SO_2 .

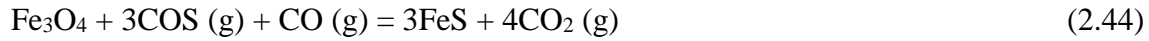
Sulfurization is one of the useful methods to selectively remove iron from bauxite ore. Fink and Marchi examined the conversion of Fe_2O_3 to FeS by adding elemental sulfur at high temperatures followed by a chlorination process to remove 90% of iron oxide from the ore [100]. Holliday and Milne demonstrated the feasibility of iron oxide removal from bauxite ore using CO-SO_2 gas mixtures [101]. According to their thermodynamic calculations, FeS was found to be the main sulfide phase resulted from the reaction between CO-SO_2 gas mixture and hematite [102]. Holliday and Milne carried out sulfurization reactions within 15 min at $700\text{ }^\circ\text{C}$ using $\text{SO}_2/\text{CO}=0.54$ to decrease iron level from 5.3% to 0.1-0.3% [101]. Bolsaitis and Nagata investigated the kinetics of hematite sulfurization in $\text{SO}_2\text{-CO}$ gas mixture using thermogravimetric analysis (TGA) [103]. They used a wide range of SO_2 mole fraction, X_{SO_2} , from 0.4 to 0.92 at $500\text{-}900\text{ }^\circ\text{C}$. Sample size and gas flow rate were fixed at 0.2 g and 1130 ml/min, respectively. It was found that Fe_2O_3 is converted to FeS by reduction and sulfurization reactions. Furthermore, the main sulfurizing agents in CO-SO_2 atmosphere were identified as S_2 and COS gases. The main chemical reactions in the system are summarized as below:

a) Gaseous phase reactions:



b) Reduction of hematite to magnetite as given by reaction 2.20.

c) Sulfurization of magnetite by COS and S₂



The equilibrium partial pressures of the components in CO-SO₂ atmosphere at 700°C are presented in Figure 2.13. The main sulfurizing agents are S₂ and COS. S₂ is the prevalent sulfurizing reagent in X_{CO} < 0.4, while by increasing X_{CO}, COS becomes the dominant reagent at X_{CO} > 0.7.

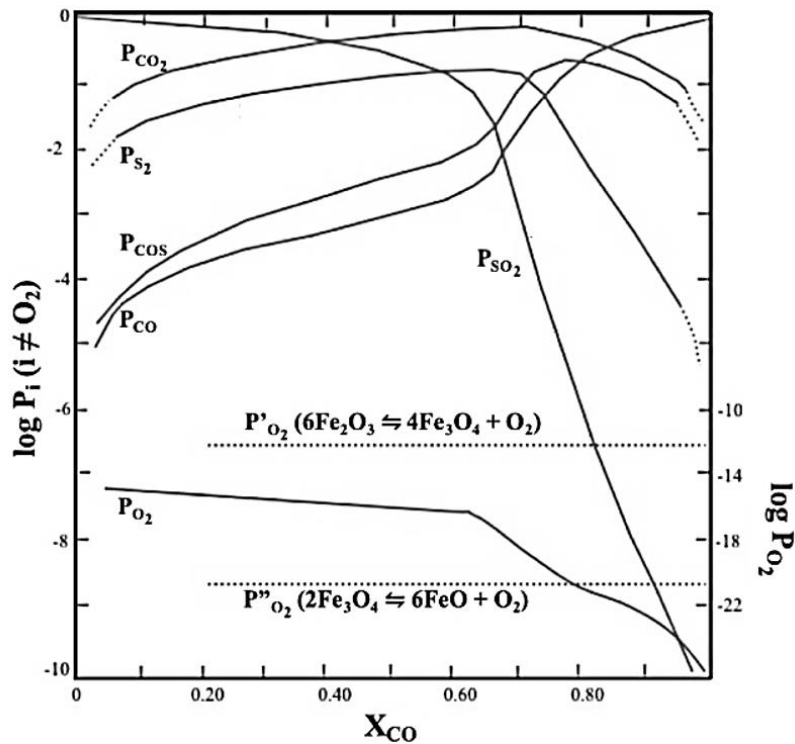


Figure 2.13 Equilibrium partial pressure of the gaseous components in CO-SO₂ system at 700 °C [103].

The same authors carried out TGA experiments to study the effect of the gas composition on the sulfurization behavior of the ore by analyzing the mass change in various X_{CO} . The weight loss in the TGA curves corresponds to the reduction of hematite to magnetite, and weight gain pertains to the sulfurization reactions and conversion of Fe_3O_4 to FeS . The lowest overall conversion for the reduction and sulfurization reactions can be observed at $X_{CO}=0.4$, which is the lowest CO content. The effect of the temperature on carbo-sulfurization of Fe_2O_3 is shown in Figure 2.14. Increased rate of reduction reactions followed by sulfurization reactions were observed at temperatures above 600 °C. The rate of the carbo-sulfurization reactions is significantly lower at 550 °C compare to higher temperatures. By decreasing the temperature to 500 °C, the rate of the sulfurization reactions is decreased significantly, and the rate of the weight-gaining period is considerably diminished. The authors observed that FeS nuclei formed after about 5 min of the process, and the nuclei started to grow over time. So, the nucleation and growth mechanism was suggested as the primary mechanism of sulfide formation. Furthermore, it was concluded that the overall carbo-sulfurizing process is controlled by diffusion of S_2 and COS gases through the solids.

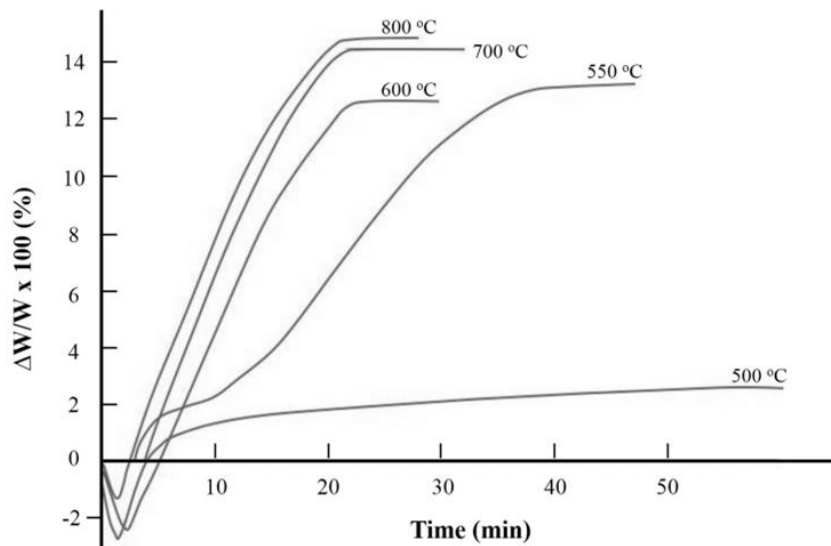


Figure 2.14 The effect of the temperature on TGA curves at $X_{co}=0.66$ [103].

A similar study was carried out to sulfurize the hematite present in the laterite ore, and the results were compared to that of pure hematite sulfurization [104]. Laterite ore containing 25.9% Al_2O_3 , 38.5% Fe_2O_3 , 31.3% SiO_2 , and 4.6% TiO_2 was used as the raw material for the sulfurization process. TGA curves of laterite sulfurization in various compositions of CO-SO₂ atmosphere at 700 °C are plotted in Figure 2.15. The percentage of mass gain is maximized at $X_{\text{CO}}=0.66$.

A lower degree of reduction was observed for the laterite sample compared to pure hematite, while the required time for sulfide nucleation was similar in both cases. The authors attributed the low degree of reduction in the laterite sample to the presence of impurities in the hematite grains of laterites. It was found that once the sulfide phase is nucleated, the rate of sulfurization for laterite ore is about two times higher than pure hematite, probably due to the higher specific surface area of the laterite sample [104].

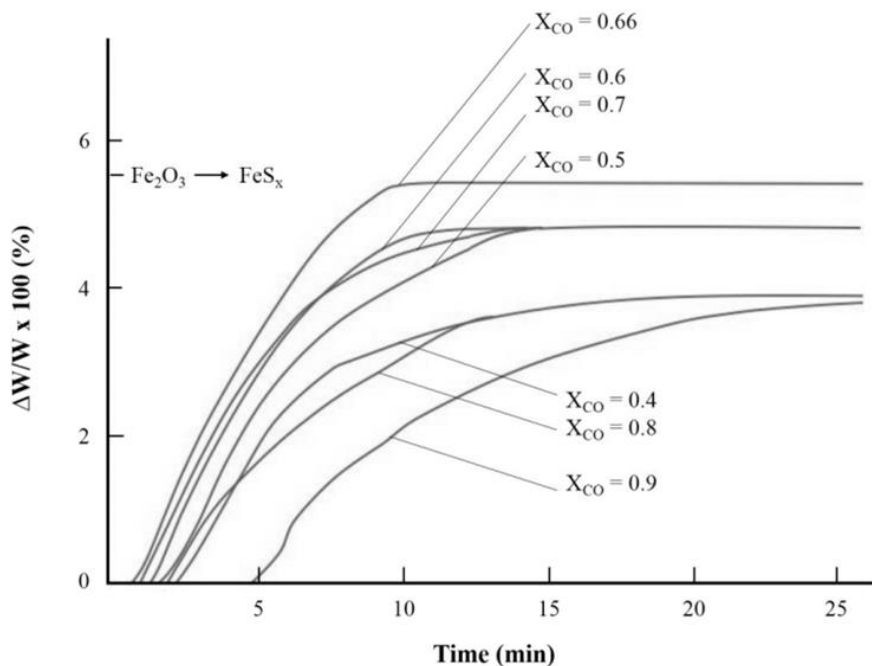


Figure 2.15 TGA plots of carbo-sulfurization of the laterite sample at 700 °C in various compositions of CO-SO₂ gas mixture [104].

It should be emphasized that the gas compositions used in all previous studies are considerably different from the ones in the current investigation. The atmosphere used to promote sulfurization of iron oxides is not the same as the atmosphere generated from fuel combustion during nickel laterite calcination. Particularly, the partial pressure of SO_2 in the rotary kiln is significantly lower than the aforementioned studies.

To identify the potential compounds that may form during the sulfurization reaction, predominance diagrams of Fe-O-S and Ni-O-S systems at 800 °C are plotted in Figure 2.16. The above predominance diagrams provide an understanding of the behavior of sulfur in nickel laterite calcination. The dominant phases of Fe-O-S and Ni-O-S systems at different values of P_{SO_2} and P_{O_2} are predicted based on Figure 2.16. By increasing P_{SO_2} , the dominant phase is shifted from metal/oxide to sulfide/sulfate phases, while increasing P_{O_2} results in oxide formation. It should be noted that the system containing CO, CO_2 and other compounds of the ore are not considered in the predominance diagrams. In this study, the overall behavior of the system is predicted by equilibrium chemical composition of the solids and gases, which is discussed comprehensively in section 6.2.

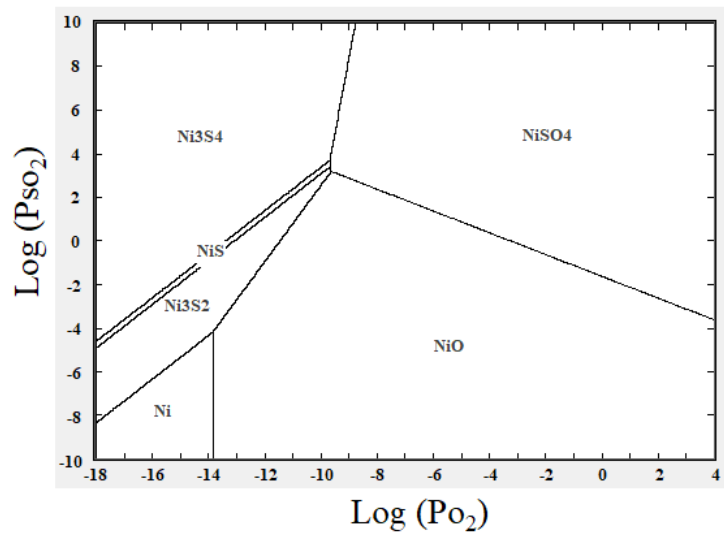
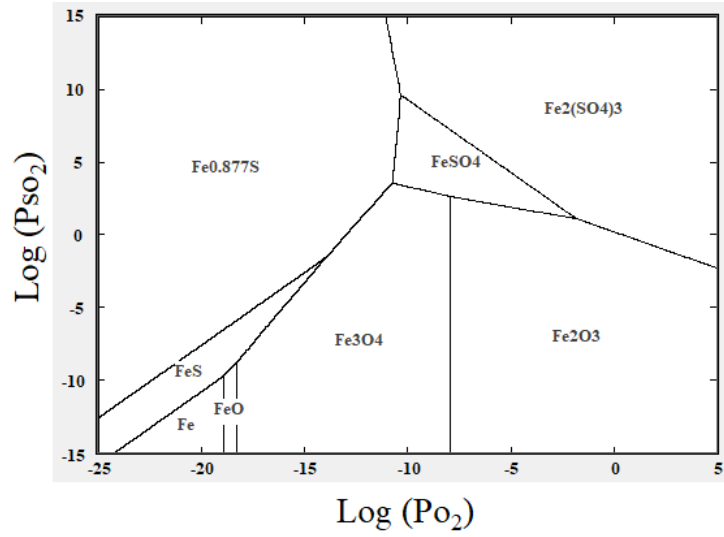


Figure 2.16 Predominance diagrams of (a) Fe-O-S and (b) Ni-O-S at 800 °C obtained by HSC Chemistry 5.11 [105].

Chapter 3: Research Gaps and Objectives

3.1 Research Gaps

Sulfur is one of the most harmful impurities in ferronickel because of its detrimental effects on the mechanical properties of nickel alloys. Therefore, it is crucial to monitor sulfur behavior during the RK-EF process. Very limited studies have been performed on the sulfur behavior during calcination and partial reduction of the oxide ores. The most pertinent work is iron removal from bauxite ore by the sulfurization process [103]. The kinetics of Fe_2O_3 sulfurization in CO-SO_2 gas mixtures was investigated by TGA analysis. Another similar study was carried out to remove iron oxide from laterite by sulfurization and chlorination [104]. However, the partial pressure of SO_2 in the aforementioned studies was much higher than the one generated by fuel (e.g., coal) combustion in a rotary kiln.

Raw laterite ores typically have a negligible sulfur content. Therefore, the sulfur in the crude ferronickel is believed to be originated from fuel and reductant added in the rotary kiln. Coal is utilized as a common fuel for calcination of nickel laterites in rotary kiln. Due to the depletion of high-quality coal with low impurity content, high-sulfur coal has been used as fuel for nickel laterite calcination. During coal combustion, sulfur is oxidized to SO_2 gas. It is hypothesized that SO_2 generated from coal combustion reacts with the ore and causes the sulfur transfer to the calcine. Hence, it is essential to monitor the behavior of sulfur in the rotary kiln to control the sulfur content of the calcine. Aside from the recent work in our group [106], there is no available literature on sulfur deportment in nickel laterites calcination. The main research gaps in the literature are described below:

The behavior of sulfur during the calcination process

In order to understand the behavior of sulfur, it is crucial to identify the main sulfurization reactions and the sulfur-containing compound in the calcine. To control the sulfur content of the calcine, it is essential to investigate the effect of the process parameters such as sulfur content of the fuel, reducing atmosphere, gas flow rate, and temperature.

In addition, the kinetics of the sulfur deportment in the laterite calcination has not been investigated before. A comprehensive kinetic analysis on the sulfurization of nickel laterite ores will provide a fundamental understanding of the sulfurization reaction rate.

Decreasing the sulfur content of the calcine by inhibiting the absorption of sulfur from fuel to the calcine in a rotary kiln

Taking into account that the behavior of sulfur during nickel laterite calcination has not been examined before, it is expected to see a gap in proposing solutions for controlling the sulfur content of the calcine. Proposing an effective way for decreasing the transfer of sulfur originated from rotary kiln fuel to the calcine will diminish the load of the refining step and decrease the overall cost of the extraction process.

3.2 Research Objectives

The long-term objective of this research is to minimize the percentage of sulfur in the nickel laterite calcine and subsequently the ferronickel. The current work investigates the effect of sulfur originated from rotary kiln fuel on the composition of the calcine. In order to address the research gaps outlined above, the overall goal of the project is broken down into four specific objectives:

Objective 1: Ore characterization and investigating its calcination behavior:

Sub-Objective (1-a): Identifying the main reactions during the calcination stage;

Sub-Objective (1-b): Kinetic analysis of the calcination reactions identified in sub-objective (1-a).

Objective 2: Identifying the sulfurization reactions and the effect of the operational parameters on the composition of the kiln calcine:

Sub-Objective (2-a): Identifying the sulfurization reactions and the main sulfur-containing compound in the calcine;

Sub-Objective (2-b): Examining the effect of the sulfur content of the coal, reducing atmosphere, gas flow rate, and temperature on the composition of the calcine by thermodynamic analysis and high-temperature experiments.

Objective 3: Kinetic analysis of the sulfurization process:

Sub-Objective (3-a): Calculating the kinetic parameters and identifying the kinetic model for sulfur deportation during the calcination stage.

Sub-Objective (3-b): Investigating the effect of P_{SO_2} on the kinetics of the sulfurization reactions.

Objective 4: Inhibition of sulfur transfer from the fuel to the calcine:

Sub-Objective (4-a): Identifying the main reactions corresponding to sulfur reduction;

Sub-Objective (4-b): Examining the effect of time and temperature on the sulfur reduction in the calcine.

Chapter 4: Materials and Methods

4.1 Materials

The laterite ore used as a raw material in this study was originally obtained from a Brazilian deposit and was provided by FLSmidth. Graphite with 99.99% purity was purchased from Thermo Fisher Scientific and used as a reducing agent in the high-temperature experiments carried out in the horizontal tube furnace. The reagents used in the digestion of the calcine are: nitric acid (HNO₃) with 69.7% purity and potassium hydroxide (KOH) with 89% purity from VWR chemicals. Bituminous coal was used as a reducing agent in TGA/DSC experiments. The proximate analysis of the bituminous coal was carried out based on ASTM standards (D3173, D3174, and D3175). The results are summarized in Table 4.1. The sulfur content of the coal is 2.13%. This value is determined by LECO analysis.

Calcium carbonate, CaCO₃, from Fisher Scientific with >99% purity, was used as an additive in the experiments of the last chapter of the thesis.

Table 4.1 Proximate analysis of bituminous coal (wt%).

Coal	Volatile matter	Ash	Moisture	Fixed carbon
Bituminous	31.14	13.64	2.33	52.89

4.2 Characterization of the Raw Materials

The chemical composition of the raw ore was determined by X-ray fluorescence (XRF) analysis at Bureau Veritas Minerals (BVM-Vancouver). The results are shown in Table 4.2. The ore contains various oxides, including SiO₂, Fe₂O₃, MgO, Al₂O₃, and NiO.

Table 4.2 Chemical composition of the laterite ore analyzed by XRF.

Component	Weight Percent
SiO ₂	36.7
Fe ₂ O ₃	34.6
MgO	8.74
Al ₂ O ₃	5.88
NiO	2.38
Cr ₂ O ₃	1.62
MnO	0.58
Na ₂ O	0.12
TiO ₂	0.1
CaO	0.03
Co	0.12
S	0.02
LOI	9.11

The phase composition of the raw ore was determined by X-ray diffraction (XRD). According to the XRD results presented in Figure 4.1, the main crystalline phases of the raw ore are identified as lizardite ((Mg₃Si₂O₅(OH)₄), nontronite (Na_{0.3}Fe₂(Si,Al)₄O₁₀(OH)₂.n(H₂O)), trevorite (NiFe₂O₄), hematite (Fe₂O₃), magnetite (Fe₃O₄), wustite (FeO), goethite ((FeO(OH)), and silicon oxide (SiO₂). The ore is identified as a mixture of saprolite and smectite due to the presence of both lizardite and nontronite.

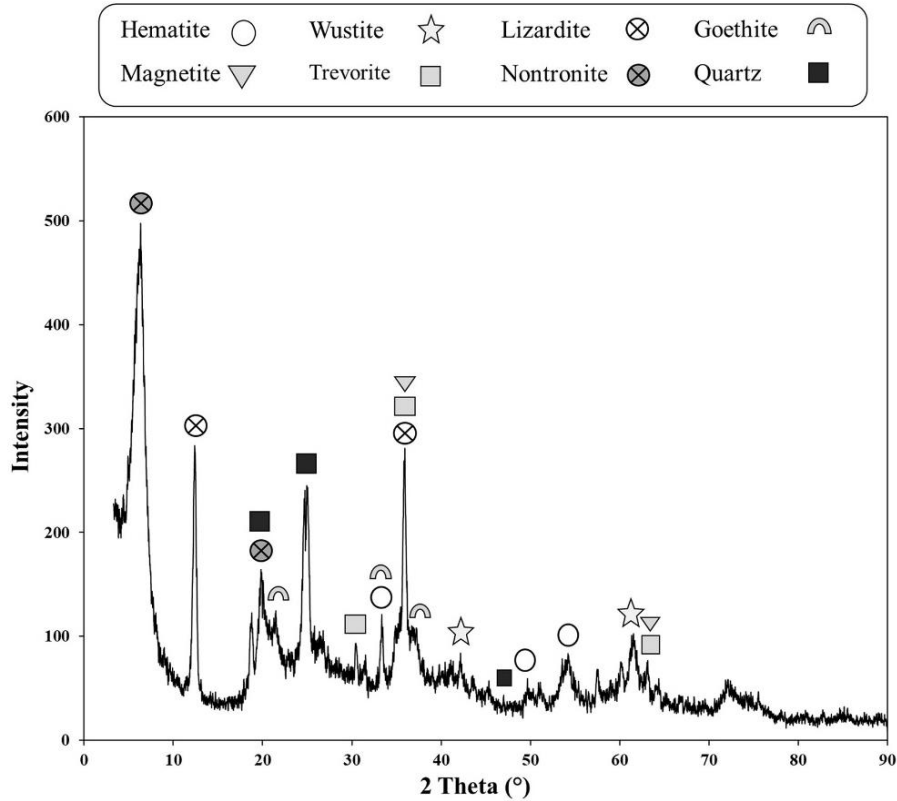


Figure 4.1 XRD pattern of the raw laterite ore.

4.3 Preliminary Processing of the Raw Materials

The raw laterite ore was dried in the oven at 130 °C for 2 h to remove the free water. Based on the mass loss observed after the drying process, the free water of the laterite ore is calculated as 28%. In the next step, the dried ore was ground in a Fritsch Pulverisette Mortar Grinder Mill for 5 min. The images of the oven and grinder are shown in Figure 4.2. The particle size distribution of the ore was obtained by dry-sieving 200 g of the ore through a sieve stack with various screen openings of 710, 600, 500, 425, 355, 300, 212, and 120 μm . Figure 4.3 demonstrates the particle size distribution of the ground ore. As can be seen in Figure 4.3, 80% of the ground ore was smaller than 355 μm , $P_{80} = 355 \mu\text{m}$.



Figure 4.2 (a) Oven, (b) mortar grinder mill.

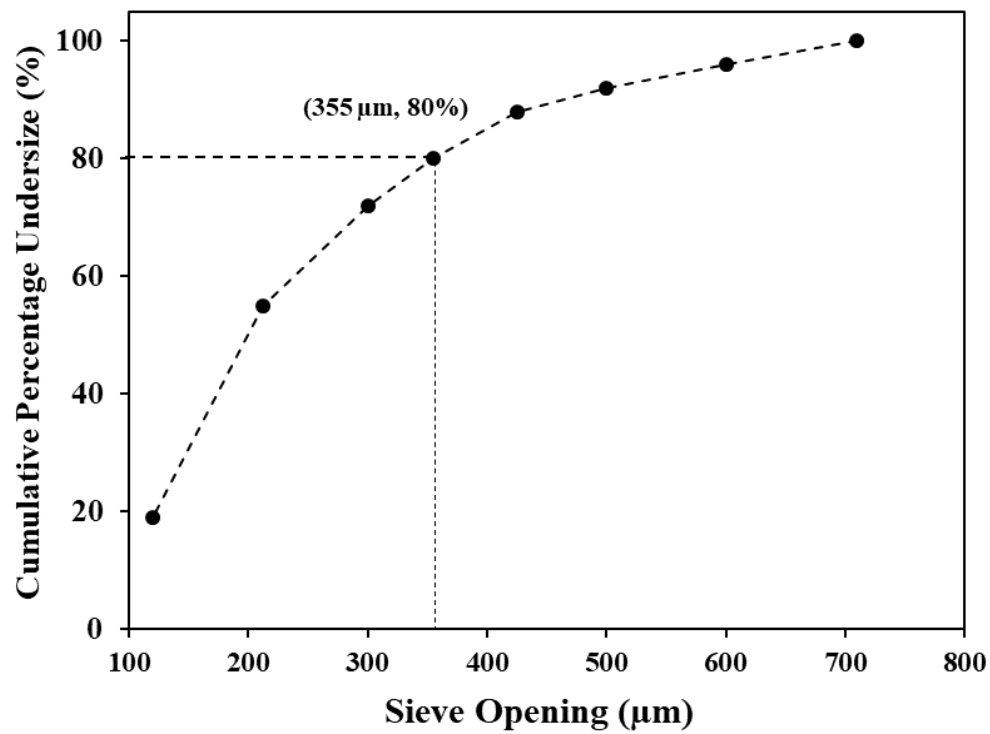


Figure 4.3 Particle size distribution of the ground ore.

4.4 Calcination and Partial Reduction Experiments

4.4.1 TGA-DSC Experiments

Thermal gravimetric analysis-differential scanning calorimetry (TGA-DSC) experiments were performed by Perkin-Elmer STA 600. During the calcination process, the mass loss, temperature, and heat flow were simultaneously measured and recorded. TGA-DSC test was employed to determine the reactions and phase transformations that occur during calcination of the laterite ore. Various samples were collected from intermediate temperatures and analyzed using XRD. Kinetics of the calcination reactions were investigated using TGA-DSC results. For this purpose, activation energy corresponding to the extent of the reaction for the whole process is calculated by model-free approach. By combining model-free and model-fitting methods, the kinetic parameters and kinetic models are obtained for the main reactions that take place during the calcination process. The details of the kinetic analysis are presented in chapter 5.

Dried ore was mixed with 5 wt% bituminous coal as the reducing agent. Subsequently, the samples were ground to <53 μm . Samples were heated from 30 to 990 $^{\circ}\text{C}$ at five heating rates of 10, 20, 30, 40, and 50 $^{\circ}\text{C}/\text{min}$ while flowing 20 ml/min of nitrogen. These experiments were performed to identify the main reactions during the calcination stage and investigate the kinetics of the identified reactions.

4.4.2 Tube Furnace Experiments

The calcination experiments were carried out in a horizontal tube furnace (RSRB 80–750/11, Nabertherm, Lilienthal, Germany). The furnace has a 1400 mm long quartz tube with a cylindrical heating zone. The dimensions of the heating zone are 750 mm in length and 76 mm in diameter. The image of the horizontal tube furnace is shown in Figure 4.4.

The thermal energy in an industrial-scale rotary kiln is usually provided by combustion of various fuels such as coal, oil, and natural gas. In the lab-scale experiments where electrically heated furnaces are used, the atmosphere of the furnace is simulated by purging specific gas compositions. The atmosphere resulted from coal combustion in the rotary kiln was simulated by purging various mixtures of N_2 , CO, CO_2 , and SO_2 gases in the furnace by controlling the individual gas flow rates using mass flow controllers (MC and MCS series, Alicat Scientific, Tucson, USA). The MC controllers are suitable for handling non-corrosive gases such as N_2 , CO, and CO_2 , while the MCS series are designed to handle corrosive gases like SO_2 . The cylindrical mixing column containing glass beads was placed after flow controllers to provide a homogenous gas mixture for the experiments. An extraction arm was used to collect the output gases from the exit end of the furnace. The gas sensors were utilized throughout the experiments to monitor the level of hazardous gases in the laboratory. Figure 4.5 illustrates the schematic of the custom-made setup for adjusting the furnace atmosphere. The experimental apparatus includes CO, CO_2 , SO_2 , and N_2 gas cylinders, their flow controllers, the mixing column, and the horizontal tube furnace connected to the extraction arm.



Figure 4.4 Horizontal tube furnace including (1) gas inlet, (2) quartz tube, (3) gas outlet, and (4) temperature controller.

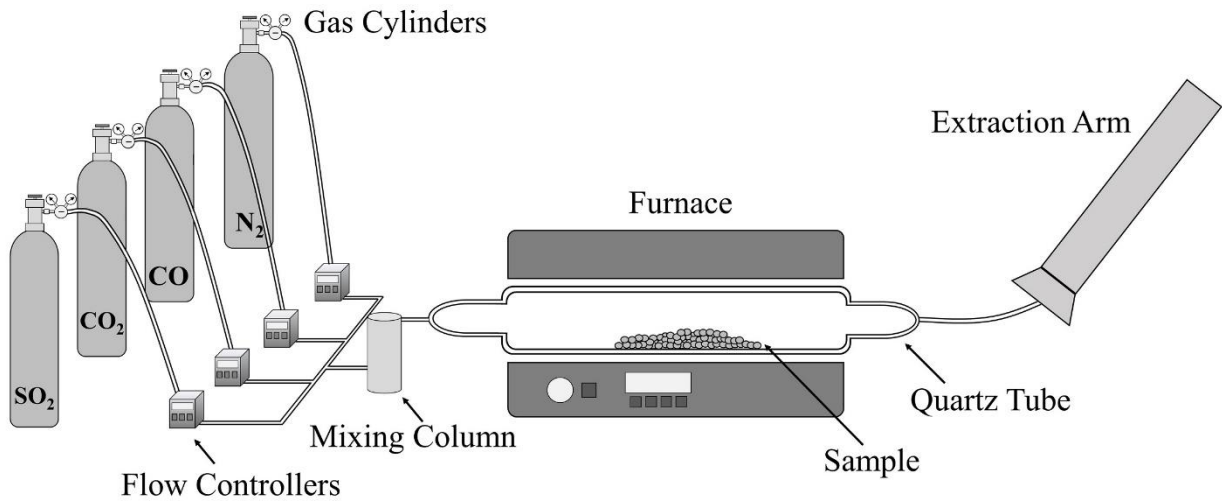


Figure 4.5 Schematic of the experimental setup used for the calcination experiments.

The samples were prepared by mixing 30 g of the laterite ore with 1.5 g of graphite as the reducing agent. In industry, coal as reductant is added in the range of 3.5-11 wt% [45]. We used 5 wt% graphite as a reasonable number within this range. Graphite was chosen as a reducing agent because of its negligible sulfur content compared with coal. This will minimize the effect of the sulfur content of the reducing agent on the sulfur department experiments. The samples were heated to the desired temperature in the range of 600-900 °C with a heating rate of 450 °C/h in a nitrogen atmosphere. The samples were then held at the selected temperature for 1 h in a specific atmosphere provided by purging various flow rates of N₂, CO, CO₂, and SO₂.

An additional thermocouple was employed once to compare the temperature inside of the tube and the one displayed by the furnace controller. Figure 4.6 indicates that both temperatures are very close to each other over the entire heating and cooling profile.

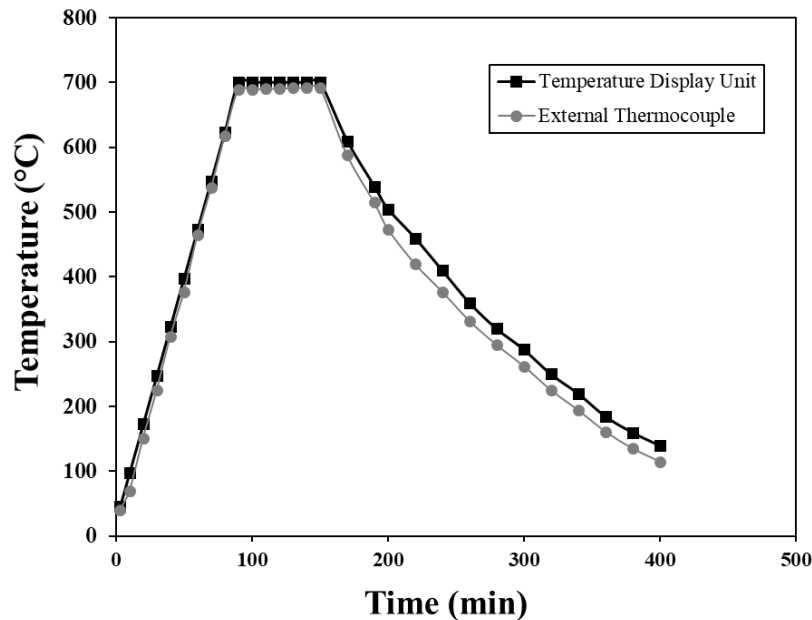


Figure 4.6 Calibration of the furnace temperature by comparing the temperature obtained by the external thermocouple and the one displayed by the furnace controller.

The effects of four primary operational variables on the sulfur content of the calcine were examined by varying each of the parameters independently. The effects of sulfur content of the burning coal, the reducing atmosphere, gas flow rate, and temperature on the sulfur content of the calcine are investigated. During nickel laterite calcination in the rotary kiln, sulfur present as an impurity in the rotary kiln fuel is oxidized and generates SO_2 . Therefore, the effect of the sulfur content of the fuel was modeled by varying P_{SO_2} in the gas mixture. Table 4.3 presents the experimental conditions for the calcination experiments to investigate the effects of the operational parameters (objective 2 in section 3.2). Further details on each series of experiments are presented in the following.

Table 4.3 Experimental conditions for calcination experiments on the effects of the operational parameters.

Sample code	CO (ml/min)	CO ₂ (ml/min)	SO ₂ (ml/min)	N ₂ (ml/min)	Total gas flow rate (ml/min)	Tem. (°C)	Equivalent %S in the burning coal	P_{SO_2} in the gas mixture
S1	23.7	5.9	0	27.7	57.3	900	0	0
S2	23.7	5.9	0.4	27.3	57.3	900	2	6.4×10^{-3}
S3	23.7	5.9	0.9	26.8	57.3	900	5	1.6×10^{-2}
S4	23.7	5.9	1.8	25.9	57.3	900	10	3.2×10^{-2}
S5	23.7	5.9	2.7	25	57.3	900	15	4.8×10^{-2}
C1	9.9	19.7	0.9	26.8	57.3	900	5	1.6×10^{-2}
C2	19.7	9.9	0.9	26.8	57.3	900	5	1.6×10^{-2}
C3	23.7	5.9	0.9	26.8	57.3	900	5	1.6×10^{-2}
C4	26.3	3.3	0.9	26.8	57.3	900	5	1.6×10^{-2}
C5	27	2.6	0.9	26.8	57.3	900	5	1.6×10^{-2}
F1	11.8	2.9	0.4	13.4	28.5	900	5	1.6×10^{-2}
F2	23.7	5.9	0.9	26.8	57.3	900	5	1.6×10^{-2}
F3	47.4	11.8	1.8	53.6	114.6	900	5	1.6×10^{-2}
F4	71.1	17.7	2.7	80.4	171.9	900	5	1.6×10^{-2}
F5	94.8	23.6	3.6	107.2	229.2	900	5	1.6×10^{-2}
T1	94.8	23.6	3.6	107.2	229.2	600	5	1.6×10^{-2}
T2	94.8	23.6	3.6	107.2	229.2	700	5	1.6×10^{-2}
T3	94.8	23.6	3.6	107.2	229.2	800	5	1.6×10^{-2}
T4	94.8	23.6	3.6	107.2	229.2	900	5	1.6×10^{-2}
H1	94.8	23.6	10.8	100	229.2	900	15	4.8×10^{-2}

The initial gas flow rate was selected based on the molar ratio of carbon in coal to the sum of nickel and iron oxides in the ore, i.e., $C/(Fe_2O_3+NiO)$. For instance, the total gas flow rates of 57.3

and 229.2 ml/min are equivalent to $C/(Fe_2O_3+NiO)$ of 1 and 4, respectively. The total gas flow rate corresponds to the gas mixture generated as a result of the combustion of coal used as a fuel in the rotary kiln. The values of the constant parameters in the experimental series were selected to be in the same range as the operational parameters of industrial rotary kilns.

The effect of the sulfur content of coal was investigated in S sample series. Higher SO_2 flow rates imply higher sulfur content of the coal. The effect of complete vs. incomplete coal combustion are examined in C sample series. Higher CO/lower CO_2 flow rates indicate incomplete coal combustion and a stronger reducing atmosphere. The effect of the process temperature and total gas flow rate were investigated in T and F series, respectively. Also, the high sulfur content sample (H1) was prepared to identify sulfur-containing compound in the calcine. In order to perform a fundamental study and isolate the effect of a target parameter on sulfur behavior, all other experimental parameters were maintained constant. It should be noted that in an industrial setting, the location of the fuel burner at one end of the furnace and the chemical reactions that occur between the gas and the solid phase result in variations in the temperature and furnace atmosphere along the kiln axis.

The next series of experiments correspond to the kinetics of the sulfur deportation in the calcination process (objective 3). The effect of two critical parameters, namely temperature, and P_{SO_2} on the kinetics of sulfur deportation were investigated. Three temperatures, i.e., 700, 800, and 900 °C, and eight processing times in the range of 15-120 min were used to examine the kinetics of the sulfurization process. The total gas flow rate, CO/ CO_2 , and sulfur content of the burning coal were maintained constant as 229.2 ml/min, 4, and 5%, respectively. The experimental conditions of the effect of temperature on the kinetics of the sulfur deportation are summarized in Table 4.4.

Table 4.4 Experimental conditions for the samples calcined at various temperatures to investigate the kinetics of sulfur deportation.

Sample code	Proc. time (min)	Temp. (°C)	Equivalent %S in the burning coal	CO (ml/min)	CO ₂ (ml/min)	SO ₂ (ml/min)	N ₂ (ml/min)
T1-K1	15	700	5	94.8	23.6	3.6	107.2
T1-K2	30	700	5	94.8	23.6	3.6	107.2
T1-K3	45	700	5	94.8	23.6	3.6	107.2
T1-K4	60	700	5	94.8	23.6	3.6	107.2
T1-K5	75	700	5	94.8	23.6	3.6	107.2
T1-K6	90	700	5	94.8	23.6	3.6	107.2
T1-K7	105	700	5	94.8	23.6	3.6	107.2
T1-K8	120	700	5	94.8	23.6	3.6	107.2
T2-K1	15	800	5	94.8	23.6	3.6	107.2
T2-K2	30	800	5	94.8	23.6	3.6	107.2
T2-K3	45	800	5	94.8	23.6	3.6	107.2
T2-K4	60	800	5	94.8	23.6	3.6	107.2
T2-K5	75	800	5	94.8	23.6	3.6	107.2
T2-K6	90	800	5	94.8	23.6	3.6	107.2
T2-K7	105	800	5	94.8	23.6	3.6	107.2
T2-K8	120	800	5	94.8	23.6	3.6	107.2
T3-K1	15	900	5	94.8	23.6	3.6	107.2
T3-K2	30	900	5	94.8	23.6	3.6	107.2
T3-K3	45	900	5	94.8	23.6	3.6	107.2
T3-K4	60	900	5	94.8	23.6	3.6	107.2
T3-K5	75	900	5	94.8	23.6	3.6	107.2
T3-K6	90	900	5	94.8	23.6	3.6	107.2
T3-K7	105	900	5	94.8	23.6	3.6	107.2
T3-K8	120	900	5	94.8	23.6	3.6	107.2

The next experiments were designed to examine the effect of P_{SO_2} on the kinetics of sulfur deportation. The samples were calcined at three different partial pressures of SO_2 , 6.4×10^{-3} , 1.6×10^{-2} , and 2.6×10^{-2} , which correspond to 2, 5, and 8% sulfur in the burning coal. Each sample was calcined for 8 processing durations in the range of 15-120 min. The total gas flow rate, CO/CO_2 , and the calcination temperature were maintained constant as 229.2 ml/min, 4, and 800 °C, respectively. Experimental conditions for the effect of the P_{SO_2} on the kinetics of sulfur deportation are shown in Table 4.5. Considering the required time for heating up and cooling down of the furnace, completion of each calcination experiment typically requires one day. After the cool down period, the quartz tube is taken out of the furnace, and the calcine is discharged manually. It is worth mentioning that the gas flow rates were selected based on simulating the atmosphere resulted from coal combustion. The gases with specific flow rates were mixed and purged to the system as the input gas. In other words, the effect of the parameters associated with coal combustion was examined systematically by controlling the individual flow rates of the input gas species. As a result of the calcination, partial reduction, and sulfurization reactions, the partial pressures of the gases in the furnace will be different from their initial values.

Table 4.5 Experimental conditions for the samples calcined at various P_{SO_2} to investigate the kinetics of sulfur deportation.

Sample code	Proc. time (min)	Equivalent %S in the burning coal	P_{SO_2} in the gas mixture	Temp. (°C)	CO (ml/min)	CO ₂ (ml/min)	SO ₂ (ml/min)	N ₂ (ml/min)
S1-K1	15	2	6.4×10^{-3}	800	94.8	23.6	1.4	109.4
S1-K2	30	2	6.4×10^{-3}	800	94.8	23.6	1.4	109.4
S1-K3	45	2	6.4×10^{-3}	800	94.8	23.6	1.4	109.4
S1-K4	60	2	6.4×10^{-3}	800	94.8	23.6	1.4	109.4
S1-K5	75	2	6.4×10^{-3}	800	94.8	23.6	1.4	109.4
S1-K6	90	2	6.4×10^{-3}	800	94.8	23.6	1.4	109.4
S1-K7	105	2	6.4×10^{-3}	800	94.8	23.6	1.4	109.4
S1-K8	120	2	6.4×10^{-3}	800	94.8	23.6	1.4	109.4
S2-K1	15	5	1.6×10^{-2}	800	94.8	23.6	3.6	107.2
S2-K2	30	5	1.6×10^{-2}	800	94.8	23.6	3.6	107.2
S2-K3	45	5	1.6×10^{-2}	800	94.8	23.6	3.6	107.2
S2-K4	60	5	1.6×10^{-2}	800	94.8	23.6	3.6	107.2
S2-K5	75	5	1.6×10^{-2}	800	94.8	23.6	3.6	107.2
S2-K6	90	5	1.6×10^{-2}	800	94.8	23.6	3.6	107.2
S2-K7	105	5	1.6×10^{-2}	800	94.8	23.6	3.6	107.2
S2-K8	120	5	1.6×10^{-2}	800	94.8	23.6	3.6	107.2
S3-K1	15	8	2.6×10^{-2}	800	94.8	23.6	5.8	105
S3-K2	30	8	2.6×10^{-2}	800	94.8	23.6	5.8	105
S3-K3	45	8	2.6×10^{-2}	800	94.8	23.6	5.8	105
S3-K4	60	8	2.6×10^{-2}	800	94.8	23.6	5.8	105
S3-K5	75	8	2.6×10^{-2}	800	94.8	23.6	5.8	105
S3-K6	90	8	2.6×10^{-2}	800	94.8	23.6	5.8	105
S3-K7	105	8	2.6×10^{-2}	800	94.8	23.6	5.8	105
S3-K8	120	8	2.6×10^{-2}	800	94.8	23.6	5.8	105

As described in chapter 3, the last objective of this study is to investigate potential solutions to reduce the sulfur content of the calcine. This objective is tackled by using CaCO_3 additive to absorb sulfur from the atmosphere and reduce the sulfur content of the calcine. The CaCO_3 additive in powder form was placed between the laterite ore and the gas entrance point in order to absorb SO_2 gas. Basically, the gas became in contact with the sulfur absorber prior to reacting with the laterite ore. For each experiment, 7.5 g laterite ore was mixed with 0.375 g graphite. 0.6 g CaCO_3 was used as the additive, which equals 8 wt% of the ore. The molar ratio of CaCO_3 to SO_2 purged in the system for 1 h was 2.7. These experiments were carried out in an alumina tube which was placed inside the original quartz tube of the horizontal furnace. The length and diameter of the alumina tube are 1400 mm and 20 mm respectively. The schematic image of the experimental setup including alumina tube is shown in Figure 4.7. Because of the reduced diameter of the quartz tube at its ends, it is not feasible to discharge the calcine without contaminating it with the additive. Therefore, the alumina tube is used to allow the discharge of the calcine and prevent mixing between the additive and the calcine.

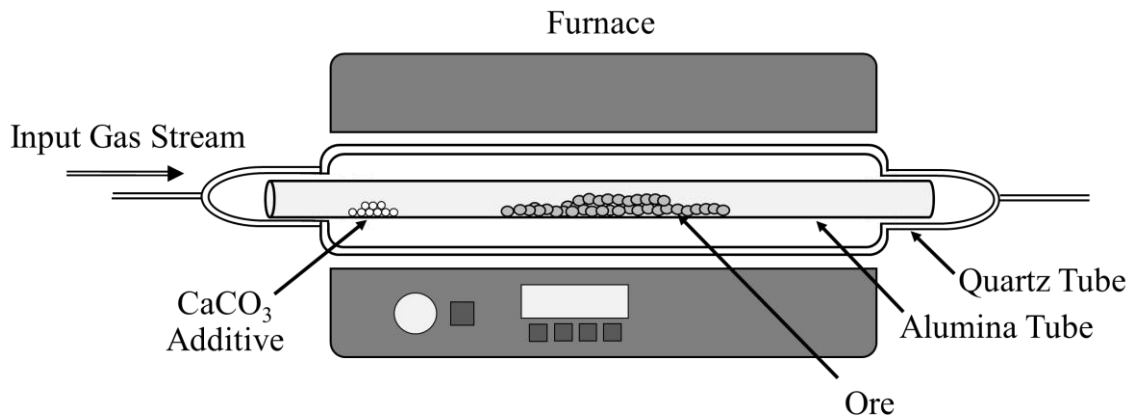


Figure 4.7 Experimental setup for investigating the effect of CaCO_3 additive on the sulfur content of the calcine.

The effects of calcination time and temperature on inhibiting sulfur transfer to the calcine were investigated. Table 4.6 shows the experimental conditions for samples calcined at various processing times (30, 60, and 120 min) and temperatures (700, 800, and 900 °C) in the presence and absence of CaCO₃. It should be mentioned that 7.5 g of the ore was used in these experiments and the total gas flow rate was selected as 57.3 ml/min, which equivalent to C/(Fe₂O₃+NiO)=4. The characters of A and B as the initials of the sample codes correspond to the absence and presence of CaCO₃ additive, respectively. The second character in the sample codes presents processing time (P) or temperature (T).

Table 4.6 Experimental conditions for the samples calcined at various processing times and temperatures to investigate the effect of CaCO₃ additive on sulfur content of the calcine.

Sample code	CaCO ₃ additive (gr)	Proc. time (min)	Temp. (°C)	Equivalent %S in the burning coal	CO (ml/min)	CO ₂ (ml/min)	SO ₂ (ml/min)	N ₂ (ml/min)
A-P1	0	30	800	5	23.7	5.9	0.9	26.8
A-P2	0	60	800	5	23.7	5.9	0.9	26.8
A-P3	0	120	800	5	23.7	5.9	0.9	26.8
B-P1	0.6	30	800	5	23.7	5.9	0.9	26.8
B-P2	0.6	60	800	5	23.7	5.9	0.9	26.8
B-P3	0.6	120	800	5	23.7	5.9	0.9	26.8
A-T1	0	60	700	5	23.7	5.9	0.9	26.8
A-T2	0	60	800	5	23.7	5.9	0.9	26.8
A-T3	0	60	900	5	23.7	5.9	0.9	26.8
B-T1	0.6	60	700	5	23.7	5.9	0.9	26.8
B-T2	0.6	60	800	5	23.7	5.9	0.9	26.8
B-T3	0.6	60	900	5	23.7	5.9	0.9	26.8

4.5 Analytical Techniques and Sample Preparation

4.5.1 Inductively Coupled Plasma Optical Emission Spectroscopy

Inductively coupled plasma optical emission spectrometry (ICP-OES, Varian 725-ES ICP spectrometer, Agilent Technologies, Santa Clara, USA) was used to measure the sulfur content of the samples.

The calcine was ground in the ball mill grinder for 5 min (Figure 4.8). The ground calcine was fused with an alkali salt to make it soluble in acid. 0.2 g of the ground calcine was mixed with 3 g of KOH pellets. The mixture was charged in a zirconium crucible and placed in the muffle furnace (Figure 4.9). The sample was heated at 450 °C for 2 h and then slowly cooled down to room temperature. The fused sample was dissolved in dilute nitric acid that was prepared by mixing 14 ml of nitric acid (70% HNO₃) and 21 ml of distilled water. Finally, the sulfur content of the sample was measured by ICP-OES analysis.

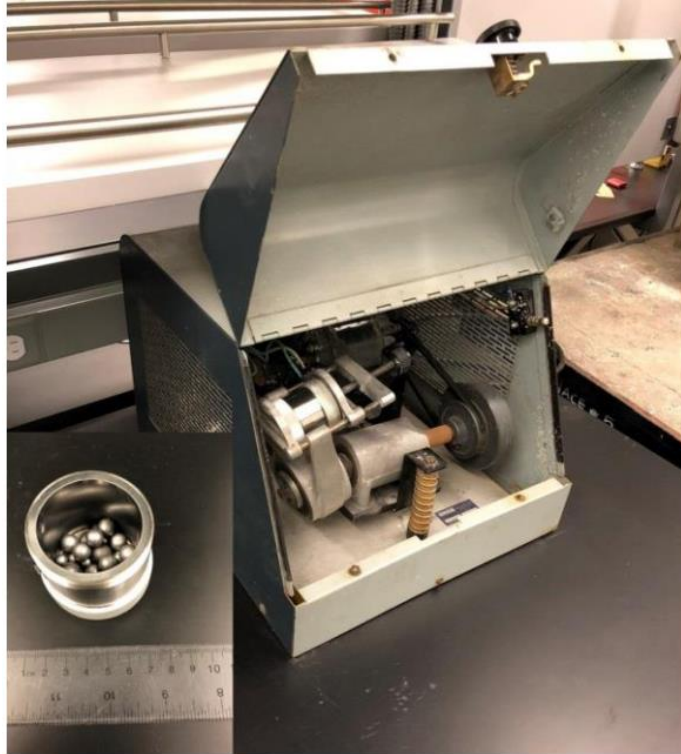


Figure 4.8 The ball mill grinder.



Figure 4.9 Muffle furnace.

4.5.2 X-ray Diffraction, Scanning Electron Microscopy and Energy Dispersive X-ray Spectroscopy

The mineralogy of the samples was determined by X-ray diffractometer (MultiFlex, Rigaku Corporation, Tokyo, Japan) using a Cu K α radiation ($\lambda = 1.54056 \text{ \AA}$). The samples were observed using a scanning electron microscope (Quanta 650, FEI Company, Oregon, USA). Energy dispersive spectroscopy (EDS) was utilized to investigate the elemental composition of various regions of the samples. SEM-EDS in this study was a semi-quantitative analysis to provide approximate chemical composition of the samples. Specially the raw and unpolished surface of the samples in chapter 6 and 7 provide X-ray signals in different directions which implies a semi-quantitative analysis [107].

Chapter 5: Kinetic Analysis on Nickel Laterite Calcination

5.1 Introduction

Characterization of the nickel laterite ore and investigating its calcination behavior is the primary step to understand the sulfur deportation in the calcination stage. In this section, the main reactions that occur during the calcination stage are identified by employing TGA-DSC, XRD, and SEM-EDS analyses. The kinetic parameters for the main reactions are obtained using a novel approach of combining model-free and model-fitting methods. Furthermore, the best kinetic model for the main reactions is identified by comparing the activation energy obtained by model-free and model-fitting methods.

5.2 Phase Transformation and Reactions during the Calcination Process

In order to determine the reactions and phase transformations during the calcination of the laterite ore, TGA/DSC test was conducted at 25-1000 °C. Figure 5.1 demonstrates the change of mass and heat flow versus temperature for the raw laterite ore. As indicated in the heat flow (DSC) plot in Figure 5.1, 4 main peaks are present at about 100, 300, 600, and 800 °C. The temperature range for the reactions was determined considering the deviation of the DSC curve from the baseline [108]. The temperature ranges of the main reactions are identified as 220-320, 550-650, and 780-820 °C. Considering the TGA/DSC results, various samples were collected from intermediate temperatures and analyzed using XRD. The results are shown in Figure 5.2.

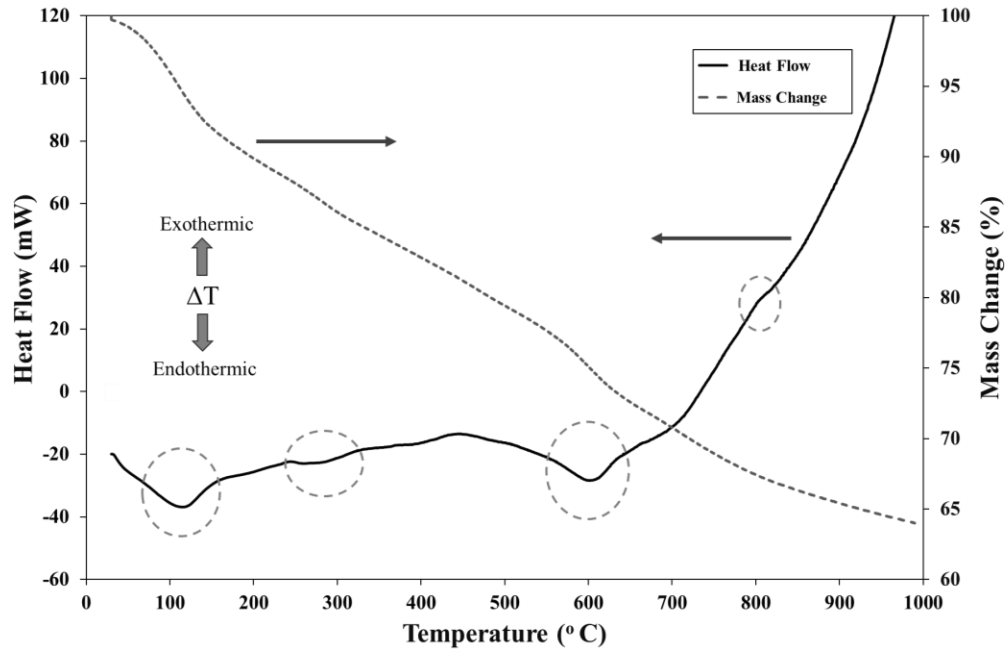


Figure 5.1 TGA-DSC analysis of the raw laterite ore.

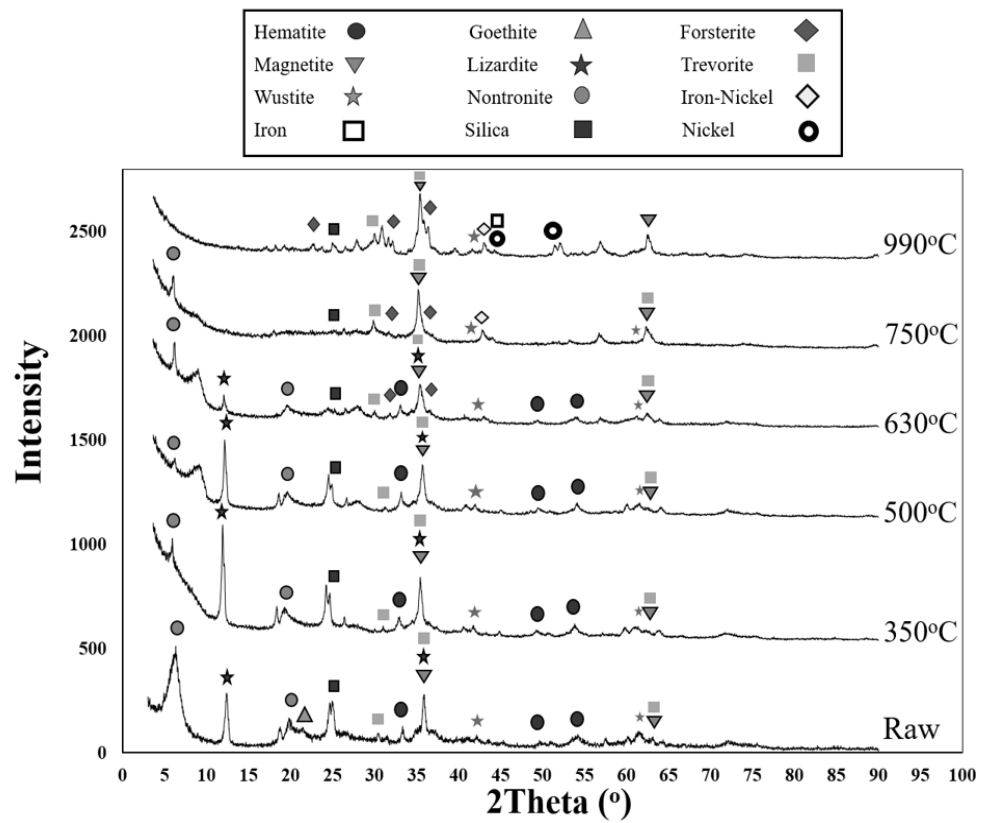
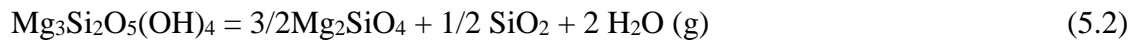


Figure 5.2 XRD patterns for the raw laterite ore and the samples collected after non-isothermal reduction at 350, 500, 630, 750, and 990 °C.

The first endothermic peak at about 100 °C, with 4 % mass loss in the TGA plot, is associated with the evaporation of free water. The second endothermic peak at about 300 °C, with 4% mass loss, corresponds to the transformation of goethite to hematite with the dehydroxylation reaction presented in equation 5.1 [49, 50, 67, 109]. The main goethite peak in the XRD spectra is not observed at 350 °C; this is attributed to the transformation of goethite to hematite.



The next endothermic peak at 600 °C with 4.5% mass loss is associated with the dissociation of lizardite to forsterite and silica with the loss of the hydroxyl group (reaction 5.2) [49, 51, 110].



Comparison between the XRD patterns of the samples heated at 500 and 630 °C (Figure 5.2) reveals that a decrease in the intensity of lizardite peaks is accompanied by the appearance of forsterite peaks at 630 °C. This observation is in agreement with the occurrence of reaction 5.2.

The last exothermic peak at about 800 °C pertains to silicate decomposition, which is in agreement with the XRD results showing the elimination of nontronite [49]. The increase in temperature leads to a gradual decrease in the intensity of lizardite and nontronite peaks in the XRD patterns due to the removal of the hydroxyl groups. According to the XRD results presented in Figure 5.2, complete dissociations of lizardite and nontronite compounds occur at 750 and 990 °C, respectively.

5.3 SEM-EDS Analysis of the Calcined Samples

Figure 5.3 shows backscattered SEM images of the raw and processed ore at 990 °C. The approximate chemical composition of the different regions in SEM images was obtained by EDS

analysis. The EDS results associated with the five main regions marked in Figure 5.3 are presented in Table 5.1.

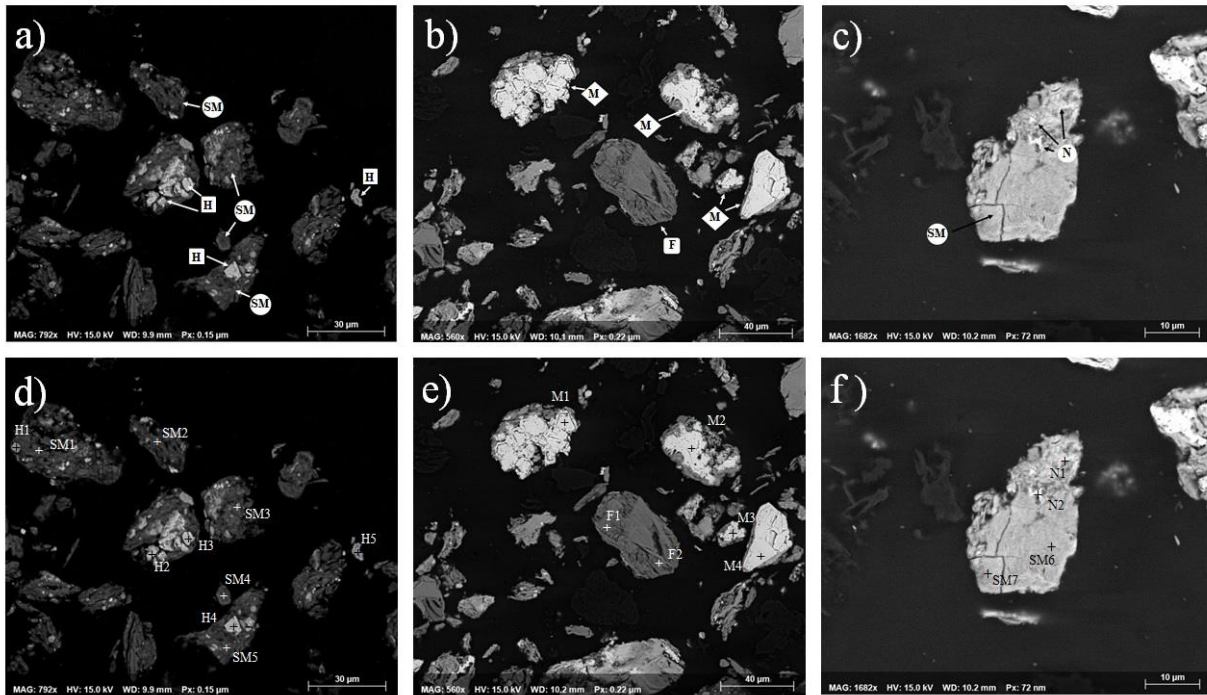


Figure 5.3 SEM images of (a) the raw laterite ore and (b, c) the calcined ore. Analysis points for EDS of (d) the raw laterite ore and (e, f) the calcined ore. H: hematite, SM: silica-magnesia area, M: magnetite, F: forsterite, N: nickel-rich region.

The EDS points are marked as SM (silica-magnesia), H (hematite), M (magnetite), F (forsterite), and N (nickel-rich region). The light gray particles in the raw material are mainly composed of hematite. Dispersed hematite particles are embedded in the silica-magnesia region. According to the percentages of iron and oxygen obtained from the EDS results, the bright phase in Figure 5.3 (b) was identified as magnetite. The comparison between the raw and the calcined ore images shows that most of the hematite phase is reduced to magnetite. Forsterite is observed as dark grey particles in the calcined ore (Figure 5.3 (c)). As explained in section 5.2, forsterite is the product

of lizardite dissociation (reaction 5.2). The small nickel-rich regions detected in the calcined ore are the result of the partial reduction of trevorite to the iron nickel-rich phase (Figure 5.3 (c)).

Table 5.1 The EDS analysis of the selected points on the raw laterite and calcined samples.

EDS Point	O (wt%)	Si (wt%)	Mg (wt%)	Fe (wt%)	Ni (wt%)	Mn (wt%)	Al (wt%)	Co (wt%)	S (wt%)	Cr (wt%)
SM1	37.5	28.4	7.8	21.4	1.3	0	3.6	0	0	0
SM2	37.7	30.6	12.9	15.3	3.5	0	0	0	0	0
SM3	36.2	25.5	8.9	22.5	3.1	0	3.8	0	0	0
SM4	33.1	26.8	7.9	25.8	2.8	0	3.6	0	0	0
SM5	37.5	25.9	8.7	23.4	2.9	0	0	0	0	1.6
SM6	37.2	29.9	7.8	21.1	2.6	0	1.4	0	0	0
SM7	34.8	28.3	9.4	20.1	4	0	2.7	0	0.7	0
Avg of SM	36.3	27.9	9.1	21.4	2.9	0	2.1	0	0.1	0.2
H1	34.5	6.5	0	59	0	0	0	0	0	0
H2	30.7	1.1	0	68.2	0	0	0	0	0	0
H3	29.7	0.8	0	69.5	0	0	0	0	0	0
H4	29	0.6	0	69.7	0	0	0	0	0	0.7
H5	29.7	3.2	0	65.7	0	0	0	0	0	1.4
Avg of H	30.7	2.5	0	66.4	0	0	0	0	0	0.4
M1	26.1	0	0	72.2	0	1.7	0	0	0	0
M2	25.8	0	0	74.2	0	0	0	0	0	0
M3	26.4	1.5	0	72.1	0	0	0	0	0	0
M4	25.5	0	0	74.5	0	0	0	0	0	0
Avg of M	25.9	0.4	0	73.3	0	0.4	0	0	0	0
F1	39.4	22.8	27.8	7.7	1.5	0	0	0	0	0.8
F2	40.3	23	28.4	6.9	1.4	0	0	0	0	0

Avg of F	39.9	22.9	28.1	7.3	1.4	0	0	0	0	0.4
N1	29.2	21.6	6.3	18.3	9.6	8.1	4.1	2.2	0.6	0
N2	24.9	12.3	3.7	16	16.2	9.9	7.8	6.9	2.3	0
Avg of N	27	17	5.1	17.1	12.9	9	5.9	4.6	1.4	0

5.4 Kinetic Analysis

Non-isothermal TGA tests were carried out to find the kinetic parameters and the appropriate reaction model. The kinetic study was done based on the mass loss measurement. The mass change is converted to a dimensionless value, known as the extent of reaction, according to equation 5.3:

$$\alpha = \frac{W_i - W}{W_i - W_f} \quad (5.3)$$

where W is the weight of the sample at time t , W_i and W_f are the initial and final weight of the sample, respectively. The degree of conversion, i.e., α , is equal to 0 and 1 at the beginning and the end of the reaction, respectively.

Two approaches, i.e., model-fitting and model-free methods, are considered to obtain the kinetic parameters and the reaction model of the main reactions that occur during the process. The general expression for the rate of the degree of conversion is presented in equation 5.4. [111]:

$$\frac{d\alpha}{dt} = f(\alpha)k(T) \quad (5.4)$$

where T is the temperature, t is the time, $f(\alpha)$ and $k(T)$ are functions of the extent of reaction and temperature, respectively. The temperature function is generally modeled using the Arrhenius equation:

$$k(T) = A \exp\left(\frac{-E}{RT}\right) \quad (5.5)$$

E is the activation energy, A is the pre-exponential factor, and R is the gas constant. Considering the non-isothermal conditions, the heating rate (β) is presented as equation 5.6.

$$\beta = \frac{dT}{dt} \quad (5.6)$$

Combining equations 5.4, 5.5, and 5.6 results in the general kinetic formula for non-isothermal condition as follows:

$$\frac{d\alpha}{dT} = \frac{A}{\beta} \exp\left(\frac{-E}{RT}\right) f(\alpha) \quad (5.7)$$

The integral form of the reaction model, $g(\alpha)$, is obtained using equation 5.8.

$$g(\alpha) = \int_0^{\alpha} \frac{d\alpha}{f(\alpha)} = \frac{A}{\beta} \exp\left(\frac{-E}{RT}\right) dT \quad (5.8)$$

Equation 5.8 is converted to equation 5.9 employing Coats Redfern method [112].

$$\ln\left[\frac{g(\alpha)}{T^2}\right] = \ln\left[\frac{AR}{\beta E} \left(1 - \frac{2RT}{E}\right)\right] - \frac{E}{RT} \quad (5.9)$$

Generally, $\frac{E}{RT}$ is significantly greater than 1 [112]. Therefore, $\left(1 - \frac{2RT}{E}\right)$ is approximately 1 and equation 5.9 can be simplified as equation 5.10.

$$\ln\left[\frac{g(\alpha)}{T^2}\right] = \ln\left[\frac{AR}{\beta E}\right] - \frac{E}{RT} \quad (5.10)$$

Plotting $\ln\left[\frac{g(\alpha)}{T^2}\right]$ versus $1/T$, E and A are calculated from the slope and the intercept, respectively.

Table 5.2 shows the list of the kinetic models used to estimate the kinetic parameters for the reactions that take place during calcination. Kinetic models are typically derived using low heating rates [113], thus, model-fitting approach was investigated employing a heating rate of 10 °C/min.

Table 5.2 List of the reaction models applied to investigate kinetics of nickel laterite ore calcination.

Reaction Model	Code	$f(\alpha)$	$g(\alpha)$
Contracting Cylinder	C2	$2(1-\alpha)^{1/2}$	$1-(1-\alpha)^{1/2}$
Contracting Sphere	C3	$3(1-\alpha)^{2/3}$	$1-(1-\alpha)^{1/3}$
1-D Diffusion	D1	$1/2\alpha^{-1}$	α^2
2-D Diffusion	D2	$[-\ln(1-\alpha)]^{-1}$	$(1-\alpha)\ln(1-\alpha)+\alpha$
3-D Diffusion	D3	$3/2(1-\alpha)^{3/2}[1-(1-\alpha)^{1/3}]^{-1}$	$[1-(1-\alpha)^{1/3}]^2$
Reaction Order (n=1)	R1	$(1-\alpha)$	$-\ln(1-\alpha)$
Reaction Order (n=2)	R2	$(1-\alpha)^2$	$(1-\alpha)^{-1} - 1$
Reaction Order (n=3)	R3	$(1-\alpha)^3$	$1/2[(1-\alpha)^{-2} - 1]$
Power Law (n=1)	P1	1	α
Power Law (n=2)	P2	$2\alpha^{1/2}$	$\alpha^{1/2}$
Power Law (n=3)	P3	$3\alpha^{2/3}$	$\alpha^{1/3}$
Avrami-Erofeev (n=2)	A2	$2(1-\alpha)[- \ln(1-\alpha)]^{1/2}$	$[- \ln(1-\alpha)]^{1/2}$
Avrami-Erofeev (n=3)	A3	$3(1-\alpha)[- \ln(1-\alpha)]^{2/3}$	$[- \ln(1-\alpha)]^{1/3}$
Avrami-Erofeev (n=4)	A4	$4(1-\alpha)[- \ln(1-\alpha)]^{3/4}$	$[- \ln(1-\alpha)]^{1/4}$

Another approach for kinetic analysis is isoconversional method also called model-free method. In this approach, the reaction rate at a constant value of α is solely temperature dependent. In model-free method, the kinetic parameters are calculated without imposing a reaction model. The principal advantage of model-free route is the ability to choose the appropriate reaction model by comparing model-free results with the ones obtained from model-fitting approach. The main

limitations of the model-free approach are failure to calculate separate E values for the parallel reactions that occur at the same extent of reaction and inability to fit kinetic models to the reactions [83, 92]. The limitation of average E calculation for parallel reactions in model-free approach is not applicable in this work, since the main reactions occur at considerably different temperatures around 300, 600, and 800 °C (Figure 5.1). The limitation of identifying the appropriate kinetic model by model-free approach is overcome by combining it with model-fitting approach. Another limitation of the model-free approach is associated with the error in E values if there is a significant deviation between sample temperature and the reference temperature [83]. This issue is overcome by conducting TGA experiment at a low heating rate (10 °C/min) for model-free approach to provide enough time for the sample to reach the reference temperature.

The two common model-free methods for calculating the activation energy as a function of α , are presented in Table 5.3. Five experiments with different heating rates were carried out to determine the activation energy (E) in the range of $\alpha=0.05-0.95$ with the step of $\alpha=0.05$. By plotting the left side of each equation relative to $1/T$, the activation energy is calculated from the slope of the line.

Table 5.3 List of model-free equations used to study the kinetics of nickel laterite ore reduction [114, 115].

Method Name	Equation
Flynn-Wall-Ozawa	$\ln(\beta_i) = Const - 1.052\left(\frac{E_\alpha}{RT_\alpha}\right)$
Kissinger-Akahira-Suonose	$\ln\left(\frac{\beta_i}{T_{\alpha,i}^2}\right) = Const - \frac{E_\alpha}{RT_\alpha}$

Mass loss and the degree of conversion curves of the calcined nickel laterite samples at various heating rates, i.e., 10, 20, 30, 40, and 50 °C /min, are illustrated in Figure 5.4 and Figure 5.5.

Increasing the heating rate causes a decrease in the mass loss and the rate of conversion, which are due to the insufficient reaction time. Four points with considerable change of slope in mass loss and degree of conversion curves are observed at about 100, 300, 600, and 800 °C. These temperatures correspond to the reaction temperatures and are in agreement with the temperatures obtained in section 5.2.

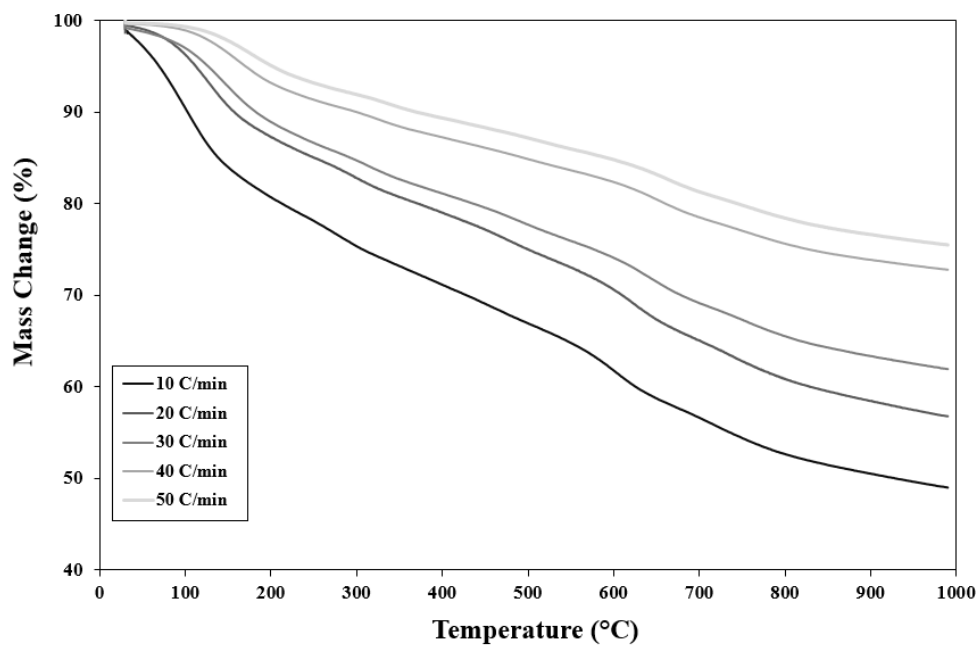


Figure 5.4 Mass change vs. temperature for the calcination process at various heating rates.

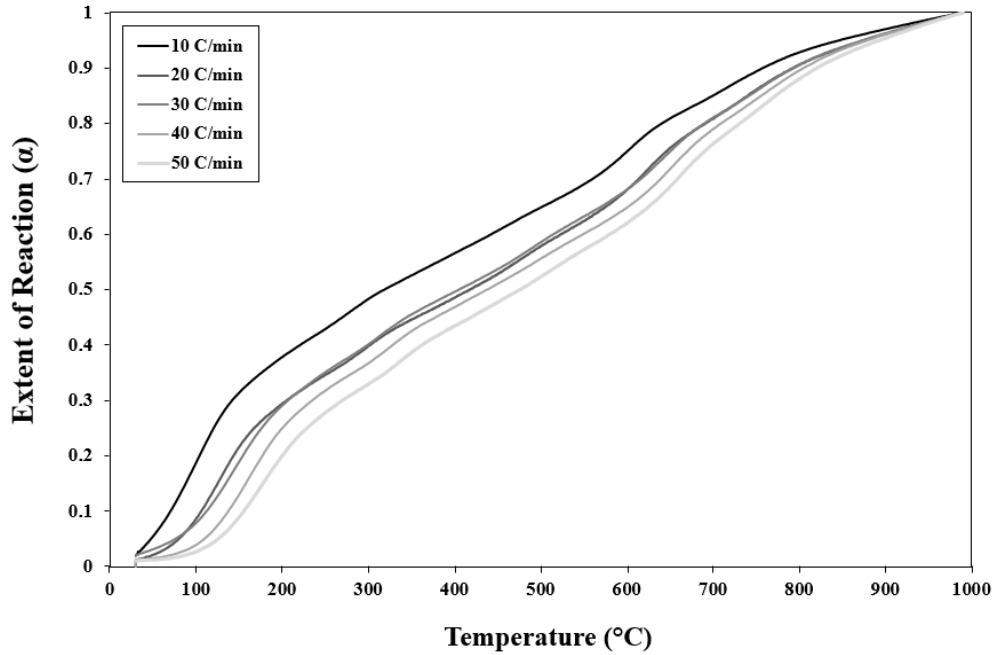


Figure 5.5 Extent of reaction vs. temperature for the calcination process at various heating rates.

The activation energy of the overall process was obtained by model-free method. $\ln(\beta_i)$ and $\ln\left(\frac{\beta_i}{T_{\alpha,i}^2}\right)$ which are the two common functions used in model-free methods are plotted versus $1/T$ in Figure 5.6 (a) and (b), respectively. Different values of heating rate, β , at various temperatures are required to obtain $\ln(\beta_i)$ or $\ln\left(\frac{\beta_i}{T_{\alpha,i}^2}\right)$ as a function of $1/T$. Therefore, the calcination process was carried out using five different heating rates. For each heating rate, nineteen different values of the extent of reaction, α , were selected between 0 and 1 using a step size of 0.05. Based on the model-free equations presented in Table 5.3, the activation energy is obtained from the slope of the linear regression lines (Figure 5.6).

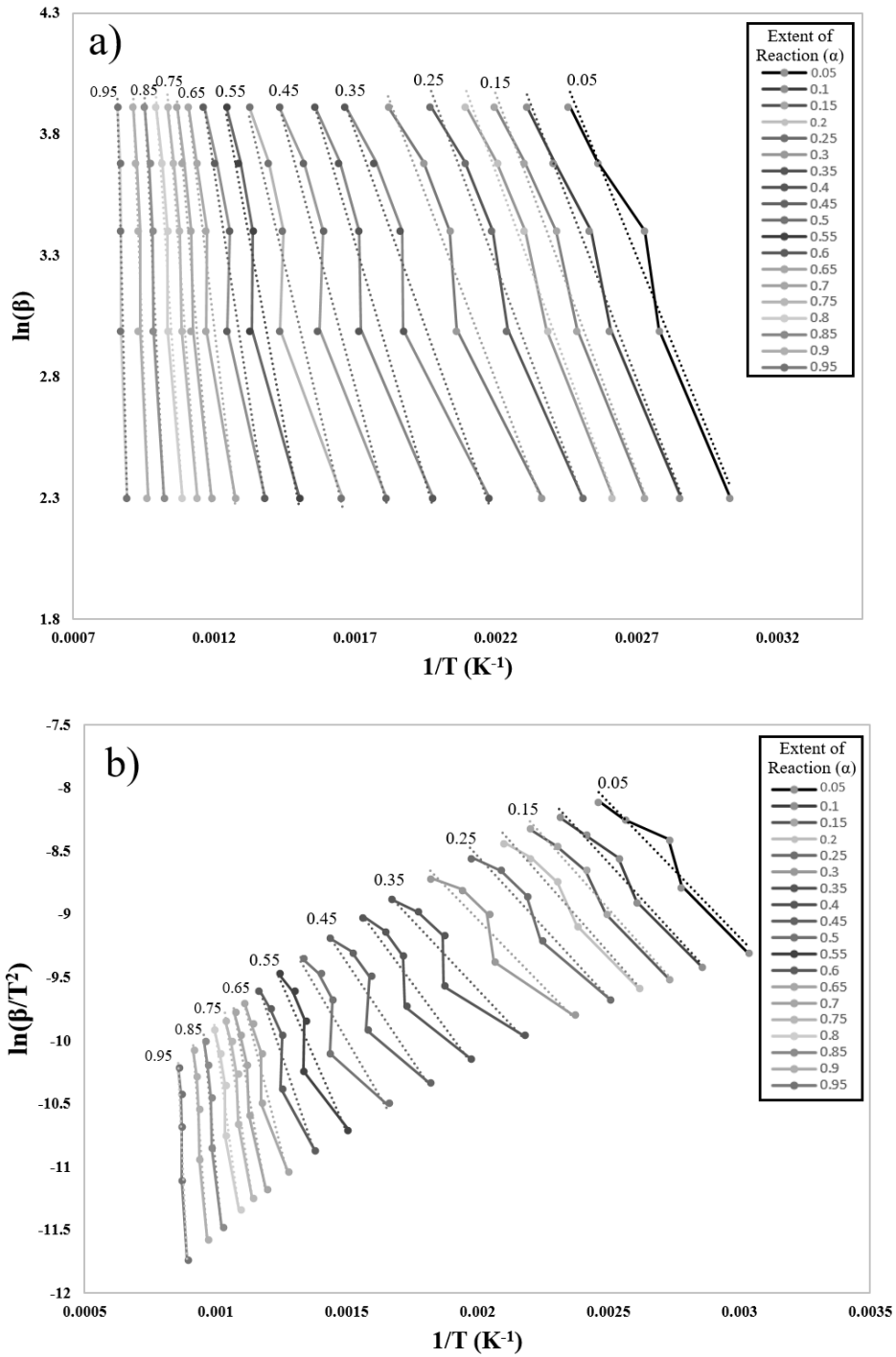


Figure 5.6 Regression lines for different extents of reactions based on (a) Flynn-Wall-Ozawa, and (b) Kissinger-Akahira-Suonose model-free methods.

The activation energy values achieved by Flynn-Wall-Ozawa and Kissinger-Akahira-Sunose methods for the entire process are shown in Figure 5.7. Both methods show a similar behavior for the activation energy, i.e., increasing from 25.2 to 310.6 kJ/mol and from 19.5 to 310.6 kJ/mol for Flynn-Wall-Ozawa and Kissinger-Akahira-Sunose methods, respectively. As mentioned in section 5.2, the main reactions occur at 300, 600, and 800 °C. At these temperatures, the activation energy is obtained by two model-free methods based on the slope of $\ln(\beta_i)$ and $\ln(\frac{\beta_i}{T_{\alpha,i}^2})$ versus $1/T$ for the entire process. Table 5.4 presents the range of the activation energy calculated by two model-free methods for the specific temperature ranges associated with the main reactions. Considering the significant difference between the activation energy values at different temperatures, developing a single kinetic model for the calcination process is not a suitable approach for investigating the kinetics of different reactions. To elucidate, the broad range of activation energy values implies the necessity of obtaining individual kinetics models for reactions that take place during the calcination process.

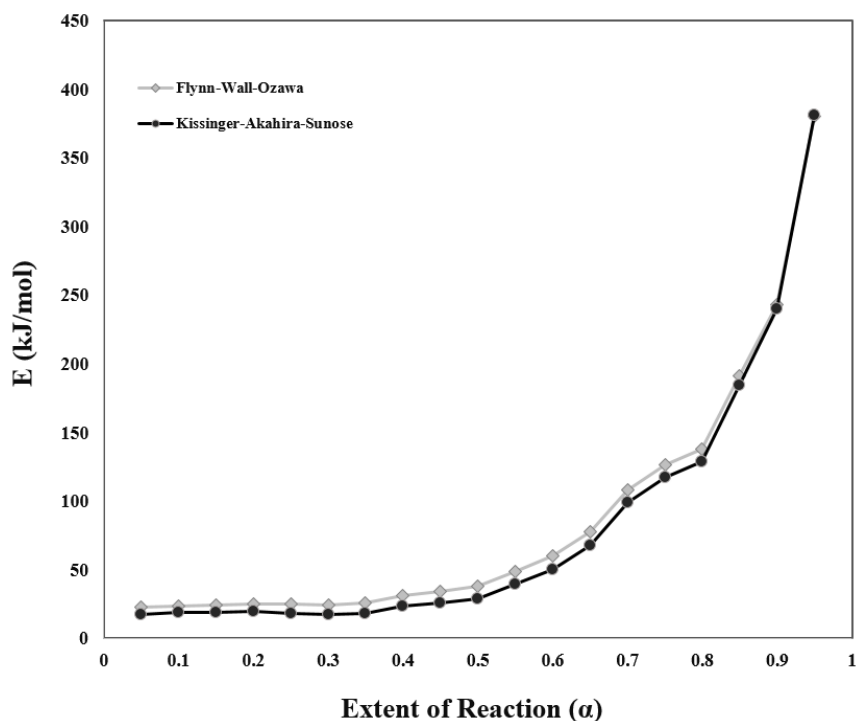


Figure 5.7 Activation Energy (E) as a function of the extent of reaction (α) obtained by two model-free methods.

Table 5.4 The range of the activation energy for the main reactions calculated by two model-free methods.

Range of Temperature for specific reaction ($^{\circ}\text{C}$)	Range of activation energy using Flynn-Wall-Ozawa method (kJ/mol)	Range of the activation energy using Kissinger-Akahira-Sunose method (kJ/mol)
220-320	25.2-39.4	19.5-29.3
550-650	60.1-137.8	50.2-128.9
780-820	191.4-310.6	184.5-310.6

Employing model-fitting method without model-free approach is not appropriate for kinetic analysis of complex processes due to the lack of clear distinction between the temperature dependence and the reaction model [116]. In this study, model-free method is carried out prior to

model-fitting method to avoid the aforementioned drawback. Model-fitting method is applied to the three temperature ranges associated with the three main reactions. For each of the three temperature ranges, $\ln\left[\frac{g(\alpha)}{T^2}\right]$ versus $1/T$ is plotted using the kinetic models described in Table 5.2. The values for E and A are calculated from the slope and the intercept of the regression lines, respectively.

The kinetic model for each reaction is selected based on the comparison between the activation energy values obtained from model-free and model-fitting methods. As stated earlier, the activation energy values for the three reactions are calculated using the model-free approach (Table 5.4). Subsequently, all kinetic models presented in Table 5.2 are fitted to the experimental data. The kinetic functions which yield an activation energy value in the range of the one obtained by model-free method, are selected as the potentially applicable kinetic models. Table 5.5 presents the kinetic models selected for each reaction, along with the E, A, and R^2 values. Table 5.5 displays the activation energy values measured from the slopes of the regression lines for $\ln\left[\frac{g(\alpha)}{T^2}\right]$ versus $1/T$. The activation energy values of Avrami-Erofeev and power law models are within the range of the values obtained by two model-free methods presented in Table 5.4. The Avrami-Erofeev equation with $n=3$ is considered to be the most suitable kinetic model for reactions at 300 and 800 °C due to the close activation energy values to the model-free method and the higher coefficient of determination compared to the power law model. For the reaction at 600 °C, Avrami-Erofeev ($n=2$) is selected as the kinetic model because of the high coefficient of determination, i.e., 0.94.

Table 5.5 Selected possible kinetic models for reactions that occur at 300, 600, and 800 °C.

Range of Temperature for specific reaction (°C)	Code	E(kJ/mol)	A(min ⁻¹)	R ²
220-320	AV3	24.5	24	0.84
220-320	P2	26.3	22	0.74
550-650	AV2	125.1	4.5E6	0.93
550-650	AV3	78.5	5.2E3	0.92
550-650	AV4	55.3	1.5E2	0.91
550-650	P2	85.5	1.1E4	0.80
780-820	AV3	273.1	4.8E12	0.94
780-820	P2	271.6	3.1E12	0.82

Avrami-Erofeev model describes processes that display sigmoidal behavior in their α -time curve. Sigmoidal curves reflect accelerated and decelerated conversion rates at the initial and final stages of the reaction, respectively. This model reaches the maximum rate of conversion at an intermediate stage of the reaction [83]. The physical interpretation of Avrami-Erofeev model is the nucleation and growth mechanism [117], which is typically used for kinetic analysis of decomposition, crystallization, crystallographic transition, and desolvation [118–121]. For instance, in lizardite dissociation, forsterite nucleates and grows at temperatures above 600 °C [122]. Transformation of goethite to hematite, dissociation of lizardite, and decomposition of silicates are the three main reactions identified in the calcination stage. Considering that the aforementioned reactions are solid-state reactions and they present high coefficient of determination values when modeled by Avrami-Erofeev equations, Avrami-Erofeev is chosen as the most suitable kinetic model for these reactions.

5.5 Conclusion

The main reactions that take place during the calcination of the nickel laterite ore are identified as transformation of goethite to hematite, dissociation of lizardite, and silicate decomposition. These reactions occur at 300, 600, and 800 °C, respectively. The activation energy raises from 19.5 to 310.6 kJ/mol with the increase in the extent of reaction. The activation energy values of the reactions at 300, 600, and 800 °C, determined by comparing the values obtained from model-free and model-fitting methods, are 24.5, 125.1, and 273.1 kJ/mol, respectively. The kinetic model for the reactions at 300 and 800 °C is identified as Avrami-Erofeev equation (n=3). The Avrami-Erofeev (n=2) is found to be the most suitable kinetic model for the reaction at 600 °C.

Chapter 6: Sulfur Department and the Effect of Operational Parameters on the Composition of the Calcine

6.1 Introduction

As described in chapter 3, there are very limited studies on sulfur department in nickel laterite calcination. In this chapter, the behavior of sulfur originated from fuel combustion in the calcination of nickel laterite is investigated. Moreover, the sulfurization reactions and the main sulfur-containing compound of the calcine are identified by thermodynamic simulation, XRD, and SEM-EDS analyses. The atmosphere resulted from coal combustion was mimicked by purging various mixtures of N₂, CO, CO₂, and SO₂ gases into the furnace. Thermodynamic analysis and high-temperature experiments were carried out to investigate the effect of operational parameters such as partial pressure of SO₂, the intensity of the reducing atmosphere, the gas flow rate, and the temperature on the calcine composition.

This chapter is divided into two main sections: thermodynamic analysis and high-temperature experiments. The sulfurization reactions and the effect of the operational parameters are discussed in detail in the following two sections.

6.2 Thermodynamic Analysis

The equilibrium composition of the system was determined using the equilibrium module of HSC Chemistry 5.11 [105]. 137 possible species, including 50 sulfur-containing compounds, were considered in the thermodynamic investigation. The list of the species is provided in appendix A. The analysis was performed to predict the equilibrium composition of the calcine and the main sulfur-containing compounds under different experimental conditions.

It should be noted that the results obtained by HSC simulation are based on pure thermodynamic analysis. HSC simulations are based on Gibbs free energy minimization method and do not consider the kinetic limitations of the process. The solution behavior of solid and gaseous species is not considered in the thermodynamic simulations and the activity coefficient of all the components is assumed to be equal to 1. This thermodynamic analysis also ignores the continuous supply of the gas mixture from outside the furnace and the removal of the gaseous compounds from the system.

6.2.1 Sulfur Department

Thermodynamic analysis of sulfur distribution was performed for sample S3 as a representative experimental condition. Figure 6.1 a and b show the equilibrium concentration of the main sulfur-containing compounds of the system in the range of 600-900 °C. Iron sulfides are the dominant sulfur-containing compound in the calcine, and COS is the major sulfur-containing gaseous compound. The equilibrium composition of the sulfur-containing gases prior to reaction with solids is shown in Figure 6.1 (c).

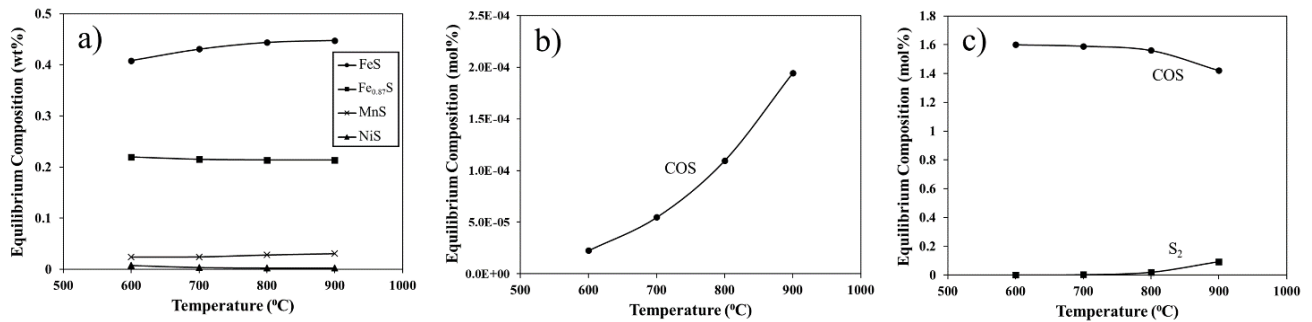


Figure 6.1 Equilibrium composition of the main sulfur-containing compounds in the (a) calcine, (b) gases reacted with solids, and (c) input gas mixture without reaction with solids.

HSC results presented in Figure 6.1 (c) imply that COS and S₂ are the main gaseous compounds that transfer sulfur from the gas to the solid phase. Considering the sulfur-containing compounds at solid-gas equilibrium, presented in Figure 6.1 (a and b), and the equilibrium composition of the sulfur-containing gases of the input gas mixture shown in Figure 6.1 (c), it is proposed that SO₂ and CO react with each other to form COS and S₂ which subsequently react with iron-containing components in the ore and form iron sulfide. Figure 6.2 depicts the proposed mechanism.

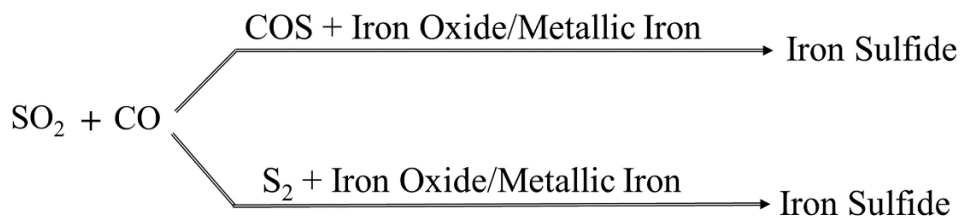


Figure 6.2 The sequence of the sulfur department reactions resulting in the formation of iron sulfide.

A list of the main possible sulfurization reactions in the system is given in Table 6.1. The reactions between SO₂ and CO produce intermediate gas species (reactions 1 and 2). Then, COS reacts with iron and iron oxides in the ore to form iron sulfides (reactions 3-6). Another gaseous species that can react with iron-containing compounds is S₂ (reactions 7-10). Considering the results presented in Figure 6.1 (c), COS is considered as the dominant gaseous compound for sulfurization reactions in the range of 600-900 °C. The overall sulfurization reactions (reactions 11-14) are derived from the sum of the reactions corresponding to S₂ or COS formation and the reactions between sulfur-containing gases and iron-containing compounds. The overall sulfurization reactions are presented in Table 6.1.

Table 6.1 List of the probable reactions associated with sulfur deportment in the system including laterite ore and N₂-CO-CO₂-SO₂ gas mixture at 900 °C.

Reaction	Formation of intermediate gas species	$\Delta G^{\circ}_{900^{\circ}\text{C}}$ (kJ/mol SO ₂)
1	$3\text{CO (g)} + \text{SO}_2 \text{(g)} = \text{COS (g)} + 2\text{CO}_2 \text{(g)}$	-86.9
2	$2\text{CO (g)} + \text{SO}_2 \text{(g)} = 1/2\text{S}_2 \text{(g)} + 2\text{CO}_2 \text{(g)}$	-84.7
Reaction	Reaction with COS	$\Delta G^{\circ}_{900^{\circ}\text{C}}$ (kJ/mol COS)
3	$1/2\text{Fe}_2\text{O}_3 + 1/2\text{CO (g)} + \text{COS (g)} = \text{FeS} + 3/2\text{CO}_2 \text{(g)}$	-98.5
4	$1/3\text{Fe}_3\text{O}_4 + 1/3\text{CO (g)} + \text{COS (g)} = \text{FeS} + 4/3\text{CO}_2 \text{(g)}$	-79.6
5	$\text{FeO} + \text{COS (g)} = \text{FeS} + \text{CO}_2 \text{(g)}$	-78.8
6	$\text{Fe} + \text{COS (g)} = \text{FeS} + \text{CO (g)}$	-85.8
Reaction	Reaction with S ₂	$\Delta G^{\circ}_{900^{\circ}\text{C}}$ (kJ/mol S ₂)
7	$\text{Fe}_2\text{O}_3 + 3\text{CO (g)} + \text{S}_2 \text{(g)} = 2\text{FeS} + 3\text{CO}_2 \text{(g)}$	-201.3
8	$2/3\text{Fe}_3\text{O}_4 + 8/3\text{CO (g)} + \text{S}_2 \text{(g)} = 2\text{FeS} + 8/3\text{CO}_2 \text{(g)}$	-163.4
9	$2\text{FeO} + 2\text{CO (g)} + \text{S}_2 \text{(g)} = 2\text{FeS} + 2\text{CO}_2 \text{(g)}$	-161.8
10	$2\text{Fe} + \text{S}_2 \text{(g)} = 2\text{FeS}$	-175.9
Reaction	Overall sulfurization reactions	$\Delta G^{\circ}_{900^{\circ}\text{C}}$ (kJ/mol SO ₂)
11	$1/2 \text{Fe}_2\text{O}_3 + 7/2\text{CO (g)} + \text{SO}_2 \text{(g)} = \text{FeS} + 7/2\text{CO}_2 \text{(g)}$	-185.4
12	$1/3 \text{Fe}_3\text{O}_4 + 10/3\text{CO (g)} + \text{SO}_2 \text{(g)} = \text{FeS} + 10/3\text{CO}_2 \text{(g)}$	-166.5
13	$\text{FeO} + 3\text{CO (g)} + \text{SO}_2 \text{(g)} = \text{FeS} + 3\text{CO}_2 \text{(g)}$	-165.6
14	$\text{Fe} + 2\text{CO (g)} + \text{SO}_2 \text{(g)} = \text{FeS} + 2\text{CO}_2 \text{(g)}$	-172.7

6.2.2 The Effect of Sulfur Content of the Burning Coal

The experimental conditions of the tests on the effect of P_{SO_2} are described in section 4.4.2 in Table 4.3 (samples S1-S5). The final % S in the calcine shown in Figure 6.3 (a) is obtained by thermodynamic modeling with HSC. The % S in the calcine is increased from 0.1 to 0.77% as the sulfur content of the burning coal raised from 2% ($P_{\text{SO}_2} = 6.4 \times 10^{-3}$ atm) to 15% ($P_{\text{SO}_2} = 4.8 \times 10^{-2}$ atm). As expected from reactions 11-14 in Table 6.1, higher levels of SO₂ results in the formation

of higher amounts of iron sulfides. Figure 6.3 (b) shows the effect of the sulfur content of coal on the equilibrium content of FeS and Fe_{0.87}S.

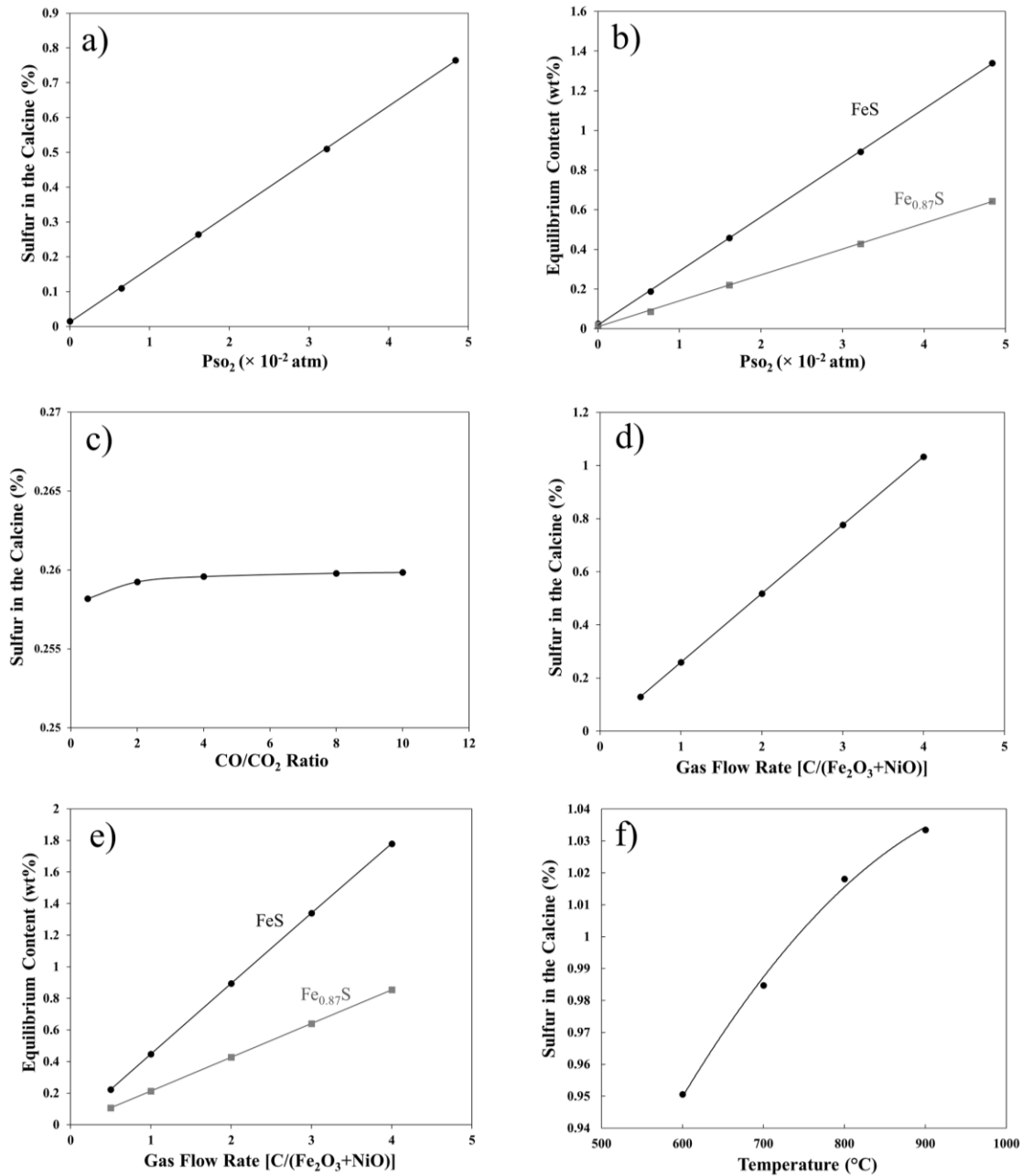


Figure 6.3 (a) Predicted %S in the calcine versus P_{SO_2} , (b) equilibrium content of sulfur compounds versus P_{SO_2} , (c) %S in the calcine versus CO/CO₂, (d) %S in the calcine versus gas flow rate, (e) equilibrium content of sulfur compounds versus gas flow rate and (f) %S in the calcine versus temperature (data obtained by HSC Chemistry 5.11 [105]).

6.2.3 The Effect of the Reducing Atmosphere (CO/CO₂)

Higher CO/CO₂ is associated with incomplete coal oxidation as a result of oxygen deficient combustion. CO plays a vital role in sulfur deportment by reacting with SO₂ and producing COS and S₂. As a result, it is expected that improvement of the reducing conditions, i.e., higher CO/CO₂, can facilitate the formation of sulfur compounds in the calcine. In order to examine the impact of the reducing atmosphere on the sulfur content of the calcine, %S in the burning coal was kept constant at 5%, which is considered a reasonable value for low quality/high sulfur coal [123]. As can be seen in Figure 6.3 (c), CO/CO₂ and the % S in the calcine are directly related to each other. It is worth noting that the increase in the equilibrium sulfur content as a result of higher CO/CO₂ is insignificant.

6.2.4 The Effect of the Total Gas Flow Rate

The gas flow rate is defined with respect to the molar ratio of carbon in the burning coal to the sum of Fe₂O₃ and NiO content of the raw ore. With a constant quantity of Fe₂O₃+NiO in the ore, a higher gas flow rate in the system translates to higher coal consumption per unit mass of the ore. In order to examine the influence of gas flow rate on the % S in the calcine, a gas mixture consisting of the amount of each gas for a one-hour experiment was considered as the gaseous input in the HSC model. The % S in the calcine versus gas flow rate is shown in Figure 6.3 (d). Increasing the ratio of CO+CO₂ to Fe₂O₃+NiO from 0.5 to 4 leads to an increase in % S from 0.13 to 1.04. As shown in Figure 6.3 (e), increasing the gas flow rate causes an increase in the equilibrium amounts of iron sulfides. It should be emphasized that the amount of SO₂ as one of the input materials in the system increases as the total gas flow rate increases. However, the HSC thermodynamic analysis ignores the kinetic factors such as continuous gas supply to the system and the effect of the gas flow rate on the gas velocity.

6.2.5 The Effect of the Temperature

Thermodynamic analysis of sulfur deportment was performed at various temperatures with 5% S in the burning coal, CO to CO₂ ratio of 4, and the total gas flow rate of 229.2 ml/min. The value for gas flow rate which is equivalent to C/(Fe₂O₃+NiO) of 4 is chosen considering coal consumption in three industrial plants. Coal consumption in nickel laterite rotary kilns in these plants is reported to be between 80 to 115 kg/ton [45]. Considering the carbon content of the coal and the iron and nickel contents of the ore, the ratio of C to Fe₂O₃+NiO is between 3 and 4.28 for these industrial plants. As presented in Table 6.1, the Gibbs free energy values of the sulfurization reactions are negative; hence, it is expected that the majority of sulfur that originate from SO₂ transfer to the calcine. The percentage of sulfur absorbed from SO₂ gas to the calcine is defined as sulfur deportation, which is presented as follows:

$$\% \text{ Sulfur deportation} = \frac{\text{Mass of sulfur in the calcine}}{\text{Total mass of input sulfur}} \times 100 \quad (6.1)$$

Based on the results of the thermodynamic Analysis, the sulfur deportation is 99.9% in the temperature range of 600-900 °C. The predicted sulfur content of the calcine at different temperatures is illustrated in Figure 6.3 (f). The % S in the calcine increased from 0.95 to 1.03% as the temperature raised from 600 to 900 °C. The slight increase in the sulfur content of the calcine is related to the higher mass loss due to reduction reactions, while the amount of sulfur transferred from the gas to the calcine is constant.

6.3 High-Temperature Experiments

6.3.1 Characterization of the Sulfur-Containing Compound

XRD analysis was used to identify the sulfur-containing compounds in the calcine. Sulfur-rich regions were further characterized using SEM/EDS analysis.

According to the thermodynamic evaluations, iron sulfide is predicted as the main sulfur-bearing compound in the calcine. Samples were analyzed by XRD to identify any distinction in the calcine composition due to the presence of SO₂ in the furnace atmosphere. The XRD patterns of the two samples shown in Figure 6.4 (a,b) reveal hematite (Fe₂O₃), magnetite (Fe₃O₄), wustite (FeO), iron (Fe), ferronickel (FeNi), graphite (C), trevorite (NiFe₂O₄), quartz (SiO₂), fayalite (Fe₂SiO₄), enstenite (MgSiO₃), forsterite (Mg₂SiO₄), and kyanite (Al₂SiO₅) as the main crystalline phases in the calcine. The only difference between samples S1 and H1 with XRD patterns labelled as (a) and (b) respectively is the presence of SO₂ in the furnace atmosphere. This allows for accurate identification of the sulfur-containing compound. The main difference between XRD patterns of the sample with high sulfur content (H1) and the one without sulfur (S1) is the iron sulfide peak (Figure 6.4). For further clarification, the magnified XRD patterns in the range of 27 to 33° are added in the upper right corner of Figure 6.4.

Since the concentration of sulfur in the calcine is considerably lower than other elements such as Si and Mg, some of the main peaks of the iron sulfide are not visible in the XRD pattern. Hence, to confirm the formation of iron sulfide and identify the exact compound, the iron sulfide particles were separated based on their metallic luster and yellow hue appearance. The separated particles were further characterized by XRD analysis. As shown in Figure 6.4 (c), all the major peaks of the sulfide phase are visible in the separated particles, and the exact phase of the main sulfur-bearing compound in the calcine is identified as pyrrhotite (Fe₇S₈). The primary peak for pyrrhotite is also observed in separated particles and sample H1 as shown in the upper right part of Figure 6.4.

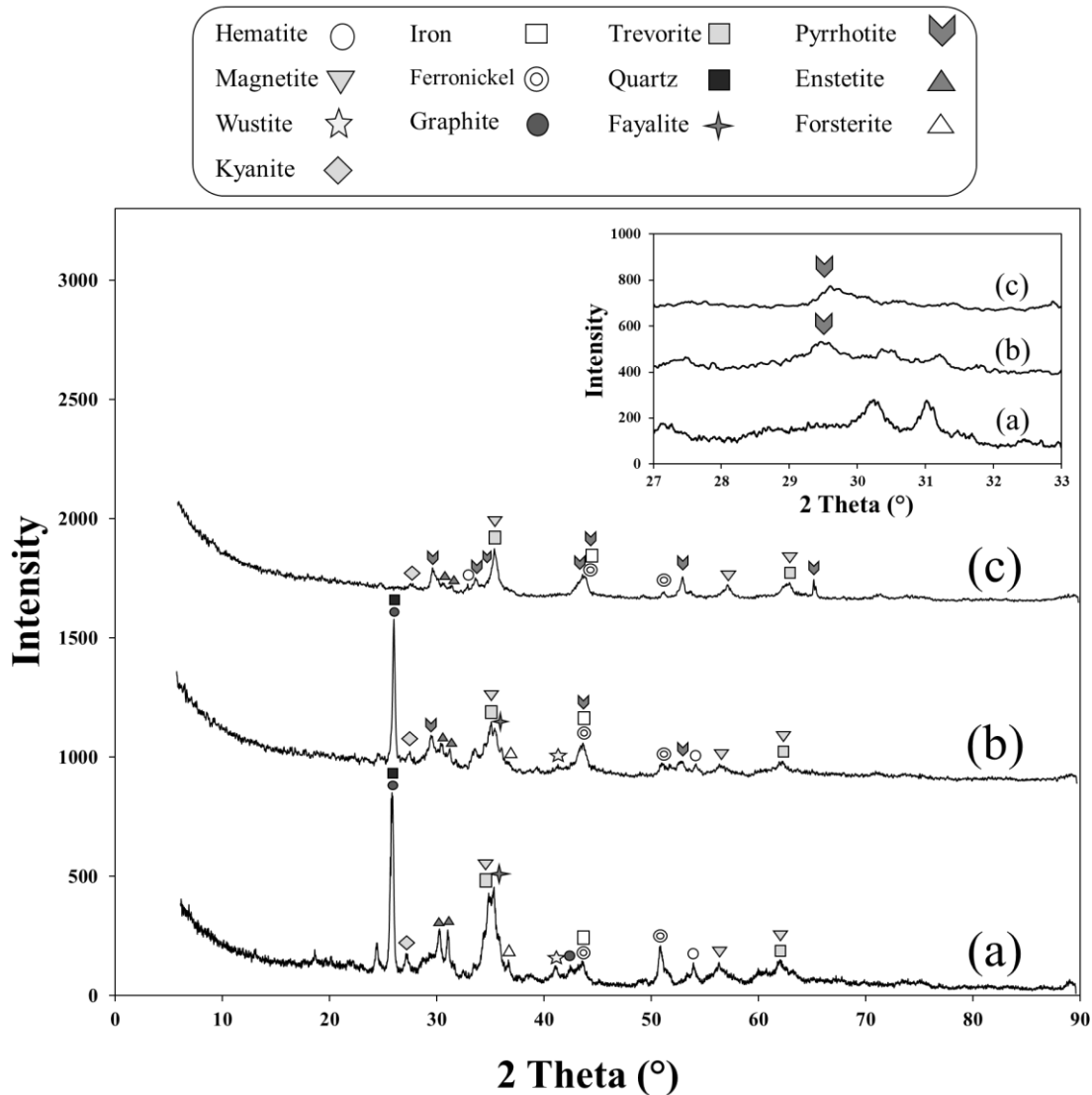


Figure 6.4 X-ray diffraction patterns of samples (a) S1, (b) H1, and (c) separated sulfide particles from sample H1.

SEM analysis was performed for sample F5 to examine sulfur-rich areas in the sample. Figure 6.5 and Figure 6.6 show SEM images and map analysis of sulfur, iron, oxygen, silicon, and nickel. The sulfur-rich zones were initially identified from the sulfur maps (Figure 6.5 (c) and Figure 6.6 (c)). EDS analysis was carried out to determine the approximate elemental composition of the sulfur-rich areas of the calcine. Figure 6.7 shows the sulfur-rich phase at different areas of the

sample. The EDS results presented in Table 6.2 confirm that sulfur in the sulfur-rich phase is primarily accompanied by iron. The results of SEM-EDS, XRD, and thermodynamic analyses are in agreement with each other.

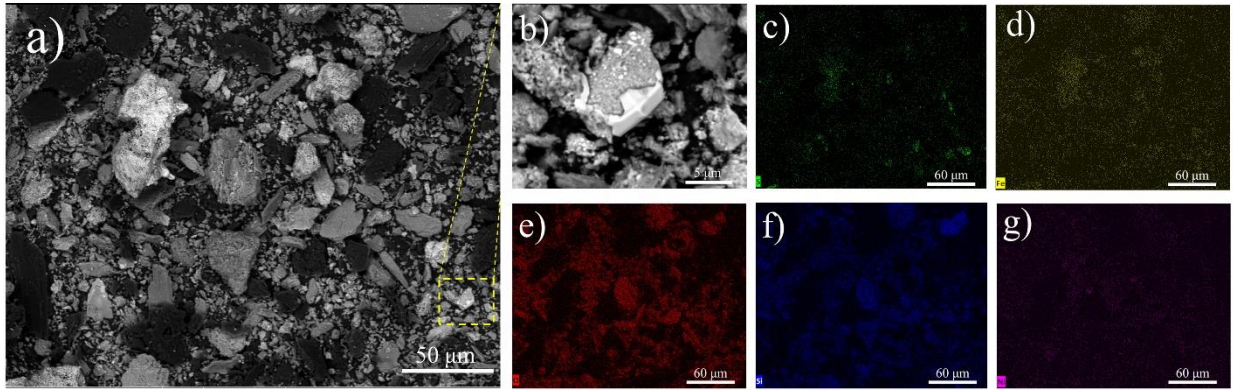


Figure 6.5 SEM image of sample (a) F5 and (b) sulfur-rich zone. EDS map analysis of (c) sulfur, (d) iron, (e) oxygen, (f) silicon, and (g) nickel.

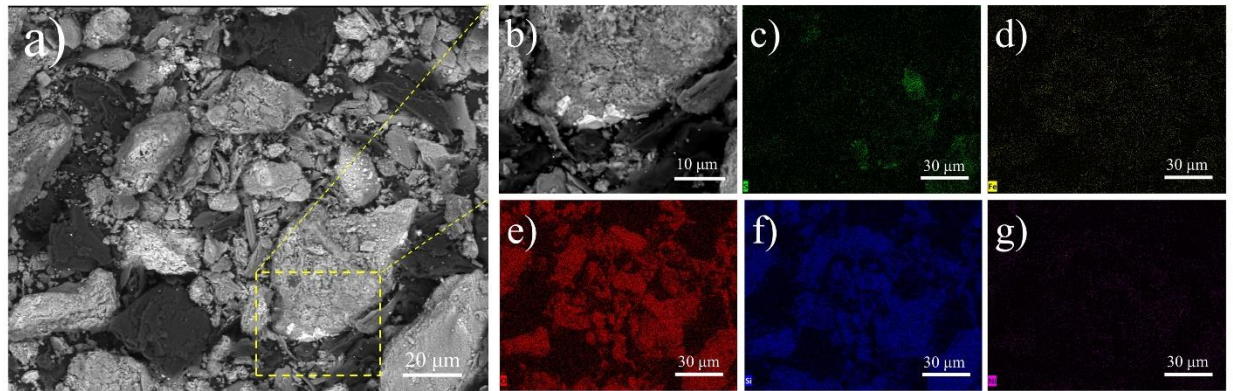


Figure 6.6 Additional SEM image of sample (a) F5 and (b) sulfur-rich zone. EDS map analysis of (c) sulfur, (d) iron, (e) oxygen, (f) silicon, and (g) nickel.

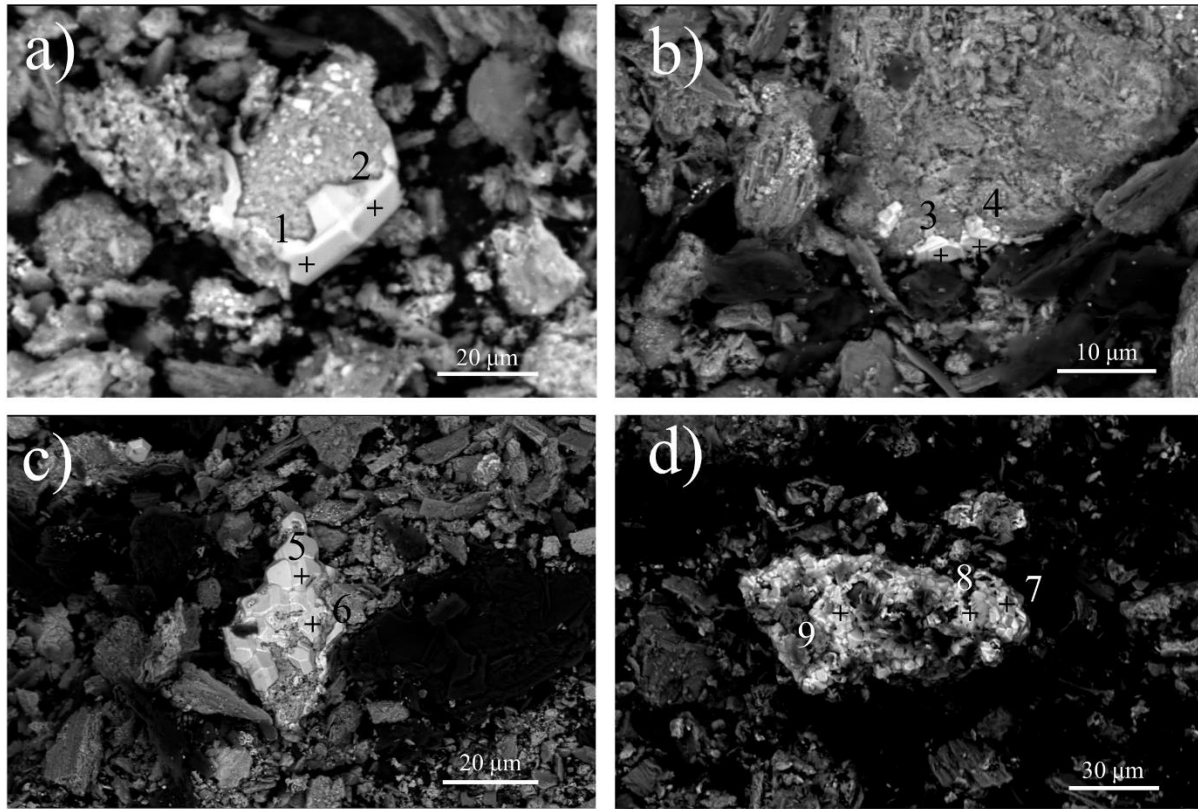


Figure 6.7 SEM images and EDS point analysis of various sulfur-rich zones in sample F5.

Table 6.2 EDS analysis of the selected points in sample F5.

EDS point	Fe (wt%)	S (wt%)	O (wt%)	Si (wt%)	Al (wt%)	Mn (wt%)	Ni (wt%)	Mg (wt%)
1	37.5	35.9	12.7	8.2	1.8	0.2	0	3.7
2	44.4	41.5	9.8	1.3	0	0.1	2.9	0
3	39.3	30.7	21.8	2.3	0	0.8	4.9	0.2
4	31.8	30	23.5	5.2	1.2	0.8	6.9	0.6
5	43.3	44.8	8.8	0.5	0	0.1	1.1	1.4
6	42.8	47.7	7.5	1.6	0	0.2	0	0.2
7	39.7	46.5	6.9	3.9	0.5	0.6	0.5	1.4
8	39.6	42.7	9.6	4.5	0.9	0.1	0.3	2.3

6.3.2 The Effect of Sulfur Content of the Burning Coal

The experimental results presented in Figure 6.8 show a direct correlation between P_{SO_2} in the atmosphere and the S% of the calcine. By increasing P_{SO_2} from 6.4×10^{-3} to 4.8×10^{-2} atm, sulfur in the calcine is increased from 0.04 to 0.14%. It is worth reiterating that higher P_{SO_2} indicates a higher concentration of sulfur in the fuel. The %S in the calcine was significantly lower than the values predicted by thermodynamic analysis due to kinetics limitations. As can be seen in Figure 6.8, increasing P_{SO_2} causes a decrease in sulfur deportation percentage. Since the total gas flow rate was kept constant while changing P_{SO_2} , increasing P_{SO_2} led to a higher SO_2 flow rate. The decline in sulfur deportation percentage is attributed to the higher velocity of SO_2 , which results in its lower residence time in the furnace [124]. By increasing the velocity of SO_2 , the sulfur-containing gas departs faster from the furnace, hence hinders the transfer of sulfur from gas to solid. As P_{SO_2} increases from 6.4×10^{-3} to 4.8×10^{-2} atm, sulfur deportation percentage decreases from 34.3 to 17.3%. Considering that the sulfur originated from coal is distributed between the calcine and the off-gas, the above observation demonstrates that the percentage of sulfur that reports to the off-gas increases with increasing the sulfur content of coal.

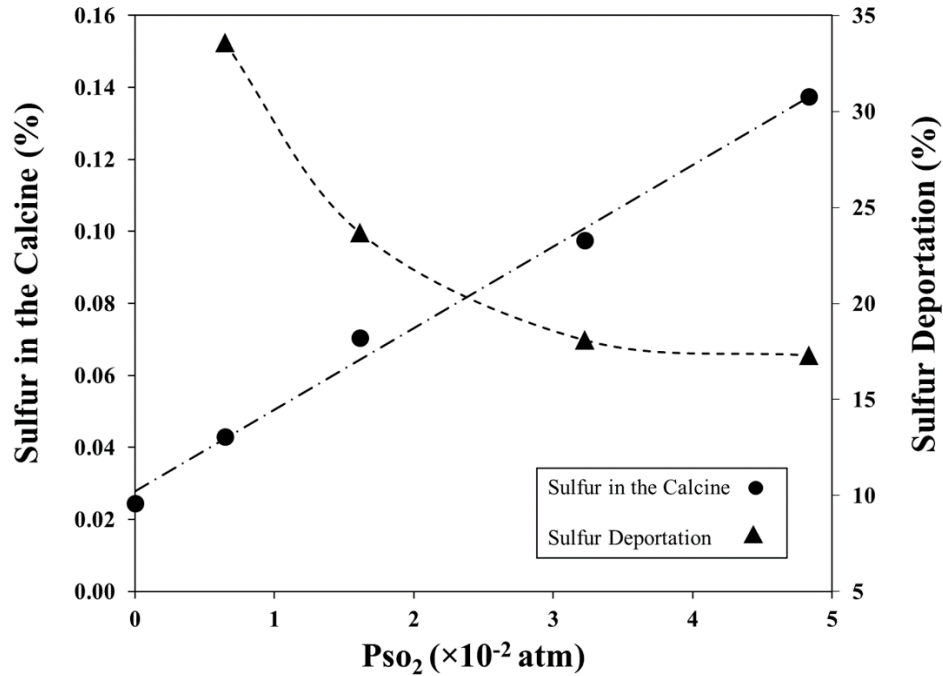


Figure 6.8 The effect of the P_{SO_2} on the % S in the calcine and sulfur deportation percentage at 900 °C, CO/CO₂ of 4, 60 min processing time, and the gas flow rate of 57.3 ml/min.

Figure 6.9 shows the XRD patterns of the samples processed at different P_{SO_2} . The main crystalline phases are described in section 4.2. The pyrrhotite peak was observed for samples S3 and S5 which were treated in an atmosphere containing 1.6 and 4.8% SO₂, respectively.

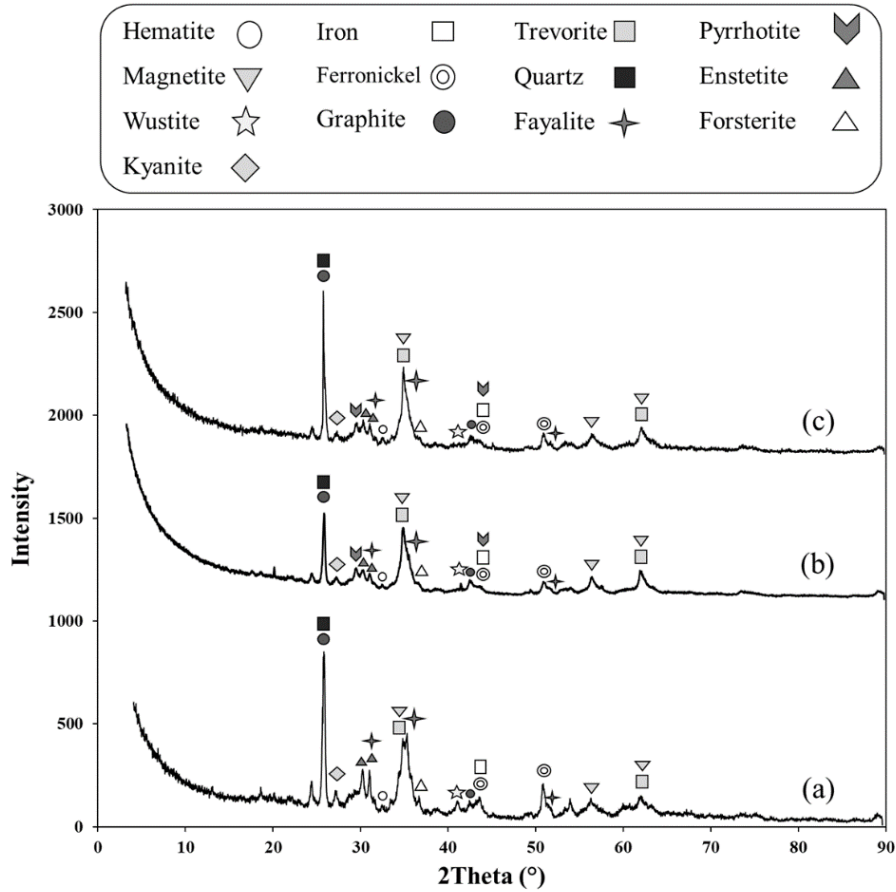


Figure 6.9 XRD patterns for samples (a) S1, (b) S3, and (c) S5.

6.3.3 The Effect of the Reducing Atmosphere (CO/CO₂)

Figure 6.10 depicts the effect of the reducing atmosphere on the S content of the calcine and sulfur deportation. The aggressive reducing condition results in higher S content of the calcine and higher sulfur deportation. By increasing CO/CO₂ from 0.5 to 10, the sulfur content of the calcine increases from 0.056 to 0.082%. Under the same conditions, sulfur deportment percentage rises from 18.95 to 25.12%. In industrial plants, CO/CO₂ in the rotary kiln is controlled by adjusting the relative quantity of fuel and air.

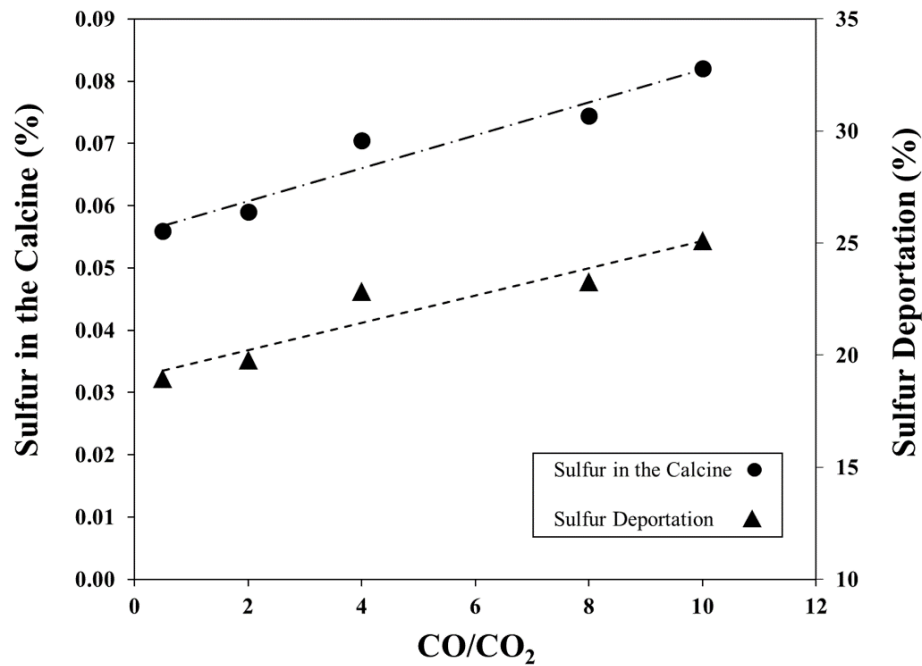


Figure 6.10 The effect of CO/CO₂ on the % S in the calcine and sulfur deportation percentage at 900 °C, 5% S in burning coal ($P_{SO_2} = 0.016$ atm), 60 min processing time, and gas flow rate of 57.3 ml/min.

The effect of the reducing atmosphere on the composition of the calcine was investigated using XRD analysis on samples C1, C3, and C4 with various CO/CO₂. The CO/CO₂ for these three samples are 0.5, 4, and 8, respectively. The XRD results are shown in Figure 6.11, metallic iron and ferronickel are not present in the sample processed in CO/CO₂ of 0.5. However, by enhancing the reducing condition, the intensity of fayalite, metallic iron, and ferronickel peaks increase while there is a decrease in the intensity of magnetite and hematite peaks. Pyrrhotite as a main sulfur-containing compound was also identified in the XRD patterns of samples C3 and C4.

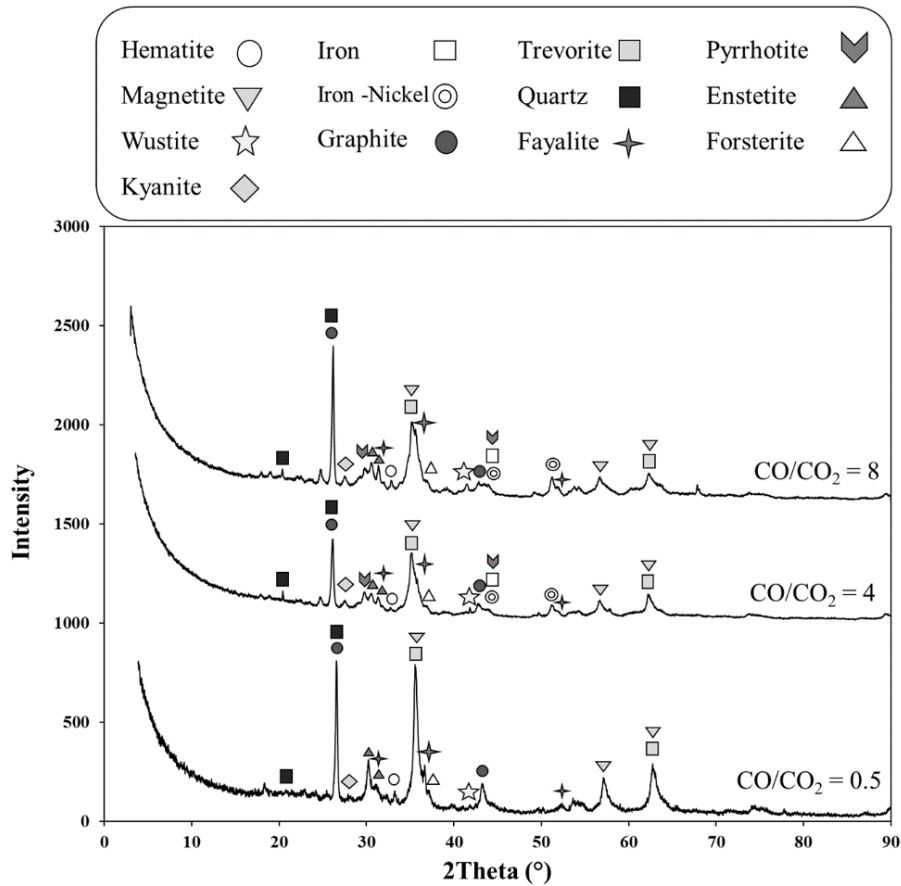


Figure 6.11 X-ray diffraction patterns of samples C1, C3, and C4 prepared in various reducing atmospheres.

6.3.4 The Effect of the Total Gas Flow Rate

The CO to CO₂ ratio was set at 4 for all samples processed at different gas flow rates. This ratio was chosen based on the observation of the desired reduction behavior in the previous set of experiments presented in section 6.3.3. Changes in the gas flow rate were made by adjusting the flow rate of each gaseous species while maintaining their partial pressure. The increase in the gas flow rate in these experiments is equivalent to using higher amount of fuel per unit mass of the laterite ore. As mentioned in section 4.4.2, the gas flow rate is associated with the molar ratio of carbon in the coal to the sum of Fe₂O₃ and NiO content of the raw ore. The values of 0.5 and 4 for

C/(Fe₂O₃+NiO) are equivalent to 28.5 and 229.2 ml/min of the total gas flow rate, respectively. Variation of % S in the calcine with the gas flow rate is shown in Figure 6.12. The sulfur content in the calcine continuously increases by increasing the gas flow rate and reaches 0.25% at the gas flow rate of 229.2 ml/min. The percentage of sulfur deportation to the calcine decreased slightly by increasing the gas flow rate (Figure 6.12). This observation can be explained by higher gas velocity and thus lower residence time of SO₂ in the system.

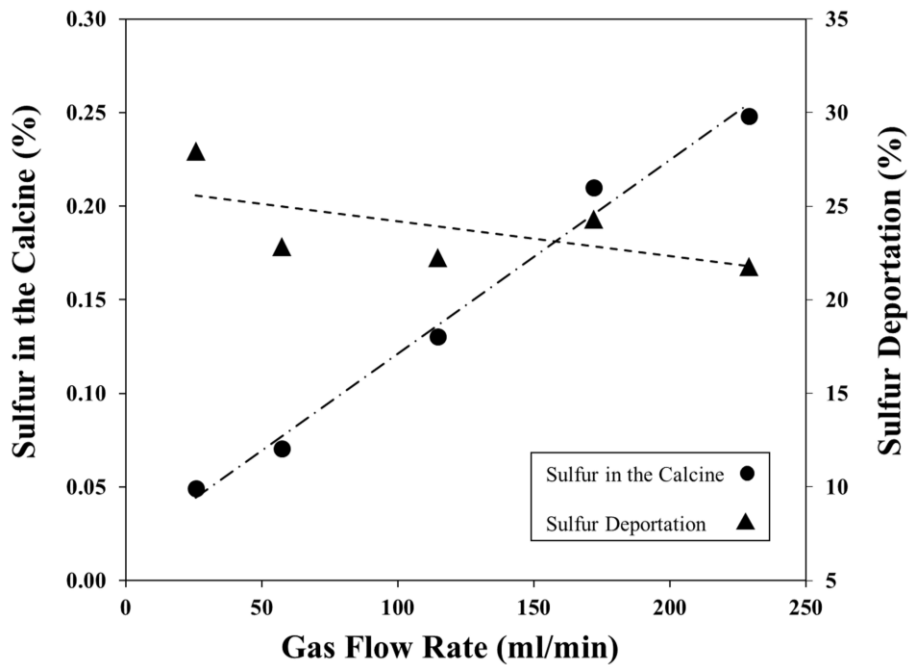


Figure 6.12 The effect of the gas flow rate on the % S in the calcine and sulfur deportation percentage at 900 °C, 5% S in burning coal ($P_{SO_2} = 0.016$ atm), 60 min processing time, and CO/CO₂ of 4.

The XRD patterns of the samples processed at various gas flow rates are presented in Figure 6.13. The intensity of ferronickel and fayalite peaks is increased by purging higher gas flow rates. This implies a higher degree of reduction at higher gas flow rates. Pyrrhotite peak as the main sulfur-containing compound is visible in samples F2, F3, and F5.

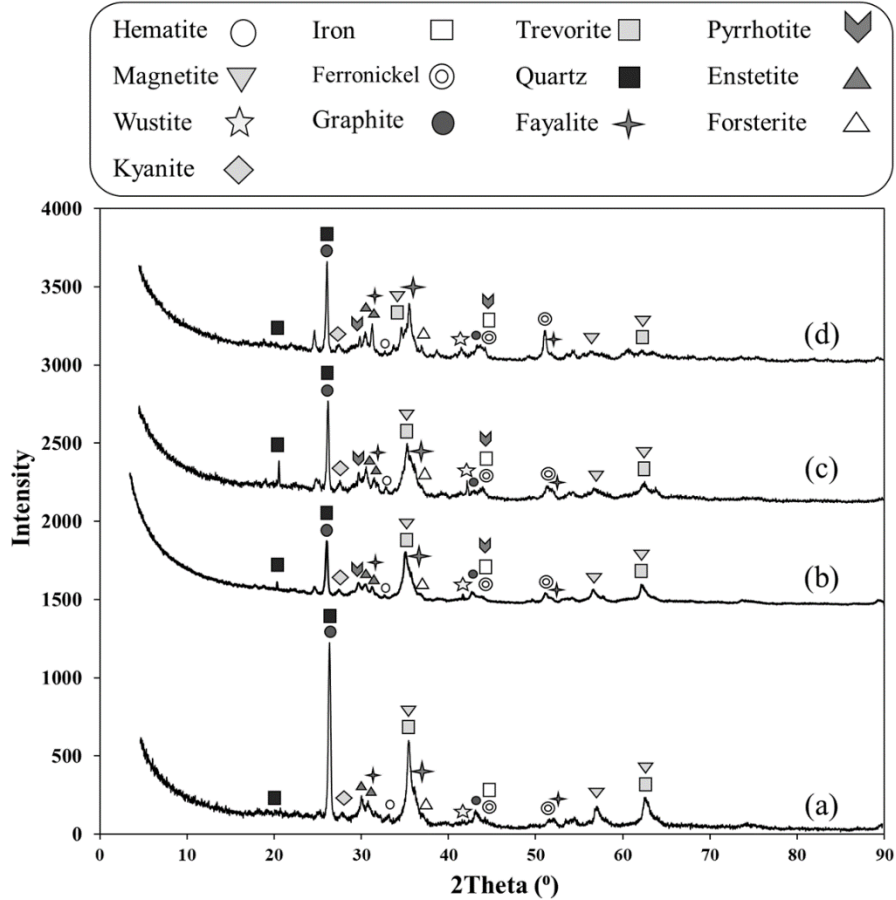


Figure 6.13 X-ray diffraction patterns of samples (a) F1, (b) F2, (c) F3, and (d) F5.

6.3.5 The Effect of Temperature

The variation of the %S in the calcine and sulfur deportation percentage as a function of temperature are shown in Figure 6.14. Increasing the temperature from 600 to 700 °C resulted in higher %S in the calcine. However, increasing the temperature above 700 °C causes a decrease in %S in the calcine. The same behavior was observed for sulfur deportation. According to both thermodynamics and kinetics considerations, increasing temperature is expected to yield a higher %S in the calcine. The decrease in %S above 700 °C is attributed to surface area reduction because of sintering of the particles and recrystallization of magnesia silicates [74, 75]. Recrystallization of magnesia silicates which occur at 800-820 °C, results in a significant decrease in the surface

area of the solid [74, 75]. The recrystallization mechanism is initiated by prenucleation step in which the amorphous grains start to undergo a structural change. Short-range order is changed to long-range crystallographic order at the surface. Subsequently, crystallization is occurred at the surface and progressed toward the center of the grain [125]. The smaller surface area of the solid results in the slower reaction kinetics between the gas and the solid, which in turn impedes sulfur transfer from the gas to the calcine.

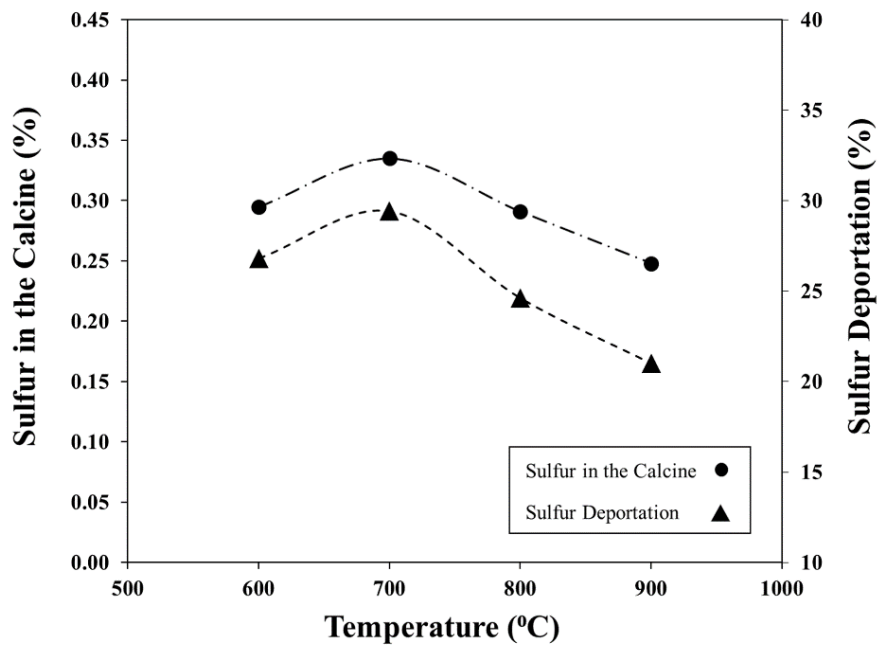


Figure 6.14 The effect of temperature on the %S in the calcine and sulfur deportation percentage at 5% S in burning coal ($P_{SO_2} = 0.016$ atm), CO/CO₂ of 4, 60 min processing time, and the gas flow rate of 229.2 ml/min.

Figure 6.15 shows the XRD spectra of the samples calcined at various temperatures. Increasing temperature enhances the reduction reactions and hence the formation of ferronickel and fayalite. It is worth noting that when nickel oxide is incorporated in the forsterite crystal, it will be locked up in an olivine structure. This will hinder the reduction of nickel oxide [73, 75, 76].

According to the results shown in Figure 6.15, both enstatite and forsterite are formed during calcination. The type of crystalline magnesia silicate compound at high temperatures depends on MO to SiO₂ ratio in the raw ore where MO is the divalent metal oxides in the ore [75, 77]. The MO/SiO₂ of greater than 1.5 indicates the formation of forsterite. The ore used in this study has the MO/SiO₂ of 0.4, which implies the formation of higher amounts of enstatite compared with forsterite. The reducibility of nickel oxide in enstatite structure is easier than forsterite [73, 76, 78, 79]. Hence, the effect of temperature increase from 800 to 900 °C on the reducibility of nickel oxide is expected to be insignificant. This is in agreement with the results of the XRD spectra for samples T3 and T4.

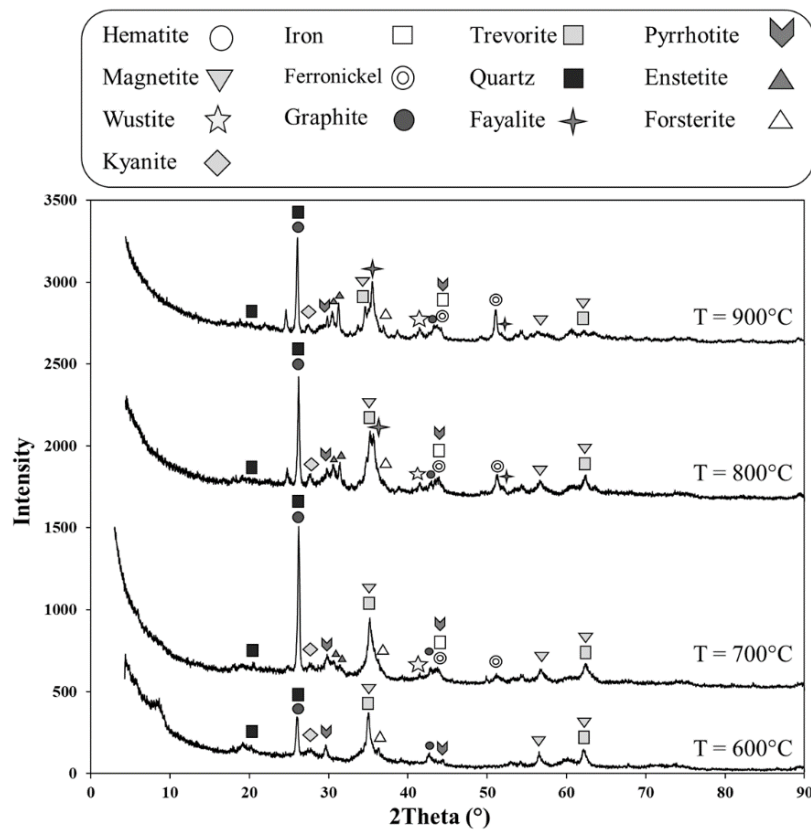


Figure 6.15 X-ray diffraction patterns of samples prepared at various temperatures, i.e., T1-T4.

It is worth mentioning that the percentage of sulfur deportation calculated from the experimental results and the ones from thermodynamic simulations are in the range of 17.26-34.35% and 99.93-99.99%, respectively. The variation is caused by the non-equilibrium nature of the experiments.

6.4 Conclusion

Considering the XRD and thermodynamic analyses results, pyrrhotite (Fe_7S_8) is identified as the main sulfur-bearing compound in the calcine. The effects of different parameters including the P_{SO_2} resulted from coal combustion, the reducing atmosphere in the furnace, gas flow rate, and temperature on sulfurization behavior and composition of the calcine are studied. It is concluded that increasing the sulfur content of the fuel, improving the reducing atmosphere, and increasing the fuel consumption result in higher sulfur content in the calcine. Increasing the fuel consumption results in a slight decrease in the percentage of sulfur deportation due to the shorter residence time of the gas in the furnace. Increasing temperature from 600 to 700 °C leads to higher sulfur in the calcine and increases sulfur deportation from the gas phase to the solid; however, raising the temperature above 700 °C decreases the sulfur deportation percentage due to the sintering of particles as well as recrystallization of the silicate compounds.

Chapter 7: Kinetic Analysis on the Sulfur Deportation during the Calcination Process

7.1 Introduction

In the previous chapter, sulfurization reactions were identified, and the effect of the operational parameters on the sulfur content of the calcine were examined. Investigating sulfur deportation at different processing times is essential to examine the kinetics of the sulfurization reactions. This chapter aims at investigating the effect of temperature and P_{SO_2} on the sulfur content of the calcine at different processing times in the range of 15-120 min. The activation energy (E) of the sulfurization reaction is obtained by combining model-free and model-fitting approaches. According to the activation energy values obtained by the model-free method, the process is divided into two steps, and the appropriate kinetic model for each step was selected based on the results of the model-free, model-fitting, and master plot methods.

The next section of this chapter investigates the effect of P_{SO_2} on the kinetics of the sulfurization reactions. The pressure kinetic function is calculated based on the sulfur content of the calcine processed at three values of P_{SO_2} (6.4×10^{-3} , 1.6×10^{-2} , and 2.6×10^{-2} atm). For each value of P_{SO_2} , eight samples with different processing times in the range of 15-120 min were prepared. The order of reaction was calculated with respect to P_{SO_2} .

7.2 Kinetic Parameters and the Kinetic Model of the Sulfur Deportation during Calcination Stage

This section investigates the kinetics of the sulfurization process using three different methods, namely model-free, model fitting and master plot techniques. Kinetics of the sulfur deportation is examined based on the sulfur content of the calcine at different processing times. The sulfur

content of each sample was obtained by three times repetition of ICP analysis with the relative standard deviation in the range of 1.7-4.9%. Figure 7.1 illustrates the %S in the calcine versus processing time at 700, 800, and 900 °C. Sulfur content of the calcine is increased by processing time. As shown in Figure 7.1, increasing temperature results in a decrease in %S in the calcine at all processing times. As described in section 6.3.5, increasing temperature above 700 °C promotes sintering which results in a lower surface area of the solid in contact with the atmosphere. In addition, recrystallization of magnesia silicates at 800-820 °C leads to a decrease in the surface area and results in the slower kinetics of the gas-solid reactions and lower sulfur transfer from gas to the calcine. Polynomial equations are obtained to estimate %S at each temperature as a function of time. These equations which are presented in Table 7.1, are obtained based on the best regression functions fitted to the data points in Figure 7.1.

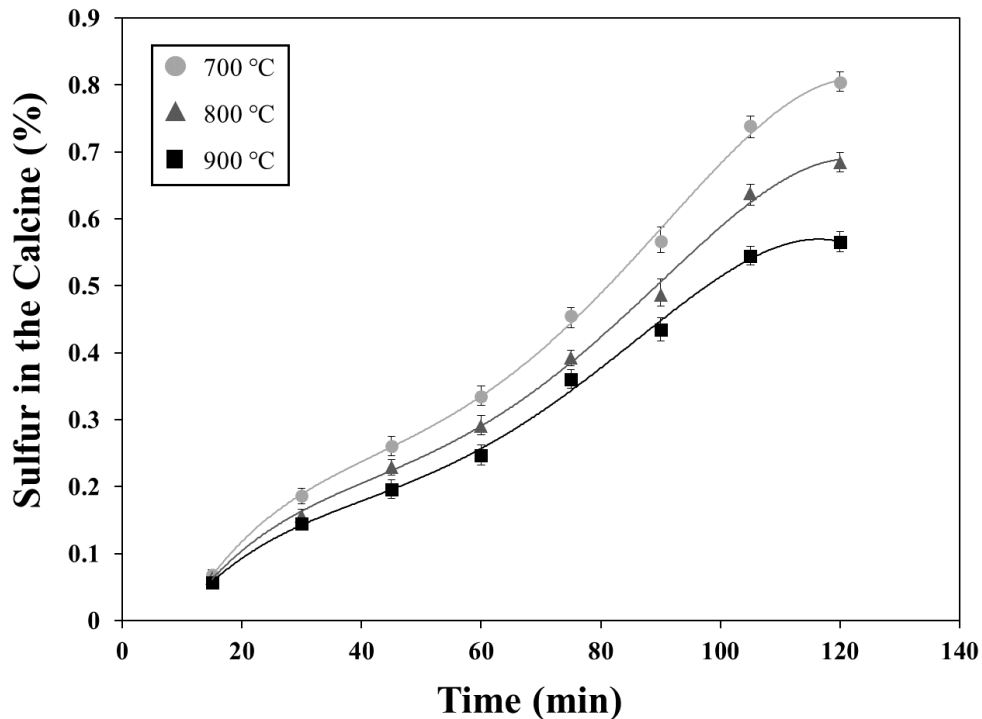


Figure 7.1 %S in the calcine vs. processing time for calcines processed at 700, 800, and 900 °C with constant parameters of 5% S in burning coal ($P_{SO_2} = 0.016$ atm) and the gas flow rate of 229.2 ml/min.

Table 7.1 Equations for sulfur content in the calcine (%) vs. time (min) at 700, 800, and 900 °C.

Equation	R ²
$\%S_{700\text{ }^{\circ}\text{C}} = -2.22 \times 10^{-8} t^4 + 6.1 \times 10^{-6} t^3 - 5.45 \times 10^{-4} t^2 + 2.44 \times 10^{-2} t - 1.96 \times 10^{-1}$	0.9941
$\%S_{800\text{ }^{\circ}\text{C}} = -1.93 \times 10^{-8} t^4 + 5.18 \times 10^{-6} t^3 - 4.54 \times 10^{-4} t^2 + 2.01 \times 10^{-2} t - 1.55 \times 10^{-1}$	0.9958
$\%S_{900\text{ }^{\circ}\text{C}} = -1.94 \times 10^{-8} t^4 + 4.9 \times 10^{-6} t^3 - 4.03 \times 10^{-4} t^2 + 1.71 \times 10^{-2} t - 1.23 \times 10^{-1}$	0.9976

To perform kinetic analysis, the extent of reaction (α) was calculated according to equation 7.1 [126]:

$$\alpha = \frac{S - S_i}{S_f - S_i} \quad (7.1)$$

where S is the sulfur content of the calcine at time t, S_i is the initial sulfur content of the raw ore, and S_f is the final sulfur content of the calcine. The extent of reaction varies between 0 to 1. The α values of 0 and 1 correspond to the beginning and the end of the reaction, respectively. The extent of reaction is calculated based on the %S in the calcine shown in Figure 7.1. Figure 7.2 shows the extent of the reaction versus time for the samples processed at 700, 800, and 900 °C.

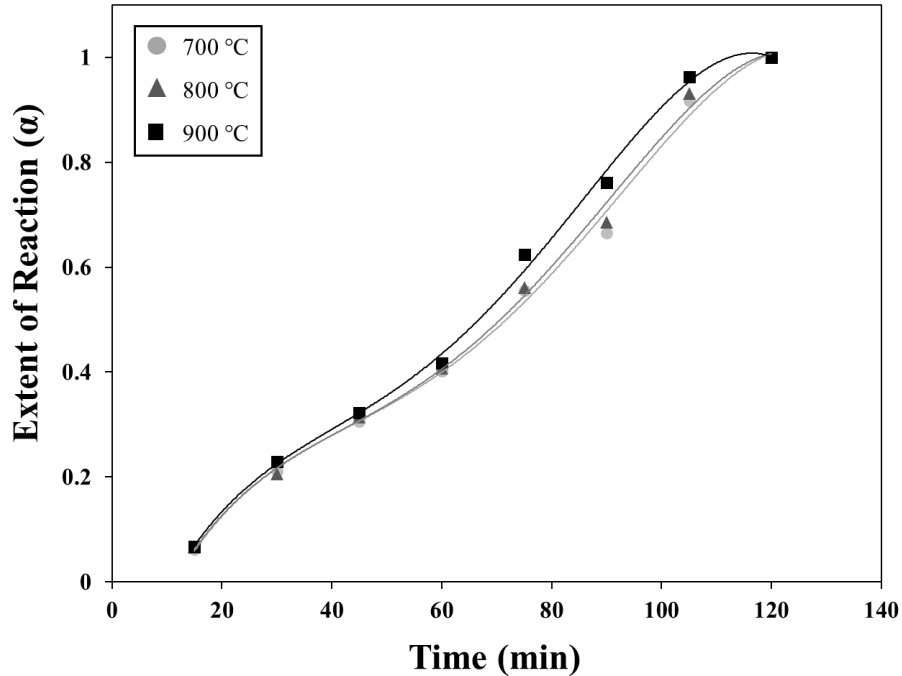


Figure 7.2 Extent of reaction vs. time for samples processed at 700, 800, and 900 °C with constant parameters of 5% S in burning coal ($P_{SO_2} = 0.016$ atm) and the gas flow rate of 229.2 ml/min.

The general expression for gas-solid reactions is presented in equation 7.2 [83, 99, 127]:

$$\frac{d\alpha}{dt} = f(\alpha)k(T)h(P) \quad (7.2)$$

where $f(\alpha)$, $k(T)$, and $h(P)$ are functions of the extent of reaction, temperature, and pressure, respectively. The dependence of the process rate on the extent of reaction is parameterized through the reaction model $f(\alpha)$. The temperature function is generally presented by the Arrhenius equation, as explained in chapter 5.

This section presents the kinetic analysis for calculating activation energy (E) and identifying the best kinetic model for sulfur deportation at the constant P_{SO_2} . The effect of P_{SO_2} on the kinetics of the sulfurization reactions is investigated and presented in section 7.3. Similar to the kinetic

analysis presented in chapter 5, Equation 7.3 is obtained by inserting the Arrhenius function in equation 7.2 at a constant P_{SO_2} .

$$\frac{d\alpha}{dt} = A \exp\left(\frac{-E}{RT}\right) f(\alpha) \quad (7.3)$$

The integral form of the reaction model, $g(\alpha)$, is obtained by rearranging equation 7.3 as follows [83,128]:

$$g(\alpha) = \int_0^\alpha \frac{d\alpha}{f(\alpha)} = A \exp\left(\frac{-E}{RT}\right) t \quad (7.4)$$

The activation energy is estimated using two main approaches: model-free and model fitting. These methods are described in detail in the following sections.

7.2.1 Model-Free Method

Model-free method is employed to calculate E as a function of α without any assumption about a reaction model. A significant change in E values at various times of the process implies a change in the reaction mechanism. Therefore, various steps of a complex process can be identified by calculating E using model-free method [128, 129]. Two common model-free methods known as integral and differential isoconversional methods are used to calculate E versus α .

The equation of the integral isoconversional method is obtained by taking the logarithm and rearranging the equation 7.4 as follows [83, 130]:

$$-\ln t = \ln\left(\frac{A}{g(\alpha)}\right) - \frac{E}{RT} \quad (7.5)$$

The activation energy for each extent of reaction is obtained by calculating the slope of the regression line for $-\ln t$ versus $1/T$. Figure 7.3 shows $-\ln t$ versus $1/T$ for various extents of reactions based on the integral isoconversional method.

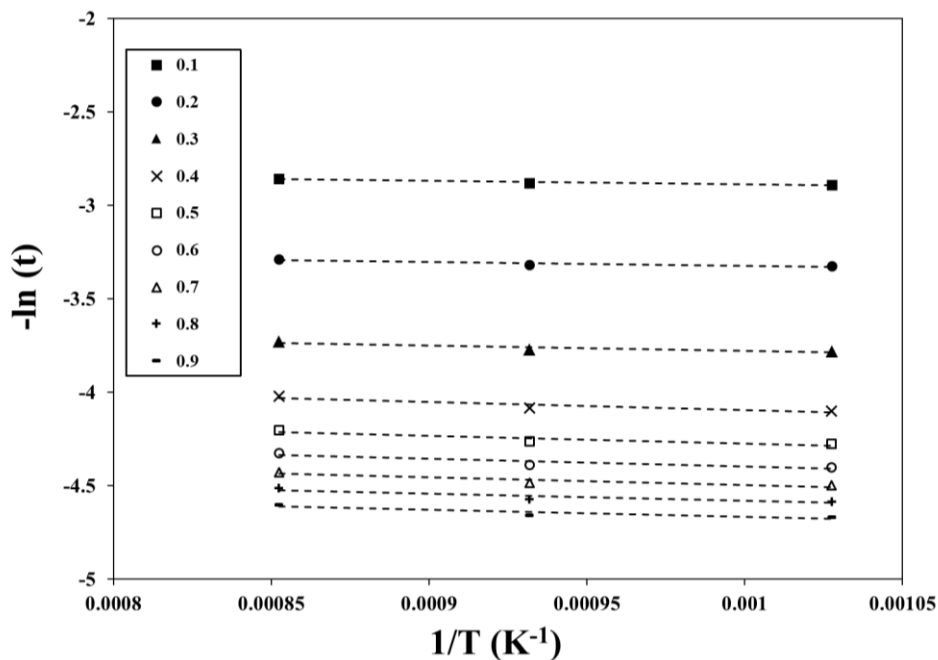


Figure 7.3 The regression lines for various extents of reaction based on the integral isoconversional method.

The next common model-free method is the differential isoconversional route. Equation 7.6 is the main model for this method which is derived by taking the natural logarithm of equation 7.3.

$$\ln\left(\frac{d\alpha}{dt}\right) = \ln[f(\alpha)A] - \frac{E}{RT} \quad (7.6)$$

Based on the α values obtained from sulfur deportation at 700, 800, and 900 °C (Figure 7.2), the values of $\frac{d\alpha}{dt}$ and $\ln\left(\frac{d\alpha}{dt}\right)$ versus time are calculated and shown in Figure 7.4. The activation energy for each α value is determined from the slope of $\ln\left(\frac{d\alpha}{dt}\right)$ versus $1/T$. Figure 7.5 presents the change in $\ln\left(\frac{d\alpha}{dt}\right)$ versus $1/T$ for various extents of reaction using the differential isoconversional

method. The activation energy values relative to the extent of reaction calculated by integral and differential isoconversional methods are shown in Figure 7.6. The activation energy increases by progressing the reaction to α of 0.4; the activation energy decreases with a further increase of α . Considering the change in the activation energy value, the process is divided into two steps before and after α of 0.4.

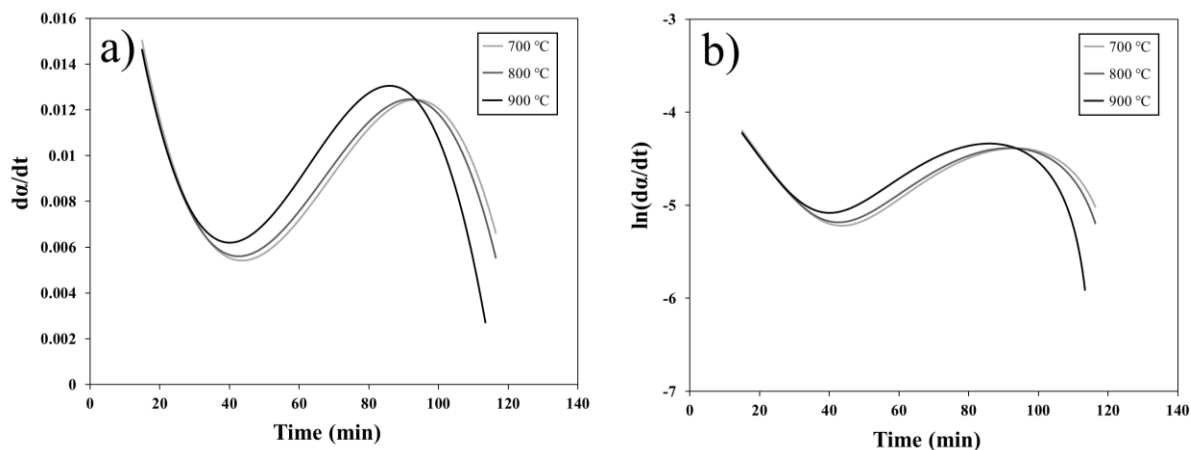


Figure 7.4 (a) The plots of $\frac{d\alpha}{dt}$ vs. time and (b) $\ln\left(\frac{d\alpha}{dt}\right)$ vs. time.

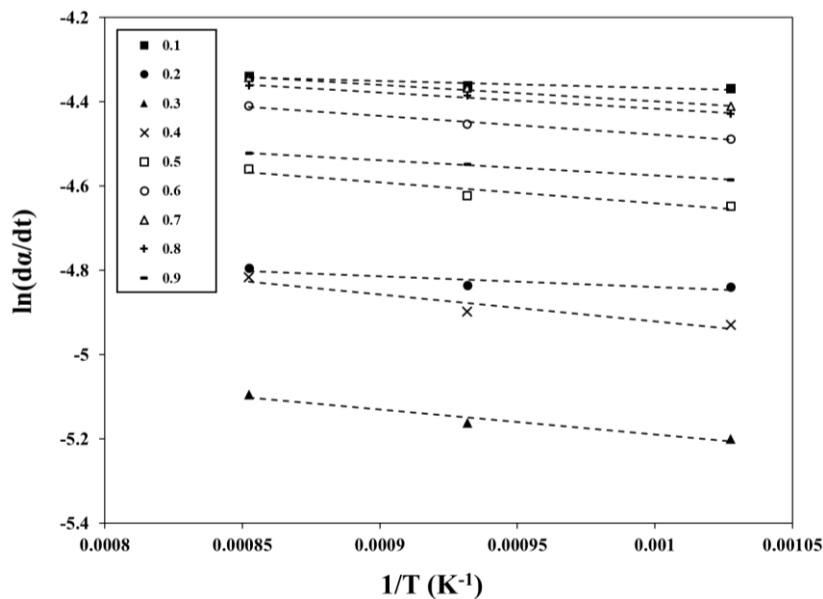


Figure 7.5 The regression lines for various extents of reaction based on the differential isoconversional method.

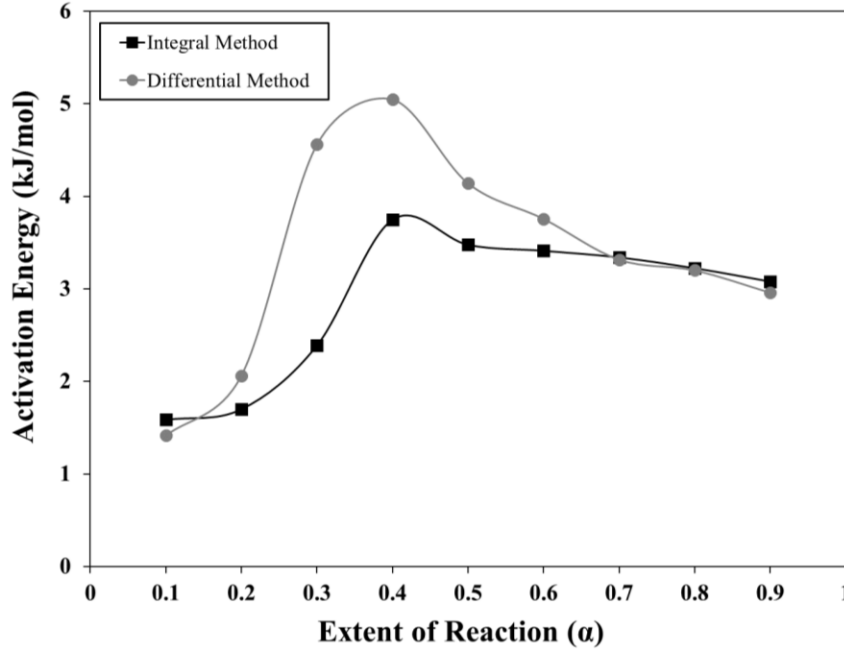


Figure 7.6 Activation energy as a function of the extent of reaction obtained from integral and differential isoconversional methods.

7.2.2 Model Fitting Method

The kinetic parameters and the associated model for the sulfurization process are obtained by model-fitting method. Since the activation energy values obtained by model-free methods (Figure 7.6) vary at different α values, a single reaction model does not describe the process adequately. Therefore, the process is divided into two steps before and after α of 0.4.

Based on equation 7.4, the slope of the regression line fitted to $g(\alpha)$ versus t is equal to $K = A \exp\left(\frac{-E}{RT}\right)$. The obtained K values are used to determine E via calculating the slope of $\ln(K)$ versus $1/T$. The kinetic functions used for model-fitting calculations are presented in Table 5.2. The range of the activation energy is initially obtained by model-free method to avoid enforcing a hypothetical kinetic model on the experimental data. In short, the activation energy values are initially calculated using model-free approach (section 7.2.1). Then, the experimental data for the

extent of reaction are fitted to all the kinetic functions listed in Table 5.2. The kinetic functions which yield an activation energy value in the range of the one predicted by model-free method are selected as the viable kinetic models. The final kinetic model is chosen from the previously selected models based on the maximum coefficient of determination.

In order to obtain the activation energy by model-fitting approach, the process was divided into two steps at 60 minutes of processing time which is equivalent of $\alpha \sim 0.4$. The extent of reaction was calculated for each step based on the experimental data. Since $\alpha = 1$ leads to the infinite value for some kinetic functions, the model-fitting calculations were carried out for $\alpha < 1$. The Activation energy values of the two steps of the process were calculated for all the kinetic models listed in Table 5.2. The selected kinetic models for which the activation energy values fall within the range obtained by model-free method are presented in Table 7.2. The kinetic models with the highest coefficient of determination are selected as the kinetic model for each step. The contracting sphere (C3) and Avrami-Erofeev (A3) are selected as the kinetic models for steps 1 and 2, respectively. These models are chosen due to the similarity between the activation energy values calculated from model-free and model-fitting approaches and the high value of the coefficient of determination.

Table 7.2 Selected kinetic models for steps 1 and 2 of the sulfurization process.

Code	E (kJ/mol)	R ²
Step 1		
C2	1.78	0.9839
C3	2.41	0.9961
D2	1.89	0.9817
D3	2.67	0.9777
R1	1.54	0.9891
R2	3.35	0.9799
Step 2		
D1	4.69	0.9884
A3	3.85	0.9944

The details of model-fitting calculations for the selected kinetic models, i.e., contracting sphere (C3) for the first step and (b) Avrami-Erofeev (A3) for the second step, are shown in Figure 7.7 and Figure 7.8. The slope of $g(\alpha)$ versus time was calculated. The values obtained for the slopes are plotted as $\ln(K)$ versus $1/T$ to calculate the activation energy (Figure 7.8).

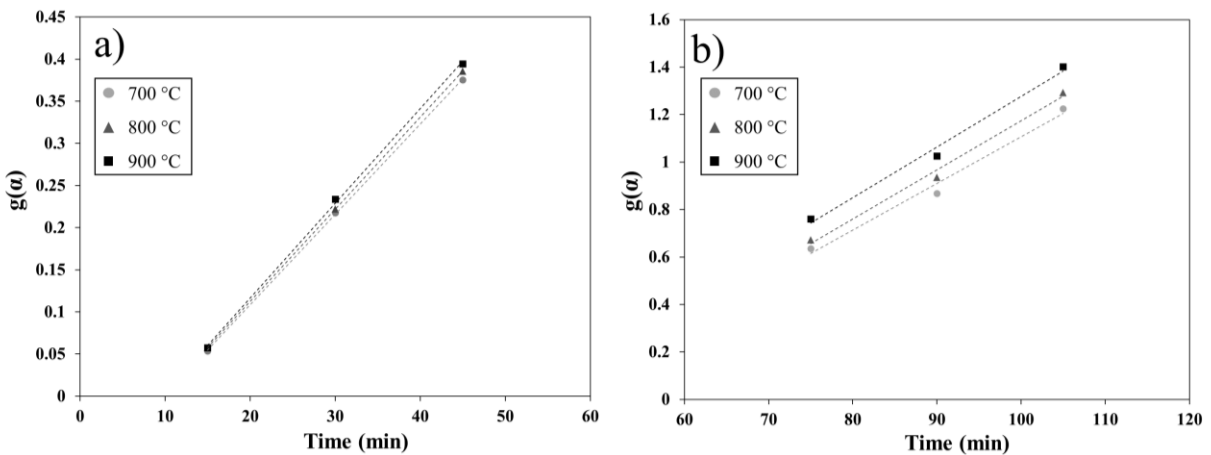


Figure 7.7 The kinetic function $g(\alpha)$ vs. time for the selected kinetic models at 700-900 °C. (a) Contracting sphere (C3) for the first step and (b) Avrami-Erofeev (A3) for the second step.

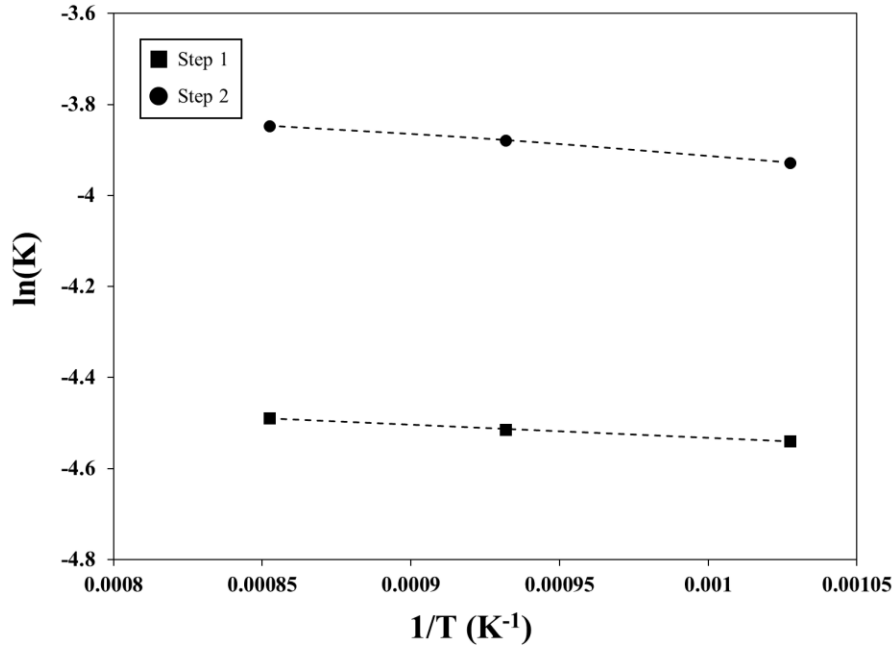


Figure 7.8 Dependence of $\ln(K)$ vs. $1/T$ for two steps of the process.

Based on the model-fitting and model-free results, the first step of the sulfurization process is described by the contracting sphere mechanism. In this model, nucleation can occur rapidly on the surface of the solid, and the reaction is progressed on the surface of the solid particle [131].

Iron sulfide is formed on the surface of the laterite particles by reactions between gaseous sulfur-containing species and iron oxides. The next step of the process is explained by Avrami-Erofeev mechanism, which is generally associated with nucleation and growth mechanism. The growth of iron sulfide nuclei occurs in this step. Also, ingestion and overlapping of the nucleation sites can occur during the growth process [131].

The activation energy value reveals important information regarding the reaction mechanism. A value lower than 24 kJ/mol generally indicates diffusion-controlled reactions [120, 121], while a value between 24 and 29 kJ/mol is commonly associated with the combined diffusion-controlled

and interfacial chemical reaction mechanism. Activation energy values above 29 kJ/mol corresponds to interfacial chemical reaction mechanism [132, 133]. Low values of activation energy (1.4-5.3 kJ/mol) indicate that sulfur deportation is a diffusion-controlled process. Formation of iron sulfide on the surface of laterite particles leads to diffusion of iron and sulfur in opposite directions in iron sulfide compound. Diffusion coefficient of iron in the temperature range of 700-950 °C ($3 \times 10^{-9} - 4.7 \times 10^{-8}$ cm²/sec) is three orders of magnitude higher than that of sulfur ($3.2 \times 10^{-12} - 6.4 \times 10^{-12}$ cm²/sec) in iron sulfide compound. Predominant ionic defects in iron sulfide are cation vacancies. This leads to a higher diffusion coefficient of iron compared to sulfur [134, 135]. Therefore, iron ions are believed to be the predominant diffusing species during the growth of the sulfide product.

It is worth mentioning that neglecting particle size distribution (PSD) may cause an error in selecting a suitable kinetic model in model-fitting approach. However, in this study, the reliable E values are obtained by model-free approach without imposing a specific kinetic model on the experimental data. This implies that there is no assumption on PSD in model-free approach. In the next step, the kinetic models are selected based on comparing the E values from model-free method with E values calculated in model-fitting approach. In addition, it is worth noting that the coefficient of variation (CV) of the PSD, which is the ratio of standard deviation to the mean particle size, is a critical value that affects the error of the model-fitting method. A kinetic model developed for a PSD with CV less than 0.5 [136] (CV < 0.3 in [137]) can be fairly used to predict experimental data without involving PSD in the models. Thus, since the CV value in this study is 0.5, the error in the results of the model-fitting approach is expected to be insignificant.

7.2.3 Master Plot Method

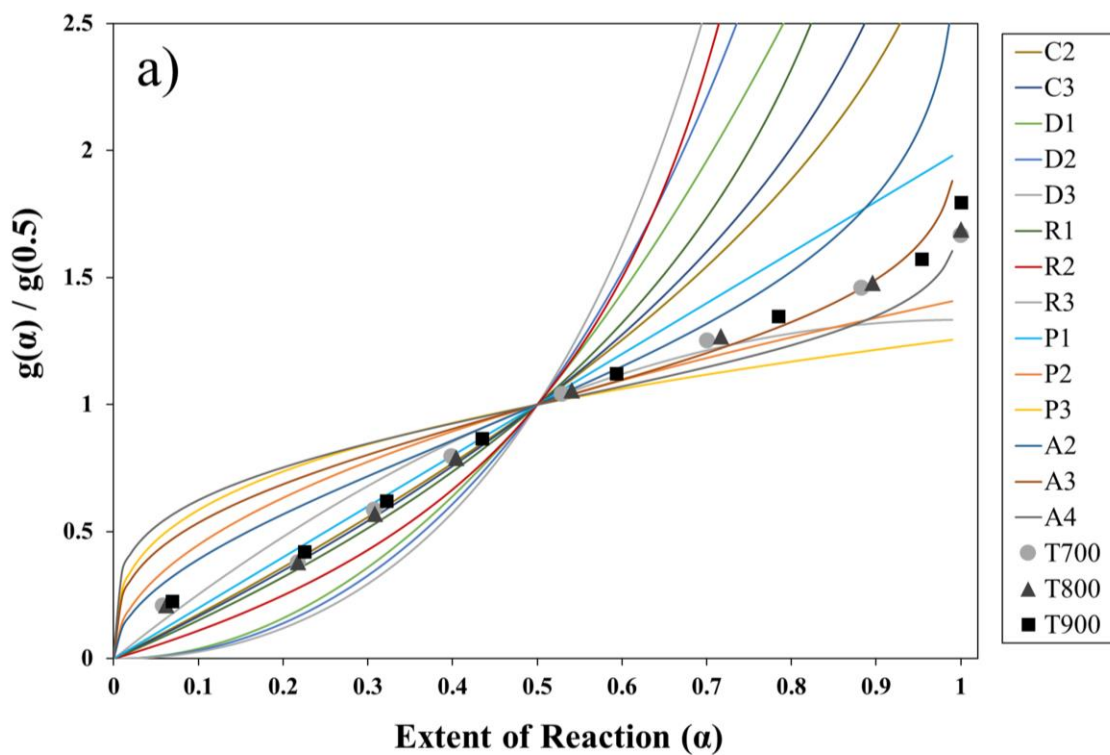
The master plot method is another technique for evaluating the reaction kinetics [138]. Master plot is a well-established mathematical method to identify the most suitable reaction model during the process without imposing the specific kinetic model on the experimental data [139]. The results of the master plot method are used for identifying the reaction model for each step of the process. Master plots, also known as reduced-time plots, are theoretical reference curves that depend on the kinetic model but are independent of the kinetic parameters. The experimental data are compared with the theoretical kinetic functions to identify the best model. This method is based on calculating the integral form of the kinetic equation using the experimental data at different values of α . The ratio of $g(\alpha)$ at any given α to $g(\alpha)$ at α equals to 0.5 is plotted versus α [139, 140].

The experiments are carried out in isothermal condition, therefore temperature functions offset each other [141–143]. Equation 7.7 is obtained by dividing $g(\alpha)$ in equation 7.4 by $g(\alpha)$ of the reference extent of reaction ($\alpha = 0.5$).

$$\frac{g(\alpha)}{g(\alpha_{0.5})} = \frac{t}{t_{0.5}} \quad (7.7)$$

Master plots of all the theoretical kinetic models along with the experimental data are shown in Figure 7.9 (a). The $\frac{t}{t_{0.5}}$ values are obtained by dividing the time for a given extent of reaction by the time of the reference extent of reaction. All the theoretical kinetic models are presented as $\frac{g(\alpha)}{g(\alpha_{0.5})}$. Therefore, by plotting $\frac{g(\alpha)}{g(\alpha_{0.5})}$ versus α , the experimental data can be compared with the theoretical kinetic models. The closest theoretical curve to the experimental data is selected as the kinetic model [144]. As shown in Figure 7.9 (b), the experimental data for the first step of the process, i.e., $0 < \alpha < 0.4$, lie on the contracting sphere kinetic model (C3) curve, and the data

points for the second step, i.e., $0.4 \leq \alpha < 1$, lie on the Avrami-Erofeev kinetic model (A3). The kinetic models predicted by the master plot method are in agreement with the model-fitting method presented in section 7.2.2.



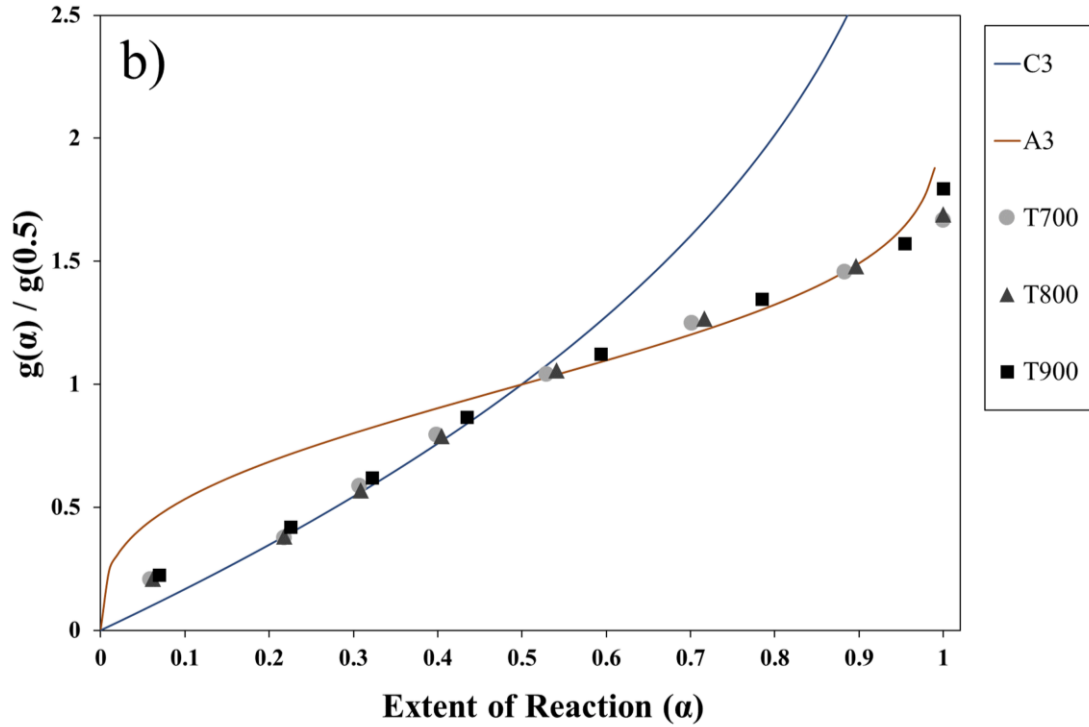


Figure 7.9 (a) Master plot for the theoretical kinetic models and the experimental data; (b) master plot of the selected kinetic models (C3 and A3) and experimental data.

7.3 The Effect of P_{SO_2} on the Kinetics of Sulfur Deportation

As described in equation 7.2, the comprehensive gas-solid reaction model includes three main functions of $f(\alpha)$, $k(T)$, and $h(P)$. The temperature effect is modelled using Arrhenius equation and extent of reaction (kinetic model) functions were discussed in section 7.2. In this section, the pressure function, $h(P)$, is examined by investigating the effect of P_{SO_2} on the kinetics of sulfur deportation at the calcination stage. The pressure function depends on P_{SO_2} as the main source of sulfur in the process. Generally, the pressure function is presented as a power function shown in equation 7.8 [99, 127]:

$$h(P) = (P_{SO_2} - P_{SO_2,eq})^n \quad (7.8)$$

P_{SO_2} and $P_{SO_2,eq}$ are the partial pressures of SO_2 in the system and at the equilibrium condition, respectively. n is the reaction order with respect to P_{SO_2} . By substituting $k(T)$ and $h(P)$ from equations 2.40 and 7.8 to equation 7.2, and using integral form of the reaction model, $g(\alpha)$, the comprehensive format of the kinetic equation is obtained as follows:

$$g(\alpha) = A \exp\left(\frac{-E}{RT}\right) (P_{SO_2} - P_{SO_2,eq})^n t \quad (7.9)$$

In order to calculate n , experimental values of α are converted to $g(\alpha)$ using the best kinetic model found in section 7.2. Then, $g(\alpha)$ is plotted against time to calculate the slope of the graph, which is equal to $A \exp\left(\frac{-E}{RT}\right) (P_{SO_2} - P_{SO_2,eq})^n$. Finally, n is obtained by calculating the slope of $\ln(P_{SO_2} - P_{SO_2,eq})$ versus $\ln[A \exp\left(\frac{-E}{RT}\right) (P_{SO_2} - P_{SO_2,eq})^n]$. The details for calculating the pressure function are described in this section.

The samples for these series of experiments were calcined at eight processing times in the range of 15-120 min and three different P_{SO_2} values of 6.4×10^{-3} , 1.6×10^{-2} , and 2.6×10^{-2} , which are equivalent to 2, 5, and 8% sulfur in the burning coal. The sulfur content of each sample was obtained by three repetitions of ICP analysis with the relative standard deviation in the range of 1.2-5.3%. According to Figure 7.10, the S content of the calcine increases by raising P_{SO_2} and the processing time. A polynomial regression equation is fitted to the S content of the calcine plotted versus processing time at different values of P_{SO_2} (Table 7.3).

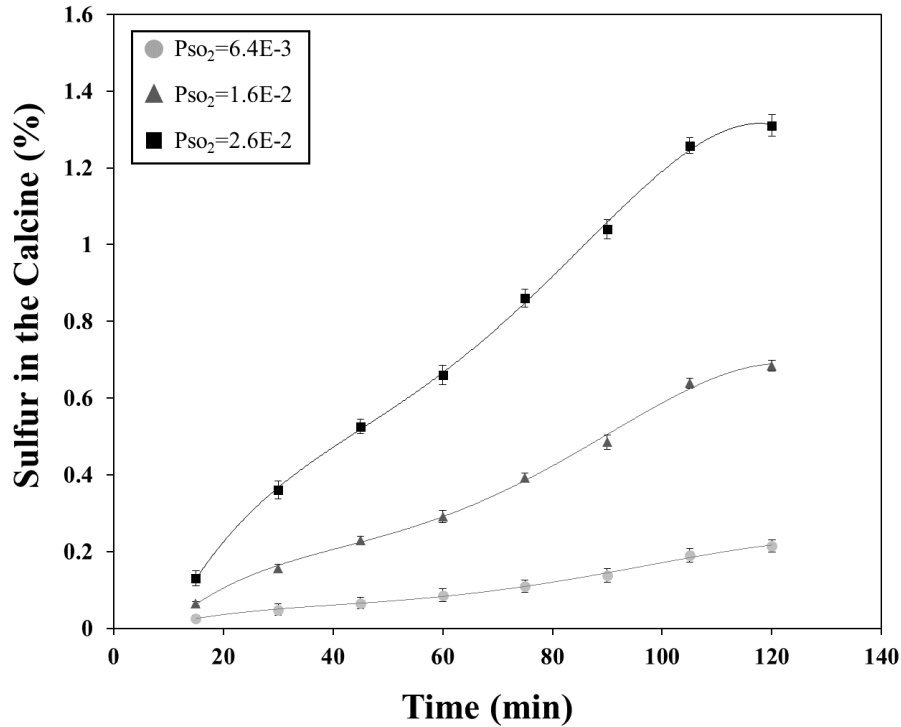


Figure 7.10 %S in the calcine vs. processing time for the calcines processed at 6.4×10^{-3} , 1.6×10^{-2} , and 2.6×10^{-2} atm SO_2 .

Table 7.3 Regression equations for sulfur content of the calcine (%) vs. time (min) at different values of P_{SO_2} .

P_{SO_2}	Equation	R^2
6.4E-3	$\%S = -4.66 \times 10^{-9} t^4 + 1.29 \times 10^{-6} t^3 - 1.11 \times 10^{-4} t^2 + 4.83 \times 10^{-3} t - 2.65 \times 10^{-2}$	0.9961
1.6E-2	$\%S = -1.93 \times 10^{-8} t^4 + 5.18 \times 10^{-6} t^3 - 4.54 \times 10^{-4} t^2 + 2.01 \times 10^{-2} t - 1.55 \times 10^{-1}$	0.9958
2.6E-3	$\%S = -3.69 \times 10^{-8} t^4 + 9.64 \times 10^{-6} t^3 - 8.53 \times 10^{-4} t^2 + 4.1 \times 10^{-2} t - 3.25 \times 10^{-1}$	0.9981

Considering the results of the kinetic analysis presented in section 7.2, the sulfur deportation process is divided into two steps at an approximate processing time of 60 min. The extent of the reaction for each step is calculated based on the experimental data, as shown in Figure 7.11.

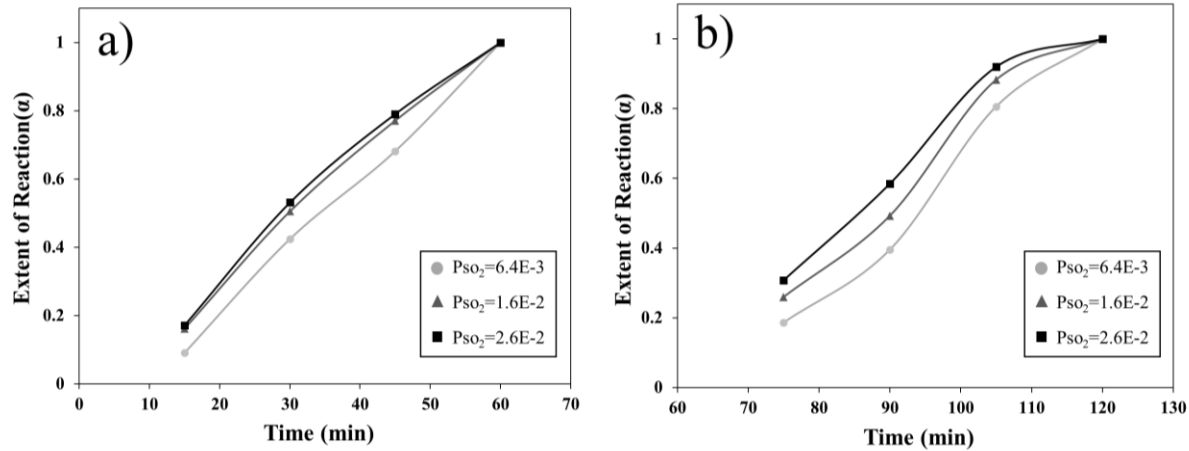


Figure 7.11 Extent of reaction vs. time for (a) step 1 (15-60 min) and (b) step 2 (75-120 min) of the sulfurization reaction.

Contracting sphere and Avrami-Erofeev kinetic models are selected as the reaction models for steps 1 and 2, respectively. The choice of the reaction models is based on the kinetic analysis performed in section 7.2. Using the above kinetic models, $g(\alpha)$ for each step is plotted against time (Figure 7.12). Since $\alpha=1$ leads to the infinite value for some kinetic functions, α values lower than one were considered for the present calculations.

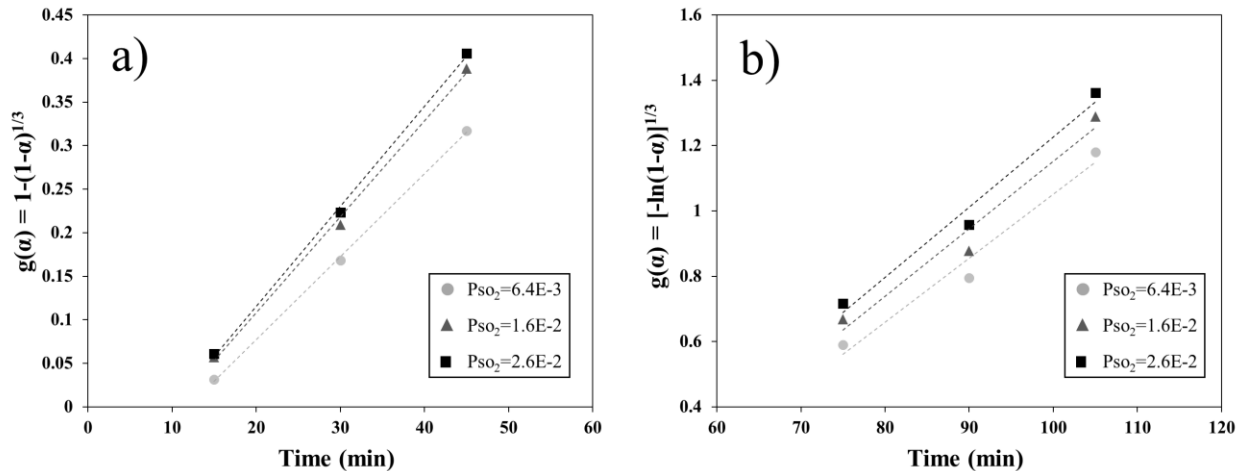


Figure 7.12 The value of $g(\alpha)$ of the best kinetic model vs. time for (a) step 1 (15-60 min) and (b) step 2 (75-120 min) of the sulfurization reaction.

As mentioned at the beginning of section 7.3, the slope of $g(\alpha)$ versus t equals $A \exp\left(\frac{-E}{RT}\right) (P_{SO_2} - P_{SO_2,eq})^n$. Since the experiments were carried out at 800 °C, the temperature function is written as constant K . Therefore, $K(P_{SO_2} - P_{SO_2,eq})^n$ is calculated from the slopes of the lines in Figure 7.12. The high-temperature experiments were carried out at three different values of P_{SO_2} . The $P_{SO_2,eq}$ for each P_{SO_2} in the gas mixture is calculated using the equilibrium module of HSC Chemistry 5.11. Table 7.4 presents the values of P_{SO_2} and $P_{SO_2,eq}$ used for kinetic calculations.

Table 7.4 The values of P_{SO_2} and $P_{SO_2,eq}$ used for kinetic calculations.

P_{SO_2}	$P_{SO_2,eq}$
6.4E-3	8.4E-9
1.6E-2	2.9E-8
2.6E-2	6.2E-8

$K(P_{SO_2} - P_{SO_2,eq})^n$ is obtained for two steps of the process from the slopes of graphs in Figure 7.12. Then, $\ln[K(P_{SO_2} - P_{SO_2,eq})^n]$ versus $\ln(P_{SO_2} - P_{SO_2,eq})$ is plotted for the two steps of the process, as shown in Figure 7.13. These values are presented in Table 7.5.

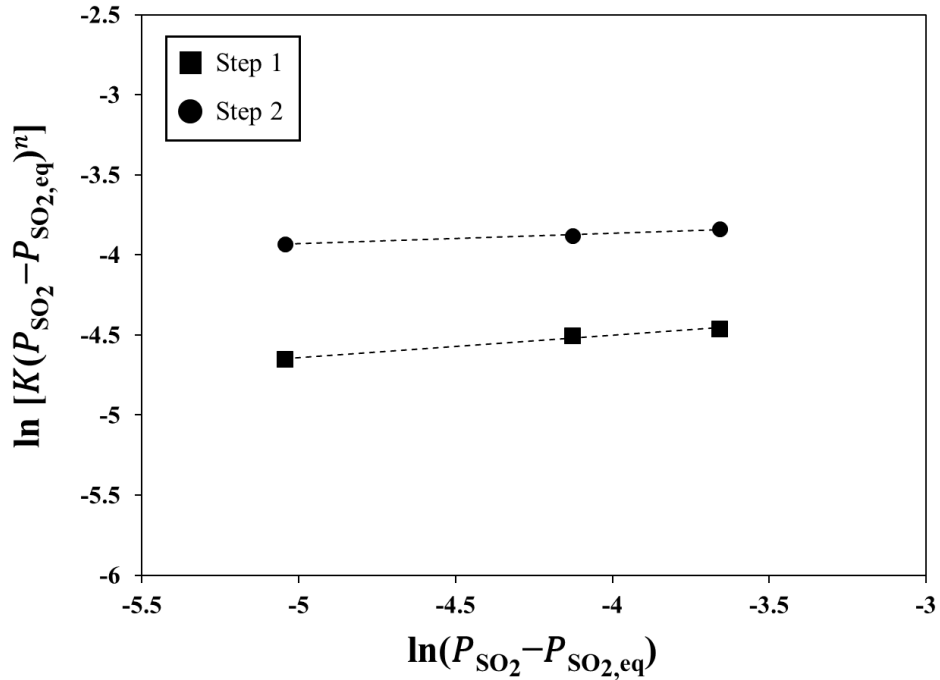


Figure 7.13 $\ln[K(P_{SO_2} - P_{SO_2,eq})^n]$ vs. $\ln(P_{SO_2} - P_{SO_2,eq})$ for the two steps of the process.

Table 7.5 Order of reaction values with respect to P_{SO_2} for the two steps of the process.

Step of the process	n
1	0.139
2	0.065

The small values of the order of reaction with respect to P_{SO_2} indicates that the variation of P_{SO_2} would not have a significant impact on the rate of reaction. It can be attributed to the very low amount of SO_2 purged to the system compared to the Fe content in the ore. The kinetic analysis and the order of reaction calculations were carried out for very low P_{SO_2} in the range of 6.4×10^{-3} to 2.6×10^{-2} . Basically, the available Fe as a reactant in sulfurization reactions is significantly

higher than the S content in the system. Therefore, changing P_{SO_2} would not considerably affect the rate of the sulfurization. Consequently, the reaction rate is relatively insensitive to P_{SO_2} .

7.4 Conclusion

The kinetics of sulfur deportation in nickel laterite calcination is investigated by a combination of model-free, model-fitting, and master plot methods. Considering the values of E obtained by model-free method, the process is divided into two steps before and after 60 minutes of calcination. The best kinetic models for steps 1 and 2 are identified as contracting sphere and Avrami-Erofeev, respectively. Since the E values of the sulfurization reactions are small (1.4-5.3 kJ/mol), it is inferred that the process is controlled by the diffusion of sulfur in the ore. The choice of the kinetic models of the two steps determined by the model-fitting method is confirmed by the master plot technique.

The effect of P_{SO_2} on the kinetics of the sulfurization process is also investigated. The results showed that the variation of P_{SO_2} would not have a significant impact on the rate of the reaction.

The following kinetic models are developed for two steps of the sulfur deportation process:

$$\frac{d\alpha}{dt} = A \exp\left(\frac{-E}{RT}\right) (3[1 - \alpha]^{\frac{2}{3}}) (P_{SO_2} - P_{SO_2,eq})^{0.139} \quad 0 < \alpha < 0.4 \quad (\text{step 1})$$

$$\frac{d\alpha}{dt} = A \exp\left(\frac{-E}{RT}\right) (3[1 - \alpha][-\ln(1 - \alpha)]^{\frac{2}{3}}) (P_{SO_2} - P_{SO_2,eq})^{0.065} \quad 0.4 \leq \alpha < 1 \quad (\text{step 2})$$

Where P_{SO_2} is in the range of 6.4×10^{-3} to 2.6×10^{-2} , which corresponds to 2-8% sulfur in the burning coal.

Chapter 8: Inhibition of Sulfur Transfer from the Fuel to the Calcine

8.1 Introduction

In the previous two chapters, sulfur deportment in the calcination stage and kinetics of sulfurization reactions were investigated. As mentioned in chapters 2 and 3, sulfur as an impurity deteriorates the mechanical properties of nickel alloys. Considering the negligible sulfur content of raw laterite ores, it is expected that the sulfur in crude ferronickel is originated from process additives such as rotary kiln fuel. Therefore, it is critical to implement an effective way to decrease the absorption of the sulfur by the calcine is to reduce the sulfur content of the crude ferronickel and diminish the load of the refinery. This chapter investigates the application of CaCO_3 as an absorbent of the sulfur resulted from fuel combustion (e.g., coal) in the calcination stage. Specifically, the effect of calcination time and temperature on preventing sulfur transfer to the calcine are examined. The sequence of the sulfurization reactions is determined, and the main sulfur-containing compound in the additive is identified by XRD, SEM-EDS, and thermodynamic analysis.

8.2 The Behavior of CaCO_3 as a Sulfur Absorbent in the Calcination Stage

To prevent the transfer of sulfur in the furnace atmosphere to the calcine, it is proposed to use a sulfur absorbent between the ore and the fuel burner where the sulfur-containing gases evolve. To the best of the author's knowledge, there is no previous investigation on mitigating the absorption of sulfur by nickel laterite calcine in the rotary kiln. Although the use of additives for sulfur absorption in laterite calcination has not been reported before, the injection of sorbents into the high-temperature zone (1000-1600 °C) of the coal fired boilers has shown to be effective in absorbing SO_2 resulted from coal combustion [145–147]. Typically, calcium based sorbents such as limestone (CaCO_3), dolomite ($(\text{CaMg}(\text{CO}_3)_2)$), hydrated lime ($\text{Ca}(\text{OH})_2$), and calcium oxide

(CaO) are used for this application [148–150]. In this study, CaCO₃ is selected as the sulfur absorbent in the calcination experiments since it is an abundant and inexpensive sulfur absorbent commonly used in various high-temperature refining processes [150–152]. As described in section 4.4.2, CaCO₃ powder was placed near one end of the furnace tube where the gas mixture of CO-CO₂-N₂-SO₂ entered the furnace. The gas mixture became in contact with the CaCO₃ powder before reacting with the laterite ore. In this chapter, the efficiency of CaCO₃ as the sulfur absorbent is investigated by thermodynamic analysis and high-temperature experiments.

8.2.1 Thermodynamic Analysis

Thermodynamic analysis was carried out to examine the feasibility of sulfur removal using CaCO₃ in the atmosphere resulted from coal combustion. Predominance area diagrams are used to predict the product of the sulfurization reaction. Predominance area diagrams provide critical information about the stability of the phases at different partial pressures of the gaseous species. Isothermal predominance area diagrams for Ca-S-C-O system at various P_{SO_2} and P_{CO}/P_{CO_2} values are shown in Figure 8.1. The diagram is plotted based on the equilibrium constant of the reactions in the system and experimental conditions pertaining to the current investigation, i.e., $P_{CO} + P_{CO_2} = 0.517$. Aggressive reducing atmosphere which is equivalent to higher P_{CO}/P_{CO_2} , promotes the formation of CaS. While lower P_{CO}/P_{CO_2} , results in CaSO₄ formation. The stability zones of CaCO₃ and CaO become larger by increasing temperature. Further increasing the temperature to 900 °C, promotes the decomposition of CaCO₃ to CaO. Considering the experimental conditions of the current investigation, i.e., $P_{SO_2} = 0.016$ atm and $\frac{P_{CO}}{P_{CO_2}} = 4$ (shown with plus signs in Figure 8.1), the main sulfur-bearing compound in the system at equilibrium conditions is CaS.

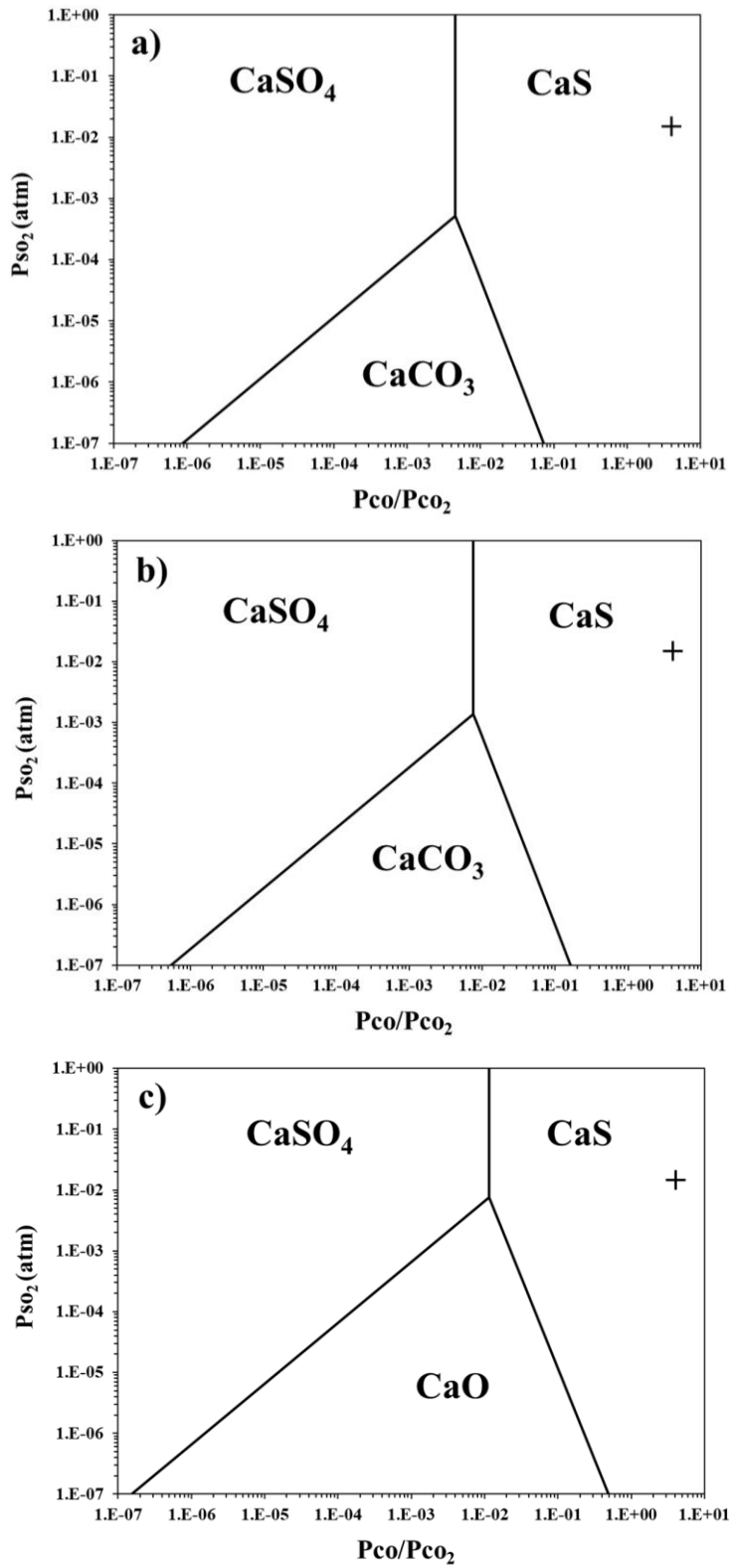


Figure 8.1 Predominance area diagrams for Ca-S-C-O system at (a) 700, (b) 800, and (c) 900 °C.

The equilibrium composition of the solids in the system containing CaCO_3 and the gas mixture used in this series of experiments is presented in Figure 8.2. The dominant sulfur-containing compound in the additive is CaS . In addition, CaCO_3 concentration decreases as temperature rises due to the decomposition of CaCO_3 to CaO . The thermodynamics results show that upon equilibrium, 99.94% of the sulfur in the atmosphere is absorbed by CaCO_3 . To determine the sequence of CaCO_3 sulfurization reactions, the equilibrium composition of the main sulfur-containing gases prior to reaction with CaCO_3 is shown in Figure 8.3. Considering the composition of the additive mixture and the gas phase presented in Figure 8.2 and Figure 8.3, the sulfurization process is explained by the reactions between SO_2 and CO and the formation of COS and S_2 . These reaction products subsequently react with CaCO_3 and CaO , generated from CaCO_3 decomposition, to form CaS . Figure 8.4 depicts the proposed mechanism.

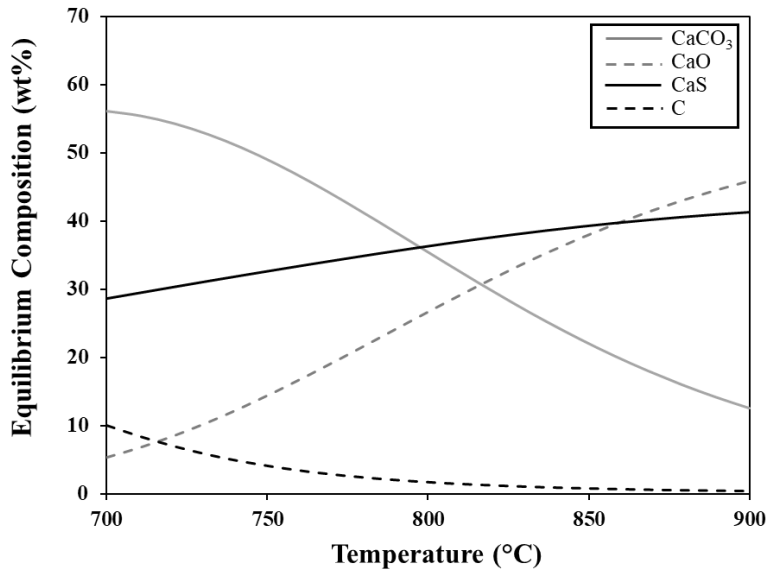


Figure 8.2 Equilibrium composition of the solids in Ca-S-C-O system at 5% S in burning coal ($P_{\text{SO}_2} = 0.016$ atm), and CO/CO_2 of 4.

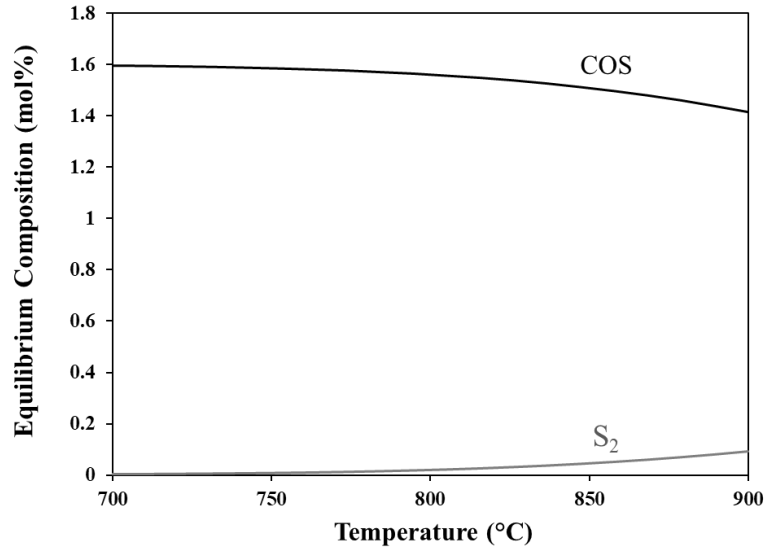


Figure 8.3 The equilibrium composition of the main sulfur-containing compounds in the gas mixture prior to reacting with the additives at 5% S in burning coal ($P_{SO_2} = 0.016$ atm), and CO/CO₂ of 4.

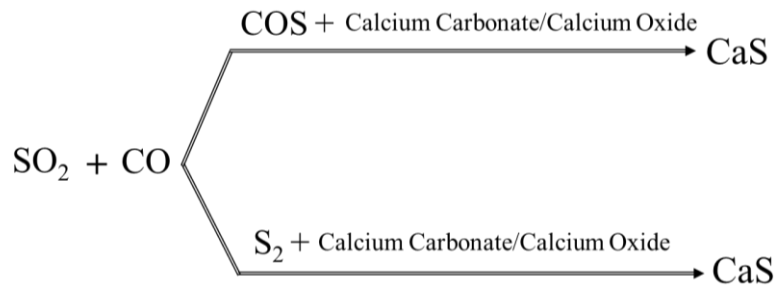


Figure 8.4 The sequence of the sulfurization reactions between input gas stream and CaCO₃ additive.

Table 8.1 presents a list of the main possible reactions associated with sulfur department in the system, including CaCO₃ and a simulated gas mixture from coal combustion. The SO₂ and CO react with each other and form intermediate gas species, COS and S₂, based on reactions 1 and 2 in Table 8.1. Then, S₂ and COS react with CaCO₃ and CaO to form CaS (Table 8.1, reactions 3-6). Reactions 11-14 in Table 8.1 show the overall sulfurization reactions.

Table 8.1 List of the probable sulfur department reactions in the system, including CaCO₃ and N₂-CO-CO₂-SO₂ gas mixture at 800 °C.

Reaction	Formation of intermediate gas species	$\Delta G^{\circ}_{800^{\circ}\text{C}}$ (kJ/mol SO ₂)
1	$3\text{CO (g)} + \text{SO}_2 \text{(g)} = \text{COS (g)} + 2\text{CO}_2 \text{(g)}$	-104.7
2	$2\text{CO (g)} + \text{SO}_2 \text{(g)} = 1/2\text{S}_2 \text{(g)} + 2\text{CO}_2 \text{(g)}$	-94.8
Reaction	Reaction with COS	$\Delta G^{\circ}_{800^{\circ}\text{C}}$ (kJ/mol COS)
3	$\text{CaCO}_3 + \text{COS (g)} = \text{CaS} + 2\text{CO}_2 \text{(g)}$	-78.8
4	$\text{CaO} + \text{COS (g)} = \text{CaS} + \text{CO}_2 \text{(g)}$	-91.2
Reaction	Reaction with S ₂	$\Delta G^{\circ}_{800^{\circ}\text{C}}$ (kJ/mol S ₂)
5	$2\text{CaCO}_3 + 2\text{CO (g)} + \text{S}_2 \text{(g)} = 2\text{CaS} + 4\text{CO}_2 \text{(g)}$	-177.5
6	$2\text{CaO} + 2\text{CO (g)} + \text{S}_2 \text{(g)} = 2\text{CaS} + 2\text{CO}_2 \text{(g)}$	-202.2
Reaction	Overall sulfurization reactions	$\Delta G^{\circ}_{800^{\circ}\text{C}}$ (kJ/mol SO ₂)
7	$\text{CaCO}_3 + 3\text{CO (g)} + \text{SO}_2 \text{(g)} = \text{CaS} + 4\text{CO}_2 \text{(g)}$	-183.5
8	$\text{CaO} + 3\text{CO (g)} + \text{SO}_2 \text{(g)} = \text{CaS} + 3\text{CO}_2 \text{(g)}$	-195.9

8.2.2 The XRD and SEM Analyses

The composition of the absorbent was examined at different processing times using XRD to identify the main sulfur-containing compound. The sulfur-rich regions were further analyzed by SEM-EDS.

The XRD patterns of CaCO₃ additive reacted with the input gas stream at 800 °C with different processing times of 0, 60, and 120 min are shown in Figure 8.5. While CaCO₃ is the only compound before high-temperature processing, CaS, and CaO are observed after the experiments. Decomposition of CaCO₃ results in the formation of CaO, and sulfurization reactions, discussed in section 8.2.1, lead to CaS formation. The intensity of CaCO₃ peaks decreases with the processing time, while the intensity of CaS peaks increases. These results indicate that a higher

amount of CaS is formed by increasing the processing time. The presence of CaS as the main sulfur-containing compound is in agreement with the results of the thermodynamic analysis.

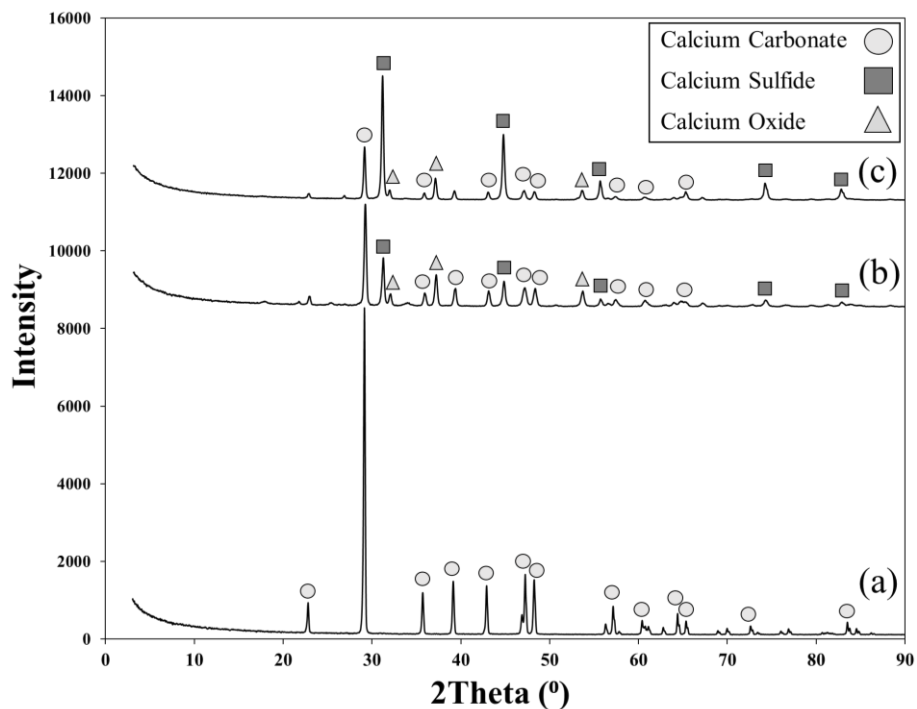


Figure 8.5 X-ray diffraction patterns of (a) raw CaCO₃ and processed CaCO₃ for (b) 60, and (c) 120 min at 800 °C.

The SEM-EDS analysis was performed on sample B-T2 to examine the sulfur-rich zones. Figure 8.6 illustrates SEM image and map analysis of sulfur, calcium, and oxygen. EDS point analysis of the sulfur-rich zones shown in Figure 8.6 (b) is presented in Table 8.2. The presence of sulfur in the reacted absorbent confirms the removal of sulfur from the input gas by the added CaCO₃.

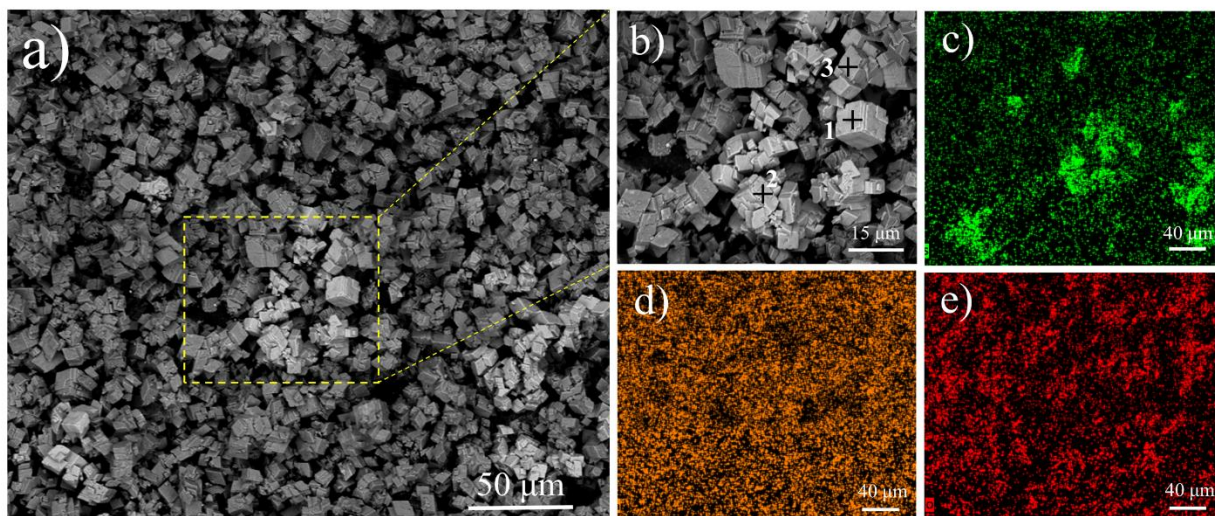


Figure 8.6 SEM image of sample (a) B-T2 and (b) sulfur-rich area. EDS elemental map of (c) sulfur, (d) calcium, and (e) oxygen.

Table 8.2 EDS analysis of the selected sulfur-rich points in sample B-T2.

EDS point	Ca (wt%)	S (wt%)	O (wt%)	C (wt%)
1	45.3	26.2	23.7	4.8
2	44	24	28.5	3.5
3	45.1	25.4	25.5	4

8.3 The Effect of the Processing Time on the Sulfur Absorption Behavior of CaCO_3

The sulfur content of the calcine for each experimental condition was measured with and without additive in order to determine the effect of CaCO_3 as a sulfur absorbent. Figure 8.7 illustrates %S in the calcine obtained by three times repetition of ICP-OES analysis at different processing times. The presence of CaCO_3 significantly reduces the absorption of sulfur from the input gas stream by the calcine.

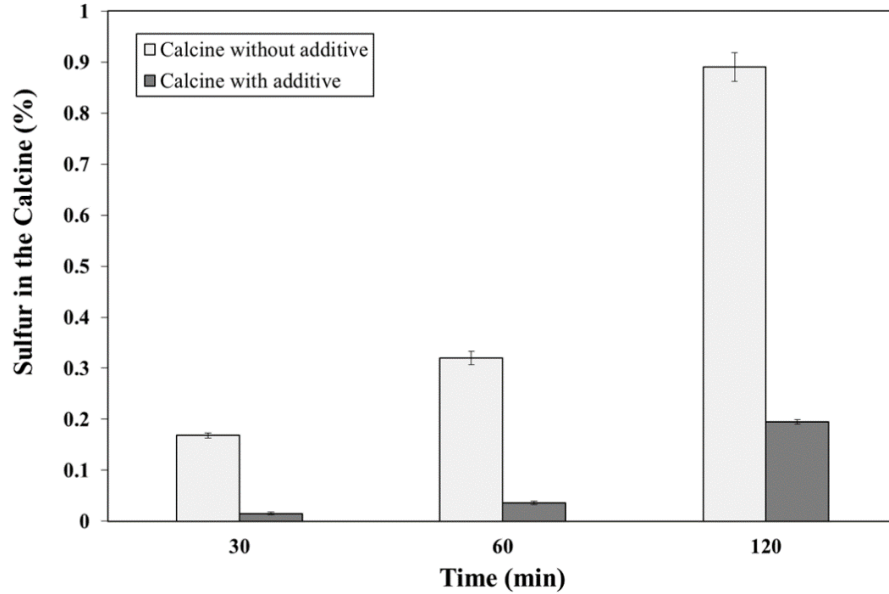


Figure 8.7 The effect of the processing time on the sulfur content of the calcine in the presence and absence of CaCO_3 additive at $800\text{ }^\circ\text{C}$, 5% S in burning coal ($P_{\text{SO}_2} = 0.016\text{ atm}$), and CO/CO_2 of 4.

The efficiency of CaCO_3 addition for reducing the sulfur absorption is quantified by sulfur reduction percentage, S_R , defined in equation 8.1:

$$S_R = \frac{(S_A - S_B)}{S_A} \times 100 \quad (8.1)$$

Where S_A is the %S in the calcine without the addition of CaCO_3 and S_B is the %S in the calcine in the presence of CaCO_3 . The sulfur reduction percentage of the calcines processed for various times is shown in Figure 8.8. By increasing the processing time from 30 to 120 min, S_R is decreased from 91.0 to 78.3%. The decrease in S_R is attributed to the sintering of CaCO_3 particles at the longer processing time, which results in smaller surface area of fresh CaCO_3 particles being available for reaction with SO_2 . Further, a longer processing time results in the sulfurization of the higher amount of CaCO_3 . Hence, fewer unreacted particles are available to react with sulfur-

containing gases. In order to observe the change in the microstructure of the additive at different processing times, SEM images of the CaCO_3 particles processed at 30, 60, and 120 min are shown in Figure 8.9. The CaCO_3 particles are sintered by increasing time. Image analysis was performed on SEM images by ImageJ software to estimate CaCO_3 particle size. The particle size distribution was determined by selecting 60 random particles on the SEM images of each sample. The particle size distribution for all three samples are shown in Figure 8.10. The P_{80} of CaCO_3 particles increases from 6.9 to 10.7 μm by raising processing time from 30 to 120 min. The increase in the particle size confirms the availability of smaller solid surface area to react with the sulfur-containing gases and slower kinetics of gas-solid reactions. Therefore, a smaller surface area of the additive indicates a decline in sulfur absorption from the gas to the additive.

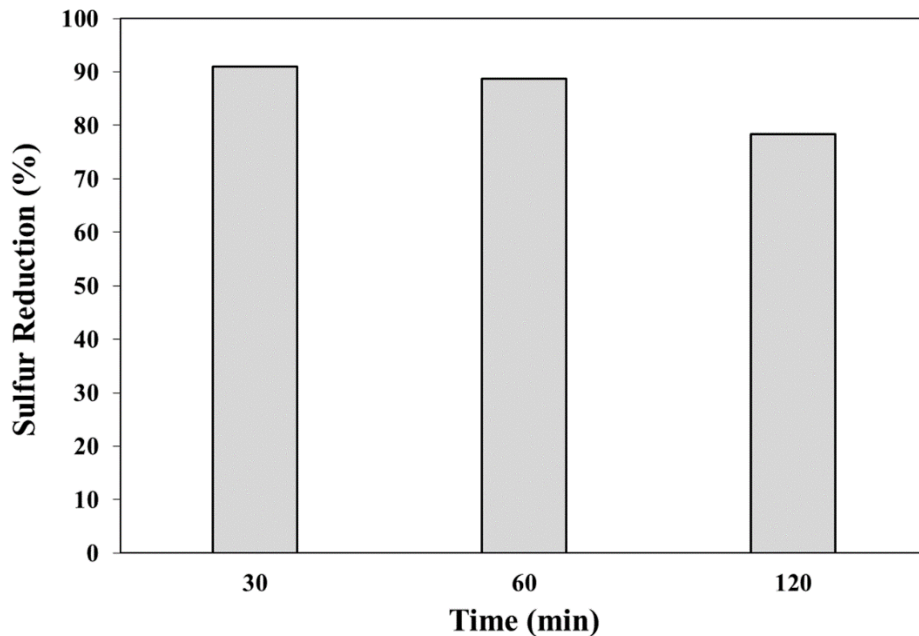


Figure 8.8 The effect of processing time on the sulfur reduction percentage in the calcine at 800 °C, 5% S in burning coal ($P_{\text{SO}_2} = 0.016$ atm), and CO/CO₂ of 4.

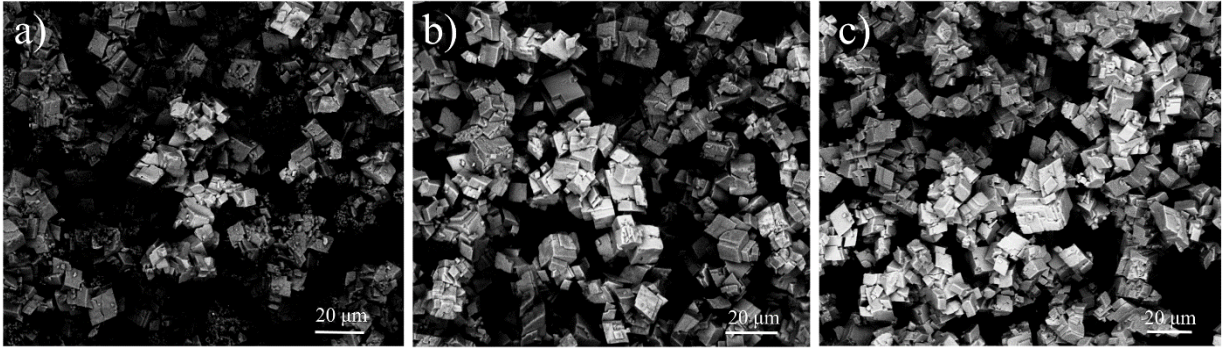


Figure 8.9 SEM images of CaCO₃ particles processed for (a) 30, (b) 60, and (c) 120 min at 800 °C, 5% S in burning coal ($P_{SO_2}= 0.016$ atm), and CO/CO₂ of 4.

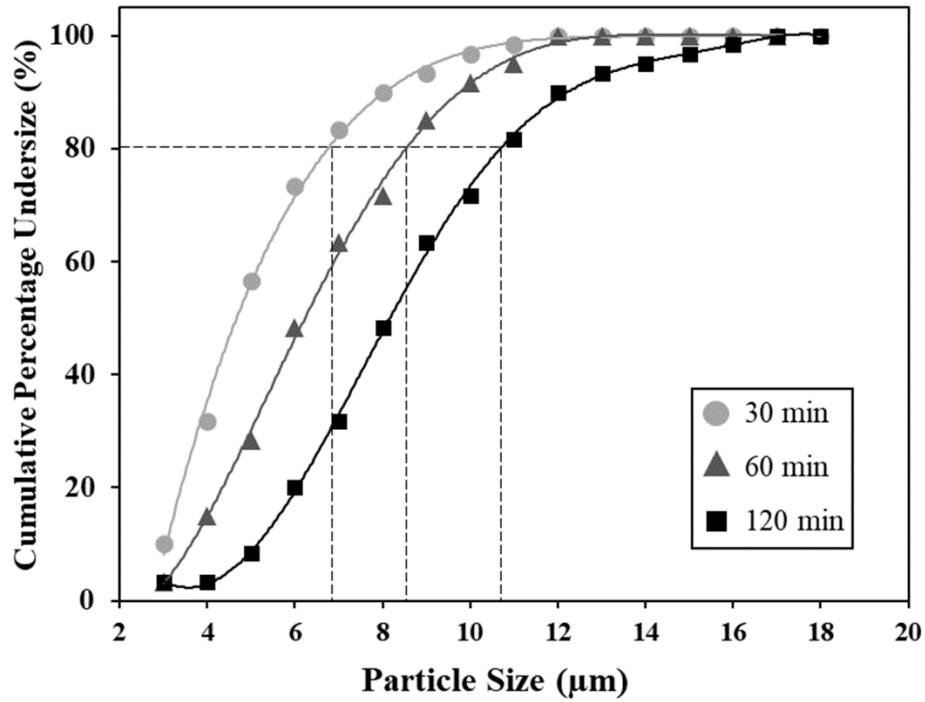


Figure 8.10 The particle size distribution of CaCO₃ additive processed for 30, 60, and 120 min at 800 °C, 5% S in burning coal ($P_{SO_2}= 0.016$ atm), and CO/CO₂ of 4.

8.4 The Effect of the Temperature on Sulfur Absorption Behavior of CaCO₃

The %S in the calcine was measured in both the presence and absence of CaCO₃ at 700, 800, and 900 °C by three times repetition of ICP analysis. The results presented in Figure 8.11 show that the presence of CaCO₃ considerably decreases the transfer of sulfur from the input gas mixture to the calcine due to the sulfur absorption by CaCO₃. As discussed in section 6.3.5, prior to the application of the sulfur absorbent, increasing temperature above 700 °C results in lower %S in the calcine due to the reduction of the surface area of the solid. However, the addition of CaCO₃ changes the behavior of the calcine with respect to the absorption of sulfur. To clarify the impact of CaCO₃ addition on the %S in the calcine at different temperatures, S_R is calculated at 700, 800 and 900 °C. The results are presented in Figure 8.12. Increasing the temperature from 700 to 800 °C leads to enhancing S_R from 77.3 to 88.8%. However, S_R decreases to 70.8 as the temperature rises to 900 °C. The processing temperature and CaCO₃ particle size are the two main parameters affecting the S_R value. Generally, the rate of gas-solid reactions increases as temperature rises. Thus, it is expected that higher temperature promotes the absorption of sulfur from gas to the additive, which in turn increases S_R. However, sintering of the particles decreases S_R and the kinetics of the gas-solid reactions. These two opposing effects results in an initial increase followed to by a decline in S_R.

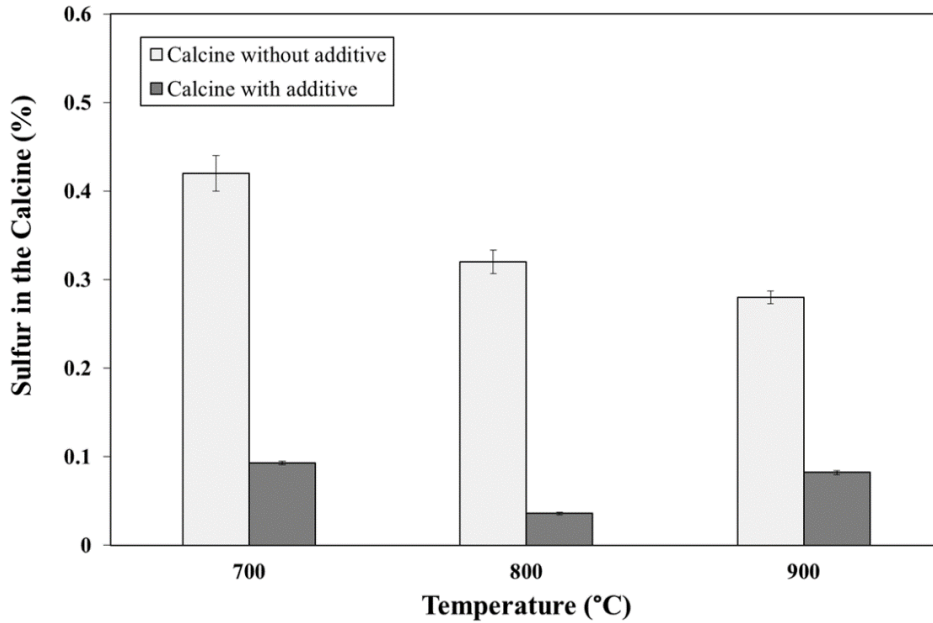


Figure 8.11 The effect of temperature on the sulfur content of the calcine in the presence/absence of CaCO_3 additive at 60 min processing time, 5% S in burning coal ($P_{\text{SO}_2} = 0.016$ atm), and CO/CO_2 of 4.

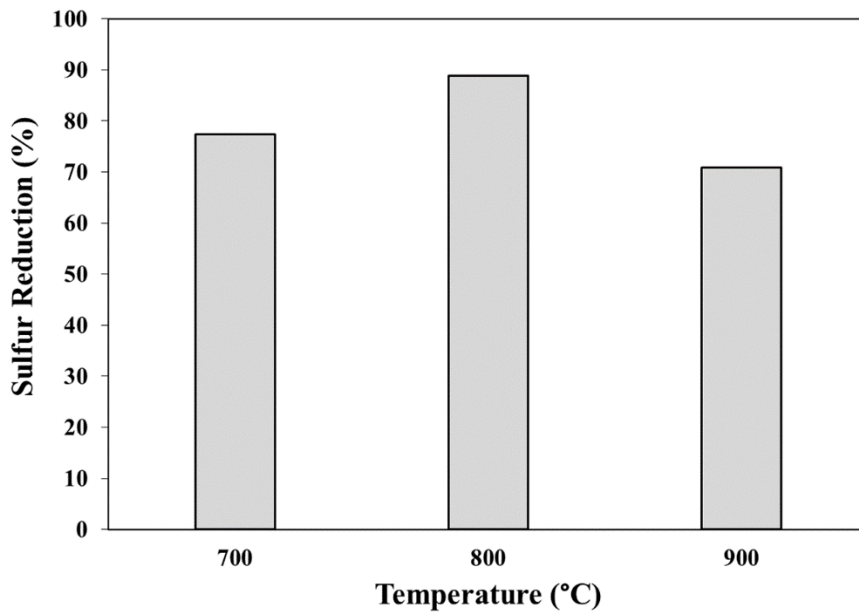


Figure 8.12 The effect of temperature on the sulfur reduction percentage in the calcine at 60 min processing time, 5% S in burning coal ($P_{\text{SO}_2} = 0.016$ atm), and CO/CO_2 of 4.

The SEM analysis was carried out to determine the effect of temperature on CaCO_3 particle size. The images shown in Figure 8.13 demonstrate the sintering of CaCO_3 particles by increasing temperature. A significant increase in particle size is observed at 900 °C, which is attributed to the sintering of CaCO_3 particles. Sintering of CaCO_3 at similar temperatures has been observed by other researchers [153, 154]. The P_{80} of CaCO_3 particles is calculated by performing image analysis using ImageJ software on SEM images. The size of 60 random particles was measured in each sample to determine the particle size distribution shown in Figure 8.14. The P_{80} of CaCO_3 particles at 700, 800, and 900 °C is estimated to be 7.1, 8.5, and 10.4 μm , respectively. It is concluded that increasing the rate of gas-solid reactions by raising the temperature and surface area reduction by sintering of the particles are two opposing parameters that influence the kinetics of sulfur absorption from the gas mixture to CaCO_3 . Increasing temperature to 900 °C results in sintering of CaCO_3 particles and a considerable increase in particle size, which in turn reduces S_R and sulfur absorption from the gas phase to the additive. The highest S_R value is found to be 88.8% at 800 °C.

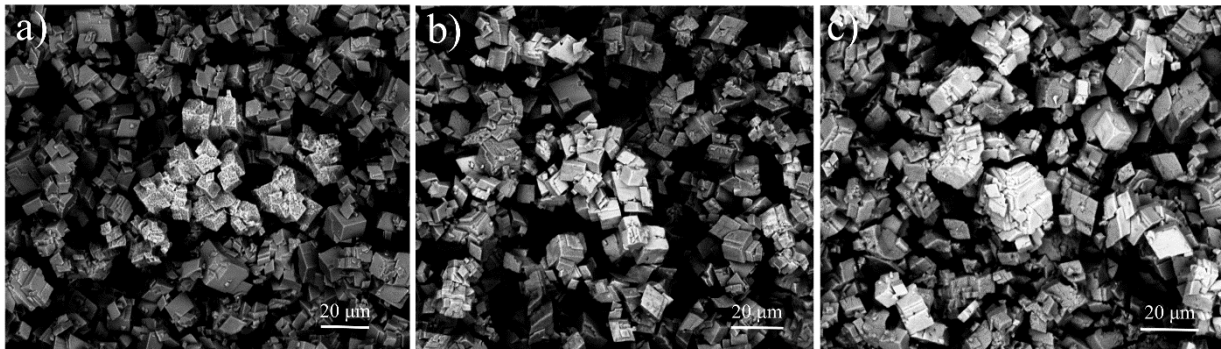


Figure 8.13 SEM images of CaCO_3 particles processed for 60 min at (a) 700, (b) 800, and (c) 900 °C.

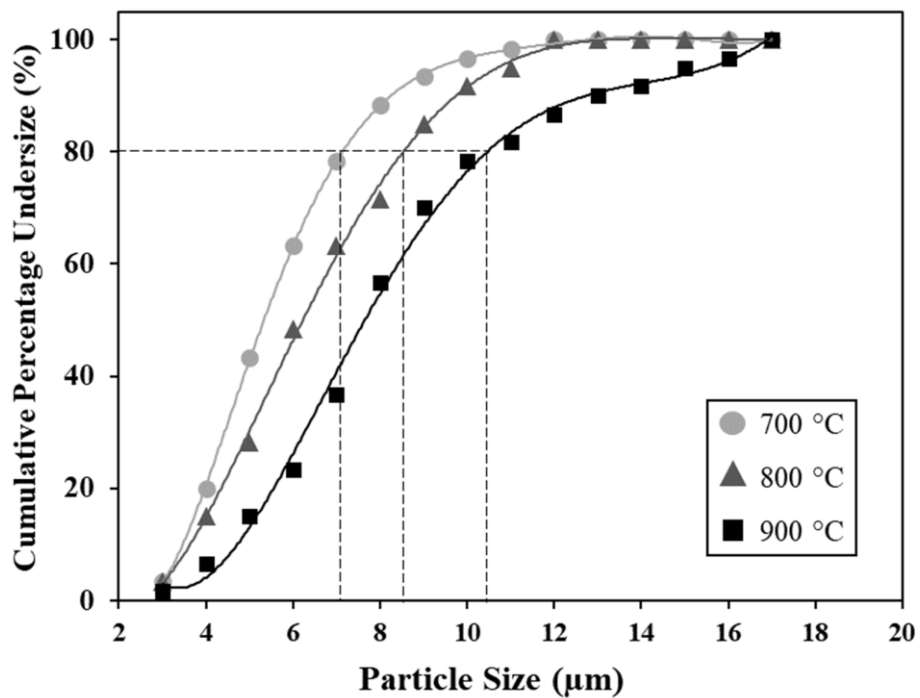


Figure 8.14 The particle size distribution of CaCO₃ additive processed at 700, 800, and 900 °C.

8.5 Conclusion

CaCO₃ is used as a sulfur absorbent in nickel laterite calcination to inhibit the transfer of sulfur in the atmosphere to the calcine. The gases emitted from fuel combustion react with CaCO₃ and generate sulfur-bearing solid compounds, which in turn decreases the %S in the calcine. Based on the results of the XRD analysis and thermodynamic simulations, CaS is identified as a main sulfur-containing compound in the additive after the calcination process. The addition of CaCO₃ as a sulfur absorbent leads to 70.8-91.0% sulfur removal in the calcine at various processing times and temperatures. The sulfur reduction percentage decreases from 91 to 78.3% by increasing the processing time from 30 to 120 min at 800 °C. The above observation is due to the sintering of CaCO₃ particles and smaller unreacted surface area of CaCO₃ particles available to react with the

gaseous species. Increasing the temperature from 700 to 900 °C at a constant processing time of 60 minutes causes two contradictory effects on the kinetics of gas-solid reactions. The rate of sulfurization reactions initially increases by raising the temperature; however, however increasing the temperature above 800°C results in sintering of CaCO₃ particles and causes slower reaction kinetics. The highest sulfur removal percentage (88.8%) is obtained at 800 °C.

Chapter 9: Conclusions and Recommendations for Future Work

A comprehensive understanding of sulfur department in nickel laterite calcination is essential in order to control the sulfur content of the calcine and consequently the final FeNi product. Decreasing sulfur absorption from the rotary kiln fuel to the calcine is critical for reducing the load of the refinery. The overall objective of this study is to gain a fundamental understanding of sulfur department in nickel laterite calcination and to find a solution to decrease sulfur transfer from the fuel to the calcine in the calcination stage. The following conclusions and recommendations have been developed based on the findings of the high-temperature experiments and thermodynamic analysis.

9.1 Conclusions

- 1- The main reactions that occur during the calcination stage are identified as transformation of goethite to hematite, dissociation of lizardite, and silicate decomposition. The above reactions take place at 300, 600, and 800 °C, respectively.
- 2- The kinetic model and kinetic parameters of the main reactions that occur during nickel laterite calcination are identified by combining model-free and model-fitting approaches. The activation energy values of the reactions at 300, 600, and 800 °C, are calculated as 24.5, 125.1, and 273.1 kJ/mol, respectively. The Avrami-Erofeev model is identified as the best kinetic model for these reactions.
- 3- Based on the XRD results, pyrrhotite is found to be the main sulfur-containing compound in the calcine.

- 4- The effect of various parameters such as the P_{SO_2} resulted from coal combustion, the reducing atmosphere in the furnace, gas flow rate, and temperature on sulfurization behavior and composition of the calcine are investigated. Increasing the sulfur content of the coal, using a more reducing atmosphere, and increasing fuel consumption lead to higher %S in the calcine. The sulfur deportation from gas to the solid shows a slight decrease by raising fuel consumption due to the shorter residence time of the gas in the furnace. The %S in the calcine and sulfur deportation are increased by raising the temperature from 600 to 700 °C. However, the sintering of particles as well as recrystallization of the silicate compounds result in lower %S in the calcine and sulfur deportation at temperatures above 700 °C.
- 5- The kinetics of sulfur deportment in nickel laterite calcination is studied by a combination of model-free, model-fitting, and master plot methods. According to the E values obtained by model-free method, the process is divided into two steps, before and after 60 min of calcination. Contracting sphere and Avrami-Erofeev are identified as the most suitable kinetic models for steps 1 and 2, respectively. According to the small E values, 1.4-5.3 kJ/mol, the sulfurization reactions are identified as diffusion-controlled. The variation of P_{SO_2} does not have a significant impact on the reaction rate.
- 6- The developed kinetic models for the two steps of the sulfur deportation process are as follow:

$$\frac{d\alpha}{dt} = A \exp\left(\frac{-E}{RT}\right) (3[1 - \alpha]^{\frac{2}{3}}) (P_{SO_2} - P_{SO_2,eq})^{0.139} \quad 0 < \alpha < 0.4 \quad (\text{step 1})$$

$$\frac{d\alpha}{dt} = A \exp\left(\frac{-E}{RT}\right) (3[1 - \alpha][-\ln(1 - \alpha)]^{\frac{2}{3}}) (P_{SO_2} - P_{SO_2,eq})^{0.065} \quad 0.4 \leq \alpha < 1 \quad (\text{step 2})$$

Where P_{SO_2} is in the range of 6.4×10^{-3} to 2.6×10^{-2} , which corresponds to 2-8% sulfur in the burning coal.

- 7- A new approach to decrease the transfer of sulfur from fuel combustion gas mixture to the calcine is proposed. $CaCO_3$ as a sulfur absorbent is placed at one side of the furnace tube where the input gas stream enters the furnace. The addition of $CaCO_3$ decreases the %S in the calcine. The addition of $CaCO_3$ leads to 70.8-91% sulfur removal in the calcine processed at 700-900 °C for 30-120 min. According to XRD and thermodynamic results, CaS is identified as the main sulfur-containing product of the sulfurization of $CaCO_3$.
- 8- The effect of the processing time and temperature on the sulfur absorption behavior of $CaCO_3$ are investigated. Increasing the processing time from 30 to 120 min at constant temperature of 800 °C causes a decrease in sulfur removal from 91 to 78.3%. This is attributed to the sintering of $CaCO_3$ particles and lower availability of unreacted $CaCO_3$ particles to react with SO_2 . When calcining the ore for 60 minutes, the sulfur removal is increased by raising the temperature from 700 to 800 °C; however, raising the temperature to 900 °C causes sintering of $CaCO_3$ particles, which in turn reduces the available surface area and sulfur removal percentage. At constant processing time of 60 min, the highest sulfur removal in the range of 700-900 °C is achieved at 800 °C with a value of 88.8%.

9.2 Recommendations

- 1- Typical rotary kilns used in metals and minerals sectors are heated directly by oxidizing a fuel in a burner. The lab-scale furnaces, however, are heated indirectly via electric resistance heating. The difference between the heating mechanisms influences the heat transfer between the furnace atmosphere and the ore, which will affect the reaction kinetics.

More specifically, the ore processed in the lab is calcined at a constant temperature; however, in fuel fired kilns the ore experiences different temperatures as it travels from one end of the furnace to the other end. Thus, it is recommended to conduct high-temperature experiments in a fuel fired rotary kiln will provide a temperature profile similar to the one in an industrial plant.

- 2- The mineralogy of the ore can affect the sulfurization behavior of the laterite ore. In this research, it is concluded that iron is the main element in the ore that reacts with sulfur. However, changing the ore mineralogy leads to the variation in the iron-containing compounds in the raw ore, which will in turn influence the reaction with sulfur. Further experiments are required to investigate the effect of the ore mineralogy on the sulfur department in nickel laterite calcination.
- 3- Performing kinetic analysis on sulfur deportation by changing the intensity of the reducing atmosphere will provide insight on the effect of CO/CO₂ on the kinetics of sulfurization reactions.
- 4- It is beneficial to investigate the effect of other operational parameters such as the rotating speed of the rotary kiln and the ore particle size on the sulfur department behavior in the nickel laterite calcination.

Bibliography

- [1] T.M. Pollock, S. Tin, Nickel-based superalloys for advanced turbine engines: chemistry, microstructure and properties, *J. Propuls. Power.* 22 (2006) 361–374.
- [2] A. Hasanbeigi, M. Arens, L. Price, Alternative emerging ironmaking technologies for energy-efficiency and carbon dioxide emissions reduction: a technical review, *Renew. Sustain. Energy Rev.* 33 (2014) 645–658.
- [3] G. Li, H. Jia, J. Luo, Z. Peng, Y. Zhang, T. Jiang, Ferronickel preparation from nickeliferous laterite by rotary kiln-electric furnace process, *Charact. Miner. Met. Mater.* (2016) 143–150.
- [4] R.E. Kirk, D.F. Othmer, *Encyclopedia of chemical technology. Vol 3.* Interscience Encyclopedia, Wiley, 1953.
- [5] G.M. Mudd, S.M. Jowitt, A detailed assessment of global nickel resource trends and endowments, *Econ. Geol.* 109 (2014) 1813–1841.
- [6] M. Rao, G. Li, T. Jiang, J. Luo, Y. Zhang, X. Fan, Carbothermic reduction of nickeliferous laterite ores for nickel pig iron production in China: A Review, *JOM* 65 (2013) 1573–1583.
- [7] N. Campagnol, K. Hoffman, A. Lala, O. Ramsbottom, *The future of nickel: A class act, Report*, McKinsey & Company, 2017.
- [8] C.R. Butt, D. Cluzel, Nickel laterite ore deposits: weathered serpentinites, *Elements* 9 (2013) 123–128.
- [9] A. Janwong, *The agglomeration of nickel laterite ore*, PhD Thesis, The University of Utah, 2012.
- [10] A. Vahed, P.J. Mackey, A.E.M. Warner, “Around the nickel world in eighty days”: A virtual tour of world nickel sulphide and laterite operations and technologies, *5th Int. Symp. Nickel Cobalt*, Springer (2021) 3–39.
- [11] A. Bunjaku, *The effect of mineralogy, sulphur, and reducing gases on the reducibility of saprolitic nickel ores*, PhD Thesis, Aalto University, 2013.
- [12] D.R. Swinbourne, Understanding ferronickel smelting from laterites through computational thermodynamics modelling, *Miner. Process. Extr. Metall.* 123 (2014) 127–140.

- [13] F. Crundwell, M. Moats, V. Ramachandran, T. Robinson, W.G. Davenport, Extractive metallurgy of nickel, cobalt and platinum group metals, Elsevier, 2011.
- [14] R. Elliott, A study on the role of sulphur in the thermal upgrading of nickeliferous laterite ores, Master's Thesis, Queen's University, 2015.
- [15] D. Bäckström, R. Johansson, K. Andersson, H. Wiinikka, C. Fredriksson, On the use of alternative fuels in rotary kiln burners - An experimental and modelling study of the effect on the radiative heat transfer conditions, *Fuel Process. Technol.* 138 (2015) 210–220.
- [16] F. O’connor, W.H. Cheung, M. Valix, Reduction roasting of limonite ores: effect of dehydroxylation, *Int. J. Miner. Process.* 80 (2006) 88–99.
- [17] M. Valix, W.H. Cheung, Study of phase transformation of laterite ores at high temperature, *Miner. Eng.* 15 (2002) 607–612.
- [18] V.V. Sidorov, V.E. Rigin, P.G. Min, Y.I. Folomeikin, Removal of a sulfur impurity from complex nickel melts in vacuum, *Russ. Metall. Met.* 11 (2015) 910–915.
- [19] T. Ogura, K. Kuwayama, A. Ono, Y. Yamada, Production of Fe-Ni by the rotary kiln-electric furnace process at Hyuga Smelter, *Int. J. Miner. Process.* 19 (1987) 189–198.
- [20] A. Ma, S. Mostaghel, K. Chattopadhyay, Review of applicable desulphurization models for crude ferronickel refining, *Miner. Process. Extr. Metall.* 127 (2018) 10–28.
- [21] R. Kurose, M. Ikeda, H. Makino, M. Kimoto, T. Miyazaki, Pulverized coal combustion characteristics of high-fuel-ratio coals, *Fuel* 83 (2004) 1777–1785.
- [22] L. Greenburg, M.B. Jacobs, Sulfur Dioxide in New York City Atmosphere, *Ind. Eng. Chem.* 48 (1956) 1517–1521.
- [23] P. Billings, Emission of hazardous air pollutants from coal-fired power plants, Report, *Env. Health Eng.*, 2007.
- [24] E. Bolat, S. Sağlam, S. Pişkin, Chemical demineralization of a Turkish high ash bituminous coal, *Fuel Process. Technol.* 57 (1998) 93–99.
- [25] J.P. Golightly, Nickeliferous laterites: A general description, *Int. Laterite Symp. Proc.* (1979) 1–23.

- [26] M.A. Rhamdhani, J. Chen, T. Hidayat, E. Jak, P. Hayes, Advances in research on nickel production through the Caron process, *Proceedings of EMC* (2009) 899–913.
- [27] G.M. Mudd, Global trends and environmental issues in nickel mining: Sulfides versus laterites, *Ore Geol. Rev.* 38 (2010) 9–26.
- [28] S. Pournaderi, Optimization of ferronickel production from Sivrihisar nickel laterite ore, PhD Thesis, Middle East Technical University, 2014.
- [29] D.B. Nahon, H. Paquet, J. Delvigne, Lateritic weathering of ultramafic rocks and the concentration of nickel in the western Ivory Coast, *Econ. Geol.* 77 (1982) 1159–1175.
- [30] C. Villanova-de-Benavent, C. Domènech, E. Tauler, S. Galí, S. Tassara, J.A. Proenza, Fe–Ni-bearing serpentines from the saprolite horizon of Caribbean Ni-laterite deposits: new insights from thermodynamic calculations, *Miner. Deposita* 52 (2017) 979–992.
- [31] J. Golightly, G.J. Paul, Nickeliferous laterite deposits, *Econ. Geol.* 75 (1981) 710–735.
- [32] A.J. Monhemius, Treatment of laterite ores of nickel to produce ferronickel, matte or precipitated sulphide, *Extr. Metall. Nickel* (1987) 51–75.
- [33] M. Elias, Nickel laterite deposits-geological overview, resources and exploitation, *Giant Ore Depos. Charact. Genes. Explor. CODES Spec. Publ.* 4 (2002) 205–220.
- [34] N.W. Brand, Nickel laterites: classification and features, *AGSO J Aust Geol Geophys.* 17 (1998) 81–88.
- [35] J. Kierczak, C. Neel, H. Bril, J. Puziewicz, Effect of mineralogy and pedoclimatic variations on Ni and Cr distribution in serpentine soils under temperate climate, *Geoderma.* 142 (2007) 165–177.
- [36] A.D. Dalvi, W.G. Bacon, R.C. Osborne, The past and the future of nickel laterites, *Int. Conv. Trade Show Invest. Exch.* (2004) 1–27.
- [37] T. Norgate, S. Jahanshahi, Assessing the energy and greenhouse gas footprints of nickel laterite processing, *Miner. Eng.* 24 (2011) 698–707.
- [38] P. Prasetyo, The effect of entry into force of the mining law 2009 began January 2014 in the production of NPI (nickel pig iron) in China, *IOP Conf. Ser. Mater. Sci. Eng.* (2018) 012015.

- [39] C.S. Simons, The production of nickel: extractive metallurgy—past, present, and future, *Extr. Metall. Nickel Cobalt* (1988) 91–134.
- [40] J. Vaughan, W. Hawker, D. White, Chemical aspects of mixed nickel-cobalt hydroxide precipitation and refining, *Proc. ALTA NiCoCu Conf.* (2011) 23–25.
- [41] J. Kyle, Nickel laterite processing technologies—where to next?, *ALTA NiCoCu Conf.*, 2010.
- [42] R.R. Moskalyk, A.M. Alfantazi, Nickel laterite processing and electrowinning practice, *Miner. Eng.* 15 (2002) 593–605.
- [43] J.E. Fittock, J.E. Fittock, Nickel and cobalt refining by QNI Pty Ltd, Yabulu, QLD, Mawby-AUSIMM Monograph 19 (2007) 1-47.
- [44] I.J. Kotze, Pilot plant production of ferronickel from nickel oxide ores and dusts in a DC arc furnace, *Miner. Eng.* 15 (2002) 1017–1022.
- [45] A.E.M. Warner, C.M. Diaz, A.D. Dalvi, P.J. Mackey, A.V. Tarasov, JOM world nonferrous smelter survey, part III: nickel: laterite, *JOM* 58 (2006) 11–20.
- [46] S. Kashani-Nejad, I. Candy, M. Kozłowski, Modelling of nickel laterite kiln processing—a conceptual review, 44th Annual Conference of Metallurgists (2005) 231–246.
- [47] G.K. Gaurav, S. Khanam, Analysis of temperature profile and % metallization in rotary kiln of sponge iron process through CFD, *J. Taiwan Inst. Chem. Eng.* 63 (2016) 473–481.
- [48] K. Moriyama, M. Yamagiwa, A. Kaikake, H. Takano, Recent improvement of reduction rotary kiln operations at Hyuga Smelting Co., Ltd., *TMS Int. Laterite Nickel Symp.* (2004) 733–740.
- [49] Q. Huang, X. Lv, Phases transformation of nickel lateritic ore during dehydration, *J. Min. Metall. B Metall.* 47 (2011) 45–51.
- [50] B. Rizov, Phase transformations from goethite to hematite and thermal decomposition in various nickeliferous laterite ores, *J. Univ. Chem. Technol. Metall.* 47 (2012) 207–210.
- [51] M. Jiang, T. Sun, Z. Liu, J. Kou, N. Liu, S. Zhang, Mechanism of sodium sulfate in promoting selective reduction of nickel laterite ore during reduction roasting process, *Int. J. Miner. Process.* 123 (2013) 32–38.

- [52] G. Li, T. Shi, M. Rao, T. Jiang, Y. Zhang, Beneficiation of nickeliferous laterite by reduction roasting in the presence of sodium sulfate, *Miner. Eng.* 32 (2012) 19–26.
- [53] K. Karalis, N. Karkalos, G.S.E. Antipas, A. Xenidis, Pragmatic analysis of the electric submerged arc furnace continuum, *R. Soc. Open Sci.* 4 (2017) 170313.
- [54] K.T. Karalis, N. Karkalos, N. Cheimarios, G.S.E. Antipas, A. Xenidis, A.G. Boudouvis, A CFD analysis of slag properties, electrode shape and immersion depth effects on electric submerged arc furnace heating in ferronickel processing, *Appl. Math. Model.* 40 (2016) 9052–9066.
- [55] M.Y. Solar, I. Candy, B. Wasmund, Selection of optimum ferronickel grade for smelting nickel laterites, *CIM Bull.* 11 (2008) 1-8.
- [56] N. Voermann, T. Gerritsen, I. Candy, F. Stober, A. Matyas, Furnace technology for ferro-nickel production-an update, *TMS Int. Laterite Nickel Symp.* (2004) 563–577.
- [57] C. Xu, Q. Dai, L. Gaines, M. Hu, A. Tukker, B. Steubing, Future material demand for automotive lithium-based batteries, *Commun. Mater.* 1 (2020) 1–10.
- [58] R. Gomez, C.T. Ogryzlo, A.A. Dor, The Cerro Matoso nickel project, *Evans Eds Int. Laterite Symp.* (1979) 412–458.
- [59] Y. Hernández, J.G. Carriazo, O. Almanza, Characterization by XRD and electron paramagnetic resonance (EPR) of waste materials from “Cerro Matoso” Mine (Colombia), *Mater. Charact.* 57 (2006) 44–49.
- [60] J.R. Kift, C.E. Ferrer, A historical overview of the Cerro Matoso operation 1980 to 2003, *TMS Int. Laterite Nickel Symp.* (2004) 719–731.
- [61] C. Doyle, The steps required to meet production targets at PT INCO, Indonesia: a new innovative business strategy, *TMS Int. Laterite Nickel Symp.* (2004) 667–684.
- [62] J.D. Guiry, A.D. Dalvi, PT INCO’s Indonesian nickel project: An updating, *Int. J. Miner. Process.* 19 (1987) 199–214.
- [63] O. Marin, M.L. Joshi, O. Charon, J. Dugue, Preferential oxygen firing system for counter-current mineral calcining, US Patent, 2000.

- [64] O. Polyakov, Technology of ferronickel, *Handb. Ferroalloys*, Elsevier (2013) 367–375.
- [65] K. Baba, I. Nagatomo, Method of manufacturing granulated ferronickel, US Patent, 1980.
- [66] E. Keskinilic, S. Pournaderi, A. Geveci, Y.A. Topkaya, Calcination characteristics of laterite ores from the central region of Anatolia, *J. South. Afr. Inst. Min. Metall.* 112 (2012) 877–882.
- [67] E. Zevgolis, C. Zografidis, T. Perraki, E. Devlin, Phase transformations of nickeliferous laterites during preheating and reduction with carbon monoxide, *J. Therm. Anal. Calorim.* 100 (2010) 133–139.
- [68] F. López, M. Ramírez, J. Pons, A. López-Delgado, F. Alguacil, Kinetic study of the thermal decomposition of low-grade nickeliferous laterite ores, *J. Therm. Anal. Calorim.* 94 (2008) 517–522.
- [69] E. Keskinilic, S. Pournaderi, A. Geveci, Y.A. Topkaya, Calcination behavior of Sivrihisar laterite ores of Turkey, *2nd Int. Symp. High-Temp. Metall. Process.*, Wiley (2011) 319–326.
- [70] J. Li, X. Li, Q. Hu, Z. Wang, Y. Zhou, J. Zheng, W. Liu, L. Li, Effect of pre-roasting on leaching of laterite, *Hydrometallurgy* 99 (2009) 84–88.
- [71] A. Garces-Granda, G.T. Lapidus, O.J. Restrepo-Baena, The effect of calcination as pre treatment to enhance the nickel extraction from low-grade laterites, *Miner. Eng.* 120 (2018) 127–131.
- [72] E. Zevgolis, C. Zografidis, I. Halikia, The reducibility of the Greek nickeliferous laterites: a review, *Miner. Process. Extr. Metall.* 119 (2010) 9–17.
- [73] A. Bunjaku, M. Kekkonen, K. Pietilä, P. Taskinen, Effect of mineralogy and reducing agent on reduction of saprolitic nickel ores, *Miner. Process. Extr. Metall.* 121 (2012) 156–165.
- [74] J. Yang, G. Zhang, O. Ostrovski, S. Jahanshahi, Changes in an Australian laterite ore in the process of heat treatment, *Miner. Eng.* 54 (2013) 110–115.
- [75] S. Li, Study of nickeliferous laterite reduction, PhD Thesis, McMaster University, 1999.
- [76] C.J. Hallet, A thermodynamic analysis of the solid state reduction of nickel from laterite minerals, *Int. Symp. Pyrometallurgical Fundam. Process Dev.* (1997) 17–20.

- [77] J.E. Lopez-Rendon, Geology, Mineralogy and geochemistry of the Cerro Matoso nickeliferous laterite, Cordoba, Colombia, PhD Thesis, Colorado State University, 1986.
- [78] J.-O. Park, H.-S. Kim, S.-M. Jung, Use of oxidation roasting to control NiO reduction in Ni-bearing limonitic laterite, *Miner. Eng.* 71 (2015) 205–215.
- [79] B. Li, Z. Ding, Y. Wei, S. Zhou, H. Wang, Reduction of nickel and iron from low-grade nickel laterite ore via a solid-state deoxidization method using methane, *Mater. Trans.* 59 (2018) 1180–1185.
- [80] H. Purwanto, T. Shimada, R. Takahashi, J. Yagi, Reduction rate of cement bonded laterite briquette with CO-CO₂ gas, *ISIJ Int.* 41 (2001) 31–35.
- [81] H.S. Ray, R. Sridhar, K.P. Abraham, Extraction of nonferrous metals, Affiliated East-West Press Ltd., 1985.
- [82] B. Li, H. Wang, Y. Wei, The reduction of nickel from low-grade nickel laterite ore using a solid-state deoxidisation method, *Miner. Eng.* 24 (2011) 1556–1562.
- [83] S. Vyazovkin, A.K. Burnham, J.M. Criado, L.A. Pérez-Maqueda, C. Popescu, N. Sbirrazzuoli, ICTAC Kinetics Committee recommendations for performing kinetic computations on thermal analysis data, *Thermochim. Acta.* 520 (2011) 1–19.
- [84] S. Vyazovkin, K. Chrissafis, M.L. Di Lorenzo, N. Koga, M. Pijolat, B. Roduit, N. Sbirrazzuoli, J.J. Suñol, ICTAC Kinetics Committee recommendations for collecting experimental thermal analysis data for kinetic computations, *Thermochim. Acta.* 590 (2014) 1–23.
- [85] B. Janković, B. Adnadević, S. Mentus, The kinetic analysis of non-isothermal nickel oxide reduction in hydrogen atmosphere using the invariant kinetic parameters method, *Thermochim. Acta.* 456 (2007) 48–55.
- [86] B. Janković, B. Adnadević, S. Mentus, The kinetic study of temperature-programmed reduction of nickel oxide in hydrogen atmosphere, *Chem. Eng. Sci.* 63 (2008) 567–575.
- [87] T.A. Utigard, M. Wu, G. Plascencia, T. Marin, Reduction kinetics of Goro nickel oxide using hydrogen, *Chem. Eng. Sci.* 60 (2005) 2061–2068.

- [88] G. Plascencia, T. Utigard, The reduction of Tokyo and Sinter 75 nickel oxides with hydrogen, *Chem. Eng. Sci.* 64 (2009) 3879–3888.
- [89] T.A. Utigard, G. Plascencia, T. Marin, A.E.M. Warner, J. Liu, A. Vahed, M. Muinonen, Hydrogen reduction of industrial nickel oxides, *Can. Metall. Q.* 44 (2005) 421–428.
- [90] G. Plascencia, Reduction of industrial nickel oxides with a hydrogen bearing gas between 523 and 673K, *Arch. Metall. Mater.* 63 (2018) 781–789.
- [91] S.L. Kharatyan, H.A. Chatilyan, K.V. Manukyan, Kinetics and mechanism of nickel oxide reduction by methane, *J. Phys. Chem. C.* 123 (2019) 21513–21521.
- [92] S. Vyazovkin, C.A. Wight, Model-free and model-fitting approaches to kinetic analysis of isothermal and nonisothermal data, *Thermochim. Acta.* 340–341 (1999) 53–68.
- [93] A. Fernandez, A. Saffe, R. Pereyra, G. Mazza, R. Rodriguez, Kinetic study of regional agro-industrial wastes pyrolysis using non-isothermal TGA analysis, *Appl. Therm. Eng.* 106 (2016) 1157–1164.
- [94] S. Vyazovkin, On the phenomenon of variable activation energy for condensed phase reactions, *New J. Chem.* 24 (2000) 913–917.
- [95] B. Li, Z. Ding, Y. Wei, H. Wang, Y. Yang, M. Barati, Kinetics of reduction of low-grade nickel laterite ore using carbon monoxide, *Metall. Mater. Trans. B* 49 (2018) 3067–3073.
- [96] B. Li, H. Wang, Y.G. Wei, Kinetic analysis for non-isothermal solid state reduction of nickel laterite ore by carbon monoxide, *Miner. Process. Extr. Metall.* 121 (2012) 178–184.
- [97] X. Lv, W. Lv, Z. You, X. Lv, C. Bai, Non-isothermal kinetics study on carbothermic reduction of nickel laterite ore, *Powder Technol.* 340 (2018) 495–501.
- [98] Y. Liu, X. Lv, Z. You, X. Lv, Kinetics study on non-isothermal carbothermic reduction of nickel laterite ore in presence of Na₂SO₄, *Powder Technol.* 362 (2020) 486–492.
- [99] J. Szekely, J.W. Evans, H.Y. Sohm, *Gas-solid reactions*, Academic Press, 1976.
- [100] C.G. Fink, V.S. de Marchi, Beneficiating ferruginous bauxites through chlorination, *Trans. Electrochem. Soc.* 74 (1938) 469.

- [101] R.D. Holliday, D.J. Milne, Experimental evaluation of routes for purification of bauxite by gas-solid reactions, *Ind. Eng. Chem. Process Des. Dev.* 14 (1975) 447–452.
- [102] D.J. Milne, R.D. Holliday, Thermodynamics of gas-solid reactions for purification of bauxite at moderate temperatures, *Ind. Eng. Chem. Process Des. Dev.* 14 (1975) 442–447.
- [103] P. Bolsaitis, K. Nagata, Kinetics of sulfidization of iron oxide with SO₂-CO mixtures of high sulfur potential, *Metall. Trans. B* 11 (1980) 185–197.
- [104] K. Nagata, P. Bolsaitis, Selective removal of iron oxide from laterite by sulphurization and chlorination, *Int. J. Miner. Process.* 19 (1987) 157–172.
- [105] Roine A, Mansikka-Aho J, Björklund P, Kentala J, Lamberg P. HSC Chemistry 5.1 and 6.0 Outokumpu Technology, Chemical Reaction and Equilibrium Software with Extensive Thermochemical Database and Flowsheet Simulation. Outokumpu Research Oy Finland, 2006.
- [106] M.H. Uddin, L.T. Khajavi, The effect of sulfur in rotary kiln fuels on nickel laterite calcination, *Miner. Eng.* 157 (2020) 106563.
- [107] D.E. Newbury, N.W. Ritchie, Is scanning electron microscopy/energy dispersive X-ray spectrometry (SEM/EDS) quantitative?, *Scanning* 35 (2013) 141–168.
- [108] G.W.H. Höhne, W.F. Hemminger, H.-J. Flammersheim, *Differential scanning calorimetry*, Springer, 2003.
- [109] D. Walter, G. Buxbaum, W. Laqua, The mechanism of the thermal transformation from goethite to hematite, *J. Therm. Anal. Calorim.* 63 (2001) 733–748.
- [110] G. Li, T. Shi, M. Rao, T. Jiang, Y. Zhang, Beneficiation of nickeliferous laterite by reduction roasting in the presence of sodium sulfate, *Miner. Eng.* 32 (2012) 19–26.
- [111] M.E. Brown, D. Dollimore, A.K. Galwey, *Reactions in the solid state*, Elsevier, 1980.
- [112] A.W. Coats, J.P. Redfern, Kinetic parameters from thermogravimetric data, *Nature* 201 (1964) 68–69.
- [113] Ö. Çepelioğullar, H. Haykırı-Açma, S. Yaman, Kinetic modelling of RDF pyrolysis: Model-fitting and model-free approaches, *Waste Manag.* 48 (2016) 275–284.

- [114] T. Ozawa, A new method of analyzing thermogravimetric data, *Bull. Chem. Soc. Jpn.* 38 (1965) 1881–1886.
- [115] T. Akahira, T. Sunose, Method of determining activation deterioration constant of electrical insulating materials, *Res. Report Chiba Inst. Technol.* 16 (1971) 22–31.
- [116] S. Vyazovkin, C.A. Wight, Isothermal and nonisothermal reaction kinetics in solids: in search of ways toward consensus, *J. Phys. Chem. A.* 101 (1997) 8279–8284.
- [117] A.K. Galwey, M.E. Brown, *Thermal decomposition of ionic solids: chemical properties and reactivities of ionic crystalline phases*, Elsevier, 1999.
- [118] A.K. Burnham, R.K. Weese, B.L. Weeks, A distributed activation energy model of thermodynamically inhibited nucleation and growth reactions and its application to the β - δ phase transition of HMX, *J. Phys. Chem. B.* 108 (2004) 19432–19441.
- [119] J. Graetz, J.J. Reilly, Decomposition kinetics of the AlH_3 polymorphs, *J. Phys. Chem. B.* 109 (2005) 22181–22185.
- [120] A. Khawam, D.R. Flanagan, Complementary use of model-free and modelistic methods in the analysis of solid-state kinetics, *J. Phys. Chem. B.* 109 (2005) 10073–10080.
- [121] A. Khawam, D.R. Flanagan, Solid-state kinetic models: basics and mathematical fundamentals, *J. Phys. Chem. B.* 110 (2006) 17315–17328.
- [122] P.A. Candela, C.D. Crummett, D.J. Earnest, M.R. Frank, A.G. Wylie, Low-pressure decomposition of chrysotile as a function of time and temperature, *Am. Mineral.* 92 (2007) 1704–1713.
- [123] C.L. Chou, Sulfur in coals: A review of geochemistry and origins, *Int. J. Coal Geol.* 100 (2012) 1–13.
- [124] L.S. Tan, A.M. Shariff, K.K. Lau, M.A. Bustam, Factors affecting CO_2 absorption efficiency in packed column: A review, *J. Ind. Eng. Chem.* 18 (2012) 1874–1883.
- [125] K. Kamitsuji, T. Sato, H. Suzuki, C. Kaito, Direct observation of crystallization of amorphous Mg-bearing silicate grains into Mg (forsterite), *Astron. Astrophys.* 436 (2005) 165–169.

- [126] O. Levenspiel, *Chemical reaction engineering*, Wiley, 1999.
- [127] M. Ramezani, P. Tremain, K. Shah, E. Doroodchi, B. Moghtaderi, Kinetics and design parameter determination for a calciner reactor in unique conditions of a novel greenhouse calcium looping process, *Energy & Fuels* 32 (2018) 33–43.
- [128] J. Liu, D. Song, H. Guan, Isothermal kinetics approach to investigating the oxidation process of red phosphorus in air, *J. Therm. Anal. Calorim.* 128 (2017) 1801–1810.
- [129] D. Zhou, E.A. Schmitt, G.G.Z. Zhang, D. Law, C.A. Wight, S. Vyazovkin, D.J.W. Grant, Model-free treatment of the dehydration kinetics of nedocromil sodium trihydrate, *J. Pharm. Sci.* 92 (2003) 1367–1376.
- [130] B. Saha, A.K. Maiti, A.K. Ghoshal, Model-free method for isothermal and non-isothermal decomposition kinetics analysis of PET sample, *Thermochim. Acta* 444 (2006) 46–52.
- [131] L. Fedunik-Hofman, A. Bayon, S.W. Donne, Kinetics of solid-gas reactions and their application to carbonate looping systems, *Energies* 12 (2019) 2981.
- [132] M.H. Khedr, Isothermal reduction kinetics of Fe_2O_3 mixed with 1–10% Cr_2O_3 at 1173–1473 K, *ISIJ Int.* 40 (2000) 309–314.
- [133] M.H. Khedr, A.A. Farghali, A.A. Abdel-Khalek, Microstructure, kinetics and mechanisms of nano-crystalline CuFe_2O_4 reduction in flowing hydrogen at 300–600 °C for the production of metallic nano-wires, *J. Anal. Appl. Pyrolysis* 78 (2007) 1–6.
- [134] R.H. Condit, R.R. Hobbins, C.E. Birchenall, Self-diffusion of iron and sulfur in ferrous sulfide, *Oxid. Met.* 8 (1974) 409–455.
- [135] M. Danielewski, S. Mrowec, A. Stolosa, Sulfidation of iron at high temperatures and diffusion kinetics in ferrous sulfide, *Oxid. Met.* 17 (1982) 77–97.
- [136] P.K.Gbor, Behaviour of Co, Ni, Cu and Fe during aqueous SO_2 leaching of non-ferrous smelter slag, PhD Thesis, University of Toronto, 2003.
- [137] P.K. Gbor, C.Q. Jia, Critical evaluation of coupling particle size distribution with the shrinking core model, *Chemical Engineering Science* 59 (2004) 1979–87.

- [138] N. Mulchandani, V. Katiyar, Generalized kinetics for thermal degradation and melt rheology for poly (lactic acid)/poly (butylene succinate)/functionalized chitosan based reactive nanobiocomposite, *Int. J. Biol. Macromol.* 141 (2019) 831–842.
- [139] G.D. Mumbach, J.L.F. Alves, J.C.G. da Silva, M. Di Domenico, R.F. de Sena, C. Marangoni, R.A.F. Machado, A. Bolzan, Pyrolysis of cocoa shell and its bioenergy potential: evaluating the kinetic triplet, thermodynamic parameters, and evolved gas analysis using TGA-FTIR, *Biomass Convers. Biorefinery* (2020) 1–17.
- [140] W. Guo, H. Xiao, W. Guo, Modeling of TG curves of isothermal oxidation of graphite, *Mater. Sci. Eng. A* 474 (2008) 197–200.
- [141] A. Ortega, M. Macías, F. Gotor, Kinetics of the thermal decomposition of anhydrous cobalt nitrate by SCRT method, *J. Therm. Anal. Calorim.* 98 (2009) 441–448.
- [142] B. Janković, Isothermal reduction kinetics of nickel oxide using hydrogen: conventional and Weibull kinetic analysis, *J. Phys. Chem. Solids.* 68 (2007) 2233–2246.
- [143] F.J. Gotor, J.M. Criado, J. Malek, N. Koga, Kinetic analysis of solid-state reactions: the universality of master plots for analyzing isothermal and nonisothermal experiments, *J. Phys. Chem. A* 104 (2000) 10777–10782.
- [144] S. Singh, J.P. Chakraborty, M.K. Mondal, Intrinsic kinetics, thermodynamic parameters and reaction mechanism of non-isothermal degradation of torrefied *Acacia nilotica* using isoconversional methods, *Fuel* 259 (2020) 116263.
- [145] J. Cheng, J. Zhou, J. Liu, Z. Zhou, Z. Huang, X. Cao, X. Zhao, K. Cen, Sulfur removal at high temperature during coal combustion in furnaces: a review, *Prog. Energy Combust. Sci.* 29 (2003) 381–405.
- [146] M.R. Stouffer, H. Yoon, An investigation of CaO sulfation mechanisms in boiler sorbent injection, *AIChE J.* 35 (1989) 1253–1262.
- [147] P.W. Sage, N.W.J. Ford, Review of sorbent injection processes for low-cost sulphur dioxide control, *Proc. Inst. Mech. Eng. Part A Power Energy* 210 (1996) 183–190.

- [148] J. Adanez, V. Fierro, F. Garcia-Labiano, J. Palacios, Study of modified calcium hydroxides for enhancing SO₂ removal during sorbent injection in pulverized coal boilers, *Fuel* 76 (1997) 257–265.
- [149] C. Wang, X. Shen, Y. Xu, Investigation on sulfation of modified Ca-based sorbent, *Fuel Process. Technol.* 79 (2002) 121–133.
- [150] M. Rozpondek, M. Siudek, Pollution control technologies applied to coal-fired power plant operation, *Acta Montan. Slovaca.* 14 (2009) 156-160.
- [151] X. Ma, T. Kaneko, T. Tashimo, T. Yoshida, K. Kato, Use of limestone for SO₂ removal from flue gas in the semidry FGD process with a powder-particle spouted bed, *Chem. Eng. Sci.* 55 (2000) 4643–4652.
- [152] C.D. Bontzolis, M.K. Petraki, D.N. Spartinos, Experimental study and parametric analysis of SO₂ capture in limestone fixed bed reactor, *J. Chem. Technol. Biotechnol.* 94 (2019) 3227–3235.
- [153] T.D. Thiede, Analysis of limestone calcination and sulfation using transient gas analysis, PhD Thesis, Iowa State University, 1996.
- [154] J.H. Yang, S.M. Shih, P.H. Lin, Effect of carbon dioxide on the sulfation of high surface area CaCO₃ at high temperatures, *Ind. Eng. Chem. Res.* 51 (2012) 2553–2559.

Appendices

Appendix A List of the species used for thermodynamic analysis

The 137 species used for thermodynamic analysis by HSC Chemistry 5.11 are shown in Table A-1.

Table A-1 The list of 137 species used for thermodynamic analysis by HSC Chemistry 5.11.

CO(g)	Al ₂ O ₃	CaCO ₃	Fe ₂ MgO ₄	MgO	Na ₂ O	NiS ₂
CO ₂ (g)	Al ₂ S ₃	CaFe(SiO ₃) ₂	Fe ₂ MnO ₄	MgS	Na ₂ S	NiSi
COS(g)	Al ₂ SiO ₅	CaFe ₃ O ₅	Fe ₂ O ₃	MgSiO ₃	Na ₂ S ₂	NiSO ₄
CS(g)	Al ₄ C ₃	CaFe ₅ O ₇	Fe ₂ S ₃	MgSO ₃	Na ₂ S ₂ O ₃	S
CS ₂ (g)	Al ₄ CO ₄	CaFeSiO ₄	Fe ₃ C	MgSO ₄	Na ₂ S ₃	Si
N ₂ (g)	AlNi	CaMg ₂	Fe ₃ O ₄	MgTi ₂ O ₅	Na ₂ S ₄	SiO ₂
O ₂ (g)	AlTi	CaMgSiO ₄	FeCO ₃	MgTiO ₃	Na ₂ SiO ₃	SiS
S ₂ (g)	C	CaO	FeNaO ₂	Mn	Na ₂ SO ₃	SiS ₂
S ₃ (g)	Ca	CaO ₂	FeO	Mn ₂ O ₃	Na ₂ SO ₄	Ti
S ₄ (g)	Ca ₂ Al ₂ O ₅	CaS	FeS	Mn ₃ O ₄	NaFeO ₂	Ti ₂ S
S ₅ (g)	Ca ₂ Al ₂ SiO ₇	CaSi	FeS ₂	Mn ₃ Si	NaS	TiO ₂
S ₆ (g)	Ca ₃ Fe ₂ Si ₃ O ₁₂	CaSi ₂	Fe ₂ Si	MnCO ₃	NaS ₂	TiS
S ₇ (g)	Ca ₃ Si ₂ O ₇	CaSiO ₃	FeSiO ₃	MnO	Ni	TiS ₂
S ₈ (g)	Ca ₃ SiO ₅	CaSO ₃	FeSO ₄	MnS	Ni ₃ S ₂	TiS ₃
SO (g)	CaAl ₂	CaSO ₄	FeTi	MnS ₂	Ni ₃ S ₄	TiSi ₂
SO ₂ (g)	CaAl ₂ Si ₂ O ₈	Co	Mg	MnSi	NiAl	TiN ₃
SO ₃ (g)	CaAl ₂ SiO ₆	Cr ₂ O ₃	Mg ₂ Si	MnSO ₄	NiCO ₃	TiNi ₃
Al	CaAl ₂ O ₄	Fe	Mg ₂ SiO ₄	Na	NiFe ₂ O ₄	
Al ₂ (SO ₄) ₃	CaAl ₄	Fe _{0.87} S	Mg ₂ TiO ₄	Na ₂ C ₂ O ₄	NiO	
Al ₂ CO	CaC ₂ O ₄	Fe ₂ (SO ₄) ₃	MgAl ₂ O ₄	Na ₂ CO ₃	NiS	

Appendix B Gas flow rate calculation

The atmosphere resulted from coal combustion is simulated by purging SO₂, CO, CO₂, and N₂ gases to the tube furnace based on the molar ratio of the carbon in the coal to the sum of the iron and nickel oxides in the raw ore.

Initially, the number of moles for iron and nickels oxides are calculated based on the chemical composition of the ore (Table 4.2). Then, according to equation B1, the number of moles of carbon in burning coal is calculated based on the moles of iron and nickel oxides in the raw ore.

$$F = \frac{C}{(Fe_2O_3 + NiO)} \quad (B1)$$

Where F is directly correlated to the total gas flow rate. Considering the available plant data, the value of F in this study is selected between 0.5 to 4. Subsequently, based on the amount of carbon in burning coal (M_c in g) and the percentage of fixed carbon in the bituminous coal (60% fixed carbon as the average value for bituminous coal), the total mass of burning coal is obtained by equation B2.

$$M_{coal} = \frac{M_c}{0.6} \quad (B2)$$

Then, considering the sulfur content of the burning coal (%S), which is selected in the range of 0-15%, the amount of sulfur (M_s in g) in the coal is achieved by equation (B3).

$$M_s = M_c \times \%S \quad (B3)$$

The main reactions that occur during coal combustion are presented as equations B4-B6.





According to equation B4, sulfur oxidation results in SO₂ emission. Considering the sulfur content of the coal (M_s), the number of moles of SO₂ (n_{SO_2}) is calculated based on equation B4.

Carbon combustion leads to CO₂ and CO emission due to complete and incomplete combustions, respectively. Therefore, the carbon content of the coal corresponds to CO+CO₂.

The partial reduction in the industrial rotary kiln aims at reducing about 95% of hematite to wustite and 25% of nickel oxide to metallic nickel. Based on the thermodynamics of indirect reduction reactions of magnetite to wustite and nickel oxide to nickel at 900 °C, $P_{CO} > 0.4$ atm is required for completion of the reactions. Therefore, in this study $P_{CO}+P_{CO_2}$ in the input gas mixture is considered to be equal to 0.5 atm, while varying the individual pressures of CO and CO₂ to create various reducing atmospheres. It should be noted that CO₂ influences the reduction reactions by producing CO by Boudouard reaction. After finding the number of moles for SO₂, CO, and CO₂ gases, the number of moles for N₂, n_{N_2} , is calculated by equations B7 and B8 considering $P_{CO}+P_{CO_2} = 0.5$.

$$P_{N_2} = \frac{n_{N_2}}{n_{SO_2}+n_{CO_2}+n_{CO}+n_{N_2}} \quad (B7)$$

$$P_{SO_2} + P_{CO_2} + P_{CO} + P_{N_2} = 1 \quad (B8)$$

The last step is calculating the gas flow rates based on the number of moles of the gases. By assuming the ideal gas behavior at $P=1$ atm and $T=298$ K, the volume of each gas (V) is obtained by equation B9.

$$V = \frac{nRT}{P} \quad (\text{B9})$$

Where, n is the number of moles for a specific gas and R is the gas constant (0.0821 (lit.atm)/(mol.K)). The gas flow rate for the specific duration of the process (t) is obtained by dividing the gas volume by the purging duration.